Inaugural dissertation

for

obtaining the doctoral degree

of the

Combined Faculty of Mathematics, Engineering and Natural Sciences

of the

Ruprecht - Karls - University

Heidelberg

Presented by

Ivana Čavka

born in: Split, Croatia

Oral examination: 5.12.2023

Investigating the timing of crossover designation in *Caenorhabditis elegans* meiosis

Referees:

Prof. Dr. Jonas Ries

Prof. Dr. Sylvia Erhardt

Acknowledgements

The work presented in this thesis would not be possible without the advice, suggestions, kindness, patience, and support I have received from my supervisor, thesis advisory committee members, colleagues, collaborators, friends, and family. All of them have contributed to this work in different, invaluable ways, and I would like to start this thesis by thanking them for their contributions.

First and foremost, I would like to express my gratitude to Simone Köhler, under whose guidance all of the research presented here has been carried out. I thank her for the opportunity to work in her group and for the endless kindness and patience she has expressed over the last four and half years of us working together on this project. I have learned a lot by working with her, and I couldn't have asked for a better mentor at the beginning of my scientific career. Furthermore, I thank you, Simone, for your advice, help, and support while writing the thesis. Truly, thank you for everything!

Secondly, for the support, suggestions, and guidance of my scientific work during the last four and half years, I would like to thank my thesis advisory committee members, Jonas Ries, Sylvia Erhardt, and Sebastian Eustermann.

To all the current and past members of the Köhler lab: Cristina Piñeiro López, Ana Rita Rodrigues Neves, Ana Cobos Galvez, Oane Gros, Petra Bulankova, Sheba Cheeran, E. Berna Durmus, Lauren (Mickey) Sloat, Resul Gökberk Elgin, Jason Kong, and Sander Mallon. I thank them for creating a great work and scientific environment, as well as, for all our scientific and less scientific discussion. I especially thank the interns who have worked with me on the *in vivo* imaging of the germline: E. Berna Durmus, Lauren (Mickey) Sloat, and Jason Kong.

I thank all the present and past members of the Ries lab. Joining their weekly meetings allowed me to learn about super-resolution techniques. Their suggestions on the experimental procedures, data analysis, and interpretation of the results of my experiments were invaluable for obtaining the results of this study. For all the help they provided, the knowledge they shared, and their kindness, I would

especially like to thank Yu-Le Wu, Philipp Hoess, Takahiro Deguchi, Aline Tschanz, Ulf Matti, and Jonas Ries.

Likewise, I thank the microscopy specialists in EMBL's Advanced light microscopy facility and Imaging centre, Marko Lampe, Aliaksandr Halavatyi, Rory M. Power, and Dietrich Walsh.

Furthermore, I thank my collaborators Yumi Kim, Joshua Blundon, and Matthew E. Hurlock. I am thankful for the opportunity to work with them on localising the novel synaptonemal complex components presented in this and previous studies.

Lastly, to my friends and family. To my former roommate Esther, thank you for all the conversations and fun moments we have shared over the last few years. To my family, I thank them for their unconditional support and encouragement in everything I do.

Od sveg srca zahvaljujem svojoj majci Maši, teti Dragoj (Seji) i najvažnijoj trojci Anamariji, Marini i Augustinu. Hvala vam na svemu, vama posvećujem ovu disertaciju.

Thesis formatting

I used ES100 Latex template written by Sam Meijer as the basis of thesis formatting. I additionally adapted this template to form the final formatting following suggestions from https://www.overleaf.com/learn and my colleague, Ana Rita Rodrigues Neves' advice on table formatting and margin size.

Parts of this study have been published in:

1. Joshua Blundon, Brenda Cesar, Jung Woo Bae, Ivana Čavka, Jocelyn Haversat, Jonas Ries, Simone Köhler, Yumi Kim. (2023) Skp1 proteins are structural components of the synaptonemal complex in *C. elegans*. bioRxiv. may 2023; 2023.05.13.540652.

2. Ivana Čavka, Rory M. Power, Dietrich Walsh, Timo Zimmermann, Simone Köhler. (2022) Super-resolution microscopy of the synaptonemal complex within the *Caenorhabditis elegans* germline. Journal of Visualized Experiments. sep 2022; (187), e64363.

3. Matthew E. Hurlock, Ivana Čavka, Lisa E. Kursel, Jocelyn Haversat, Matthew Wooten, Zehra Nizami, Rashi Turniansky, Philipp Hoess, Jonas Ries, Joseph G. Gall, Ofer Rog, Simone Köhler, and Yumi Kim. (2020) Identification of novel synaptonemal complex components in *C. elegans*. Journal of Cell Biology, 219(5), may 2020. ISSN 15408140.

The research presented in this study was carried out under the supervision of Dr. Simone Köhler at the European Molecular Biology Laboratory in Heidelberg from April 2019 to September 2023.

Summary

Homologous recombination plays an important role in meiosis as it allows for the exchange of genetic information between homologous chromosomes that secures the diversity of the progeny. An excess of double-strand breaks is introduced and processed into recombination intermediates to achieve homologous recombination. However, only a limited subset of these recombination intermediates is designated to become crossovers. Any imbalance in the distribution of crossovers may lead to genomic instability and errors in chromosome segregation with devastating consequences on the health of the progeny. However, what is the main regulatory mechanism and when exactly crossovers are designated remain highly disputed questions. In this study, I harnessed recent advances in image analysis and 3D dual-colour single-molecule localisation microscopy (SMLM) to investigate the timing and mechanism of crossover designation in *Caenorhabditis elegans*.

This study combines *in vivo* confocal microscopy with a custom analysis pipeline for segmentation, foci detection, and tracking to identify the timing of crossover designation. Recombination intermediates are initially detected as dim, diffraction-limited foci of a pro-crossover factor, while designated crossovers at later stages are marked by bright foci. Interestingly, two populations of dim recombination intermediates that have differing association dynamics of the pro-crossover factors could be identified. Similarly, ultrastructures that are consistent with break repair intermediates that are destined to become crossovers were identified at earlier stages than previous data suggested. Together, these findings indicated that crossover designation happens earlier than previously thought.

To obtain these data, the experimental procedures had to be optimised and adapted. These optimisations now set a basis for future investigation of crossover regulation, quantitative analysis of time-lapse movies of the *C. elegans* germline, and the re-purposing of the SMLM data analysis tools for describing the 3D-SMLM localisations of the synaptonemal complex components and associated proteins.

Indeed, the optimised immunohistochemistry protocol compatible with 3D-SMLM imaging was invalu-

able in investigating the organisation and function of novel synaptonemal complex components. 3D-SMLM imaging showed that SYP-5/6 proteins are transversal filaments that span the width of the synaptonemal complex. Furthermore, 3D-SMLM imaging proved that Skp1-related proteins (SKR-1/2 in *C.elegans*) localise to the central region of the synaptonemal complex. This result was contrary to the chromosome axis localisation observed in mice and provided further insight into the possible roles of these proteins within the synaptonemal complex in *C. elegans*. 3D-SMLM imaging combined with the appropriate sample preparation broadened the understanding of the structure of the synaptonemal complex in *C. elegans*.

Zusammenfassung

Die homologe Rekombination spielt in der Meiose eine wichtige Rolle, da sie den Austausch genetischer Informationen zwischen homologen Chromosomen ermöglicht und so die Vielfalt der Nachkommenschaft sichert. Damit homologe Rekombination stattfinden kann, muss ein Überschuss an Doppelstrangbrüchen in das Genom eingeführt und zu Rekombinationsintermediaten verarbeitet werden. Allerdings ist nur eine begrenzte Anzahl dieser Rekombinationsintermediate dazu bestimmt, zu Crossovern zu werden. Eine unausgewogene Verteilung der Crossover im Genom kann zu genomischer Instabilität und Fehlern bei der Chromosomensegregation führen mit verheerende Folgen für die Gesundheit der Nachkommenschaft. Wie dieser Prozess reguliert wird, und wann genau die Entscheidung getroffen wird, welche Rekombinationsintermediate zu Crossovern werden, ist jedoch nach wie vor höchst umstritten. In dieser Studie habe ich jüngste Fortschritte in der Bildanalyse und der 3D-Zweifarben-Einzelmolekül-Lokalisationsmikroskopie (SMLM) genutzt, um den Zeitpunkt und den Mechanismus der Festsetzung von Crossovern in *Caenorhabditis elegans* zu untersuchen.

In dieser Studie habe ich konfokale Mikroskopie am lebenden Organismus mit einer maßgeschneiderten Analysepipeline für Segmentierung, Punkt-Erkennung und Tracking kombiniert, um zu ermitteln wann Rekombinationsintermediate zu Crossovern bestimmt werden. Rekombinationsintermediate werden zunächst als schwach leuchtende, beugungsbegrenzte Punkte eines Pro-Crossover-Faktors abgebildet, während designierte Crossover in späteren Stadien durch helle Foci markiert werden. Interessanterweise konnten zwei Populationen von schwach leuchtenden Rekombinationsintermediaten identifiziert werden, die eine unterschiedliche Assoziationsdynamik der Pro-Crossover-Faktoren aufweisen. Des Weiteren wurden mittels Einzelmolekül-Lokalisationsmikroskopie Ultrastrukturen identifiziert, die einzelnen Zwischenstufen der Bruchreparatur ähneln, die dazu bestimmt sind, zu Crossovern zu werden. Diese Ereignesse konnte ich nun in früheren Stadien nachweisen als frühere Daten vermuten ließen. Zusammengenommen deuten diese Ergebnisse darauf hin, dass die Bestimmung von

Crossovern früher erfolgt als bisher angenommen.

Um diese Daten zu erhalten, musste ich die experimentellen Verfahren anpassen und optimieren. Diese Optimierungen bilden nun die Grundlage für künftige Untersuchungen der Crossover-Regulation mittels quantitativer Analyse von Zeitrafferfilmen der Keimbahn von *C. elegans* oder zur Beschreibung von 3D-SMLM-Lokalisationen der Komponenten des synaptonemalen Komplexes und der damit verbundenen Proteine.

Das optimierte immunhistochemische Protokoll, das mit der 3D-SMLM-Bildgebung kompatibel ist, war von unschätzbarem Wert für die Untersuchung der Organisation und Funktion neuartiger Komponenten des synaptonemalen Komplexes. Die 3D-SMLM-Bildgebung zeigte, dass SYP-5/6-Proteine transversale Filamente sind, die die Breite des synaptonemalen Komplexes überspannen. Darüber hinaus zeigte die 3D-SMLM-Bildgebung, dass Skp1-verwandte Proteine (SKR-1/2 in C.elegans) in der zentralen Region des synaptonemalen Komplexes lokalisiert sind. Dieses Ergebnis stand im Gegensatz zu Erkenntnissen bei Mäusen, in denen Skp1-verwandte Proteine in der Chromosomenachse zu finden sind, und lieferte damit weitere Erkenntnisse über die mögliche Rolle dieser Proteine innerhalb des synaptonemalen Komplexes in *C. elegans*. Die 3D-SMLM-Bildgebung in Verbindung mit einer geeigneten Probenvorbereitung hat das Verständnis der Struktur des synaptonemalen Komplexes in *C. elegans* erweitert.

Contents

List of Figures v

List of Tables vii

1 Introduction 1

1.1 Basics of meiosis . . . 1

1.2 Meiotic prophase I in *Caenorhabditis elegans* . . . 2

1.3 Organization of the synaptonemal complex . . . 3

1.4 Regulation of crossover number and distribution . . . 5

1.4.1 Crossover interference models . . . 7

1.4.2 Crossover regulation in *Caenorhabditis elegans* . . . 9

1.4.3 Synaptonemal complex and crossover regulation . . . 10

1.5 Fluorescence microscopy . . . 11

1.5.1 Confocal microscopy . . . 11

1.5.2 Super-resolution microscopy techniques . . . 11

1.6 Single-molecule localisation microscopy . . . 12

2 Aims 15

3 Materials and methods 19

3.1 *Caenorhabditis elegans* maintenance . . . 19

3.2 CRISPR/Cas9-mediated genome editing . . . 19

3.3 Brood counts . . . 20

3.4 Cytology . . . 21

3.4.1 Poly-L-lysine coated coverslips . . . 21

3.4.2 Conjugation of F(ab')$_2$ fragments with organic fluorophores 21
3.4.3 Feeding worms with HaloTag ligands conjugated with fluorescent organic dyes 22
3.4.4 Immunohistochemistry of *Caenorhabditis elegans* germline tissue 22
3.4.5 Confocal imaging of fixed germline tissue 25
3.4.6 Stimulated emission depletion microscopy 26
3.4.7 Single-molecule localisation microscopy (SMLM) 27
3.5 *In vivo* imaging of crossover designation in *C. elegans* 29
3.5.1 Sample preparation 29
3.5.2 Confocal imaging 30
3.6 Aligning the line profiles of regions of interest in STED images 31
3.7 Data analysis for the 3D-single molecule localisation microscopy data 31
3.7.1 Mapping positions and orientation of SYP-5/6 proteins by 3D single-molecule localisation microscopy 31
3.7.2 Localisation of SKR-1/2 within the substructure of the synaptonemal complex 32
3.7.3 Straightening of SMLM localisations along an annotated polyline 32
3.7.4 Describing the shape of a continuous stretch of the synaptonemal complex in SMLM images 39
3.7.5 Describing the super-resolved organization of the MSH-5::V5 at recombination intermediates 41
3.7.6 Describing the super-resolved organization of HTP-3::HA at recombination sites 43
3.8 Data analysis for the *in vivo* imaging of *C. elegans* germline 43
3.8.1 Quantification of the number of COSA-1 foci within individual meiotic nuclei 43
3.8.2 Determining the position of meiotic nuclei within the germline 45
3.8.3 Mean intensity and number of HaloTag::COSA-1 foci per nucleus 46
3.8.4 Quantifying the distribution of HaloTag::COSA-1 foci along individual chromosome 46

3.8.5 Additional image processing 49

4 Super-resolution microscopy of the synaptonemal complex in *C. elegans* germline 51

4.1 Optimising the sample preparation for super-resolution microscopy of the synaptonemal complex 52

4.2 SYP-5/6 transverse the width of the synaptonemal complex 55

4.3 SKR-1 and SKR-2 localise within the central region of the synaptonemal complex . . 56

4.4 Discussion 63

5 Timing of crossover designation in *Caenorhabditis elegans* meiosis 67

5.1 Image analysis pipeline faithfully captures the number and intensity distribution of COSA-1 protein along the germline 68

5.2 Optimised immobilization protocol allows for long-term imaging of the meiosis . . . 70

5.3 *In vivo* imaging of *C. elegans* germlines discovers intricate dynamics of HaloTag::COSA-1 foci 72

5.4 Blinking foci have lower intensity compared to persistent foci 79

5.5 Super-resolution imaging identifies the variety of MutSγ complex organization at recombination sites 82

5.6 Chromosome axes distortions in proximity of crossover precursors 89

5.7 Discussion 93

5.8 Outlook 98

Concluding remarks 101

Bibliography 103

Appendices 123

Appendix A *Caenorhabditis elegans* strains used in this study 123

Appendix B Specifics of CRISPR/Cas9-mediated genome editing 125

Appendix C Brood counts for the *Caenorhabditis elegans* strains generated in this study 131

Appendix D Reagents used in cytological methods 133

Appendix E Single molecule localisation microscopes used in this study 137

Appendix F Supplementary information for section 4.2 139

Appendix G Supplemental information for chapter 5 141

List of publications 147

List of Figures

1.1 Comparison of mitotic and meiotic cell divisions 1

1.2 Meiotic prophase I in *Caenorhabditis elegans* 3

1.3 Organization of the synaptonemal complex 5

1.4 Meiotic double-strand break repair 6

1.5 Models of crossover interference 8

3.1 Mounting of *C. elegans* dissected tissue for super-resolution microscopy 25

3.2 Workflow to straighten SMLM localisations along an annotated polyline 33

3.3 Describing the shape of chromosome axes in single-molecule localisation microscopy images 38

3.4 Association of HaloTag::COSA-1 foci to individual synaptonemal complexes 47

3.5 Describing the dynamics of HaloTag::COSA-1 foci along traced synaptonemal complexes 49

4.1 Dependence of the Fourier ring correlation resolution of single-molecule localisation microscopy images on the distance of the imaged *z*-plane from the plane of the coverslip 54

4.2 Single-molecule localisation microscopy of HTP-3 and the C-termini of the SYP-5 . . 58

4.3 Fluorescence Lifetime Imaging enhanced Tau-Stimulated emission depletion (TauSTED) microscopy resolves two localisation bands for both, HTP-3 and the C-terminus of SYP -5 59

4.4 Aligned stretches of the synaptonemal complex in late pachytene 60

4.5 SKR-1 protein localises to the central region of the synaptonemal complex 61

4.6 SKR-2 protein localises to the central region of the synaptonemal complex 62

4.7 Localisation of the SYP-5/6 and SKR-1/2 proteins within the synaptonemal complex of *Caenorhabditis elegans* 65

5.1 Distribution of HaloTag::COSA-1 foci along the *Caenorhabditis elegans* germline . . 69

5.2 Progression of meiosis is confirmed by the presence of chromosome movement and nuclear rotation 71

5.3 Photobleaching assessment 72

5.4 HaloTag::COSA-1 foci intensity at different timing during pachytene 73

5.5 Nuclei whose synaptonemal complexes have been manually traced 74

5.6 Comparison of the spotMAX results and the sharpened image of HaloTag::COSA-1 fluorescent signal 76

5.7 The last HaloTag::COSA-1 focus to remain attached to the individual synaptonemal complexes is, at the same time, the most persistent focus 80

5.8 The relationship between HaloTag::COSA-1 focus intensity and persistence 81

5.9 Ultrastructure of MSH-5::V5 foci resolved by single-molecule resolution microscopy . 83

5.10 MutSγ complex distribution at recombination intermediates 88

5.11 Chromosome axis rearrangements at crossover precursor sites 90

5.12 Characterising the organization of the synaptonemal complex in proximity to putative designated crossover sites 92

5.13 Model for the association of MutSγ complex at recombination intermediates 98

F.1 Examples of individual stretches taken from SMLM images for mapping position and orientation of SYP-5/6 proteins . . . 139
G.1 Supplemental information for Figure 5.1A . . . 141
G.2 Characterisation of synaptonemal complex tracing . . . 142
G.3 HaloTag::COSA-1 foci counts for each traced synaptonemal complex . . . 143
G.4 Supplemental information for Figure 5.6 . . . 144
G.5 Supplemental information for Figure 5.12 . . . 145

List of Tables

3.1 spotMAX parameters used to detect individual HaloTag::COSA-1 foci . . . 45
3.2 Typical TrackMate parameters used to track meiotic nuclei during timelapse movies of *Caenorhabditis elegans* germline . . . 45

A.1 *Caenorhabditis elegans* strains used in the study . . . 123

B.1 Alleles generated for this study by CRISPR/Cas9-mediated genome editing . . . 125
B.2 Repair templates for CRISPR/Cas9-mediated genome editing . . . 126
B.3 Sequences of CRISPR-RNA (crRNA), genotyping information, and sequencing primers for each CRISPR/Cas9-mediated genome editing . . . 128

C.1 Brood counts for the *Caenorhabditis elegans* strains generated in this study . . . 131

D.1 Reagents used for flourescent staining in the cytological experiments . . . 133
D.2 Specifics of the cytological experiments . . . 135

E.1 Single molecule localisation microscopes used in this study . . . 137

F.1 Number and total length of the stretches that were analyzed to map the orientation of SYP-5 and SYP-6 139

F.2 Distribution parameters of the HA::SYP-5/6 and SYP-5/6::HA localisations 140

G.1 Total length of super-resolved synaptonemal complex stretches analysed in chapter 5 145

G.2 Total number of super-resolved MSH-5::V5 foci analysed in chapter 5 145

List of Abbreviations

Btn	Biotin
CGC	Caenorhabditis Genetics Center
CRISPR	Clustered regularly interspaced short palindromic repeats
crRNA	CRISPR-RNA
DNA	Deoxyribonucleic acid
dsDNA	Double-stranded DNA
ECDF	Empirical cumulative distribution function
FLIM	Fluorescence lifetime imaging
HA	Hemagglutinin
HWHM	Half width at half maximum
mod	Remainder of a division operator (modulo)
PBS	Phosphate-buffered saline
PBST	Phosphate-buffered saline with 0.1% Tween® 20
PBST*	Phosphate-buffered saline with 0.2% Tween® 20
PCA	Principal component analysis
PCR	Polymerase chain reaction
PSF	Point spread function
RNA	Ribonucleic acid
SIM	Structured illumination microscopy
SMLM	Single-molecule localisation microscopy
STED	Stimulated emission depletion

1. Introduction

1.1. Basics of meiosis

During meiosis, two consecutive chromosome segregation events, termed meiosis I and II, proceed after a single round of DNA replication, reducing the number of chromosomes by half to produce up to four gametes. The original chromosome number is restored upon fertilization.

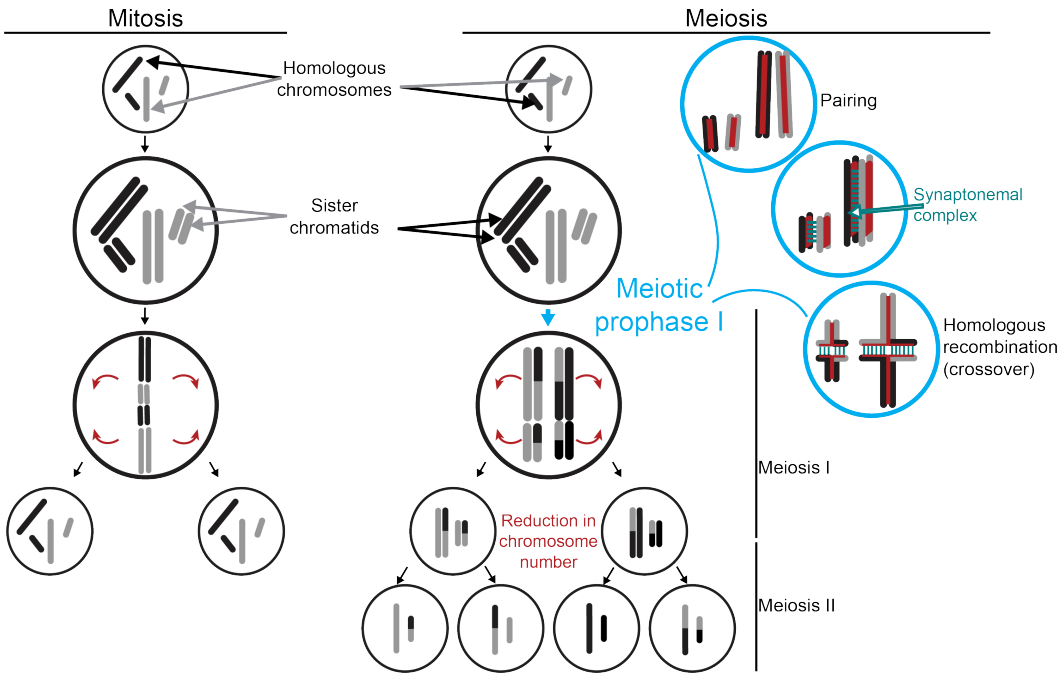


Figure 1.1. Comparison of mitotic and meiotic cell divisions
Illustration of a selected subset of mitotic and meiotic events that highlight differences in the two types of cell division. Additionally, three hallmarks of meiotic prophase I, including pairing (and alignment), synapsis, and the exchange of the genetic information between homologous chromosomes (crossover formation), are highlighted in cyan.

Generally speaking, the two homologous chromosomes are segregated in the first meiotic division (meiosis I), which is unlike the segregation of sister chromatids during the mitosis or the second meiotic

division, meiosis II (**Figure 1.1**) (Zickler and Kleckner, 1999).

To segregate the two homologous chromosomes in meiosis I, they must be aligned in the metaphase I plane. To this end, the two homologous chromosomes must recognise each other during prophase I. The assembly of the synaptonemal complex between them further corroborates the initial pairing interactions. Additionally, the two chromosomes are linked together through homologous recombination that results in the exchange of genetic information between paternal and maternal chromosomes (crossover - **Figure 1.1**). Once the synaptonemal complex disassembles in late prophase I, the crossover site provides a physical connection between the two homologous chromosomes until their segregation. Such a connection can be cytologically detected and has been termed a chiasmata (Hunter, 2015).

1.2. Meiotic prophase I in *Caenorhabditis elegans*

Prophase I is a fascinating process divided into five stages: leptotene, zygotene, pachytene, diplotene, and diakinesis. As meiotic nuclei progress through prophase I, they physically move within the gonad of the nematode *Caenorhabditis elegans*. For this reason, the *C. elegans* germline offers a temporal resolution of all prophase I events (Lui and Colaiácovo, 2013; Hillers et al., 2017).

Leptotene and zygotene stages cannot easily be distinguished within the germline tissue cytologically. Therefore, meiotic nuclei undergoing these two stages are typically grouped within a region of the germline termed the transition zone (**Figure 1.2**). Nuclei within the transition zone are characterised by a crescent shape of the fluorescently labelled chromatin. This shape results from pairing homologous chromosomes (Lui and Colaiácovo, 2013). Additionally, double-strand breaks are introduced across the genome by the specialised topoisomerase-related protein SPO-11 starting from transition zone (Dernburg et al., 1998; Hicks et al., 2022). The end of the zygotene stage and the transition zone is defined by the complete assembly of the synaptonemal complex between the two homologous chromosomes (**Figure 1.2**).

Through the next phase, pachytene, crossovers form and mature. The crossovers result from the repair of double-strand breaks by homologous recombination. In *C. elegans*, each genome receives

approximately 30-50 double-strand breaks (Woglar and Villeneuve, 2018; Almanzar et al., 2021; Rosu et al., 2011; Colaiácovo et al., 2003) but only six of these breaks, one per pair of homologous chromosomes, yield a crossover, i.e. the exchange of the genetic information between parental and maternal homologous chromosomes. The crossover sites in *C. elegans* can be cytologically detected as bright foci of COSA-1 protein in late pachytene (Yokoo et al., 2012).

During diplotene and diakinesis, chromosomes desynapse (the synaptonemal complex partially disassembles) and further compact (Zickler and Kleckner, 1999).

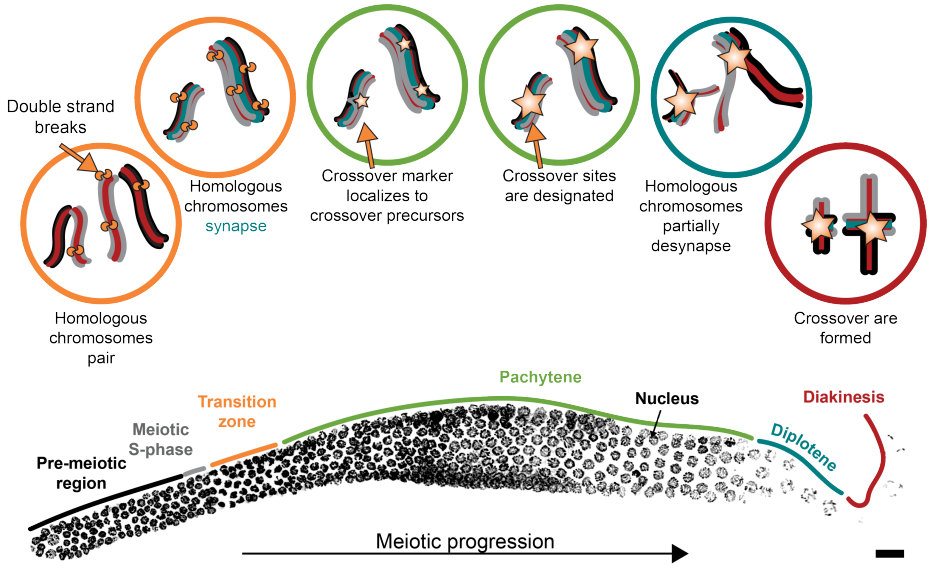


Figure 1.2. Meiotic prophase I in *Caenorhabditis elegans*
Bottom: Maximum intensity projection image of a DAPI stained germline of a *C. elegans* hermaphrodite. The direction in which individual meiotic nuclei move through the tissue as they progress through the stages of meiotic prophase I is indicated below the image (scale bar: 10 µm). Top: Illustration of the events during each prophase I stage. The outline's colour in the cartoon associates the displayed event to the prophase I stage in which it occurs. Additionally, the section of the gonad that contains nuclei in individual stages is marked by lines of the same colour. For simplicity, only two out of six pairs of homologous chromosomes are drawn in the graphics.

1.3. Organization of the synaptonemal complex

The general structure of the synaptonemal complex is evolutionary conserved even though there is little sequence homology between its protein components (**Figure 1.3**, Fraune et al. 2012; Kursel et al. 2021; Hemmer and Blumenstiel 2016). In electron micrographs, the synaptonemal complex appears

as a tripartite ladder-like structure that is composed of two lateral elements or axes and a central region (Colaiácovo, 2006). An electron-dense central element along the midline of the central region (**Figure 1.3**) can be observed as well (Carpenter, 1975).

Proteins of the central region contain coiled-coiled domains, which is an evolutionary conserved feature (Fraune et al., 2012; Kursel et al., 2021), while the axes are built from meiosis-specific cohesin complexes and other meiosis-specific proteins (Ur and Corbett, 2021). In *C. elegans*, the chromsome axes are composed by three different cohesin complexes as well as meiosis-specific HORMA domain proteins (HTP-1/2, HTP-3, HIM-3; Zetka et al., 1999; Martinez-Perez and Villeneuve, 2005; Couteau and Zetka, 2005; Goodyer et al., 2008; Severson et al., 2009). The central region consists of at least 6 coiled-coil proteins, SYP-1-6 (Colaiácovo et al., 2003; MacQueen et al., 2002; Smolikov et al., 2007, 2009; Hurlock et al., 2020; Zhang et al., 2020), and the Skp-1 related proteins SKR-1 and SKR-2 (Blundon et al., 2023). The proteins SYP-1 and SYP-5/6 are the transverse filaments of the synaptonemal complex. The term transverse filament reflects their role in spanning the width of the central region in a head-to-head manner connecting the two chromosome axes (**Figure 1.3**, Schild-Prüfert et al. 2011; Hurlock et al. 2020). The assembly of the central region in *C. elegans* requires the presence of all central region proteins, with the exception of SYP-5 or SYP-6 and SKR-1 or SKR-2, which are two pairs of paralogs that are partially redundant (Hurlock et al., 2020; Zhang et al., 2020; Blundon et al., 2023).

The organization of the chromosome axis and central region of the synaptonemal complex in *C. elegans* has been studied previously by electron microscopy (Schild-Prüfert et al., 2011), by single-molecule localization (SMLM) microscopy Köhler et al. (2017, 2020), and by structured illumination microscopy (Woglar et al., 2020). These studies elucidated the organization of the synaptonemal complex in *C. elegans*.

Additionally, it has been reported that the synaptonemal complex is a dynamic structure which undergoes a change in its dynamics from a more dynamic state in early pachytene to a more rigid state in late pachytene (Pattabiraman et al., 2017; Rog et al., 2017; Nadarajan et al., 2017). Interestingly, the change in the dynamic state of the synaptonemal complex coincides with crossover designation.

Furthermore, growing evidence points to an active role of the synaptonemal complex components in crossover regulation that limits the number and distribution of crossover events (Hayashi et al., 2010; Libuda et al., 2013; Wang et al., 2015; Pattabiraman et al., 2017; Woglar and Villeneuve, 2018; Morgan et al., 2021; Zhang et al., 2021).

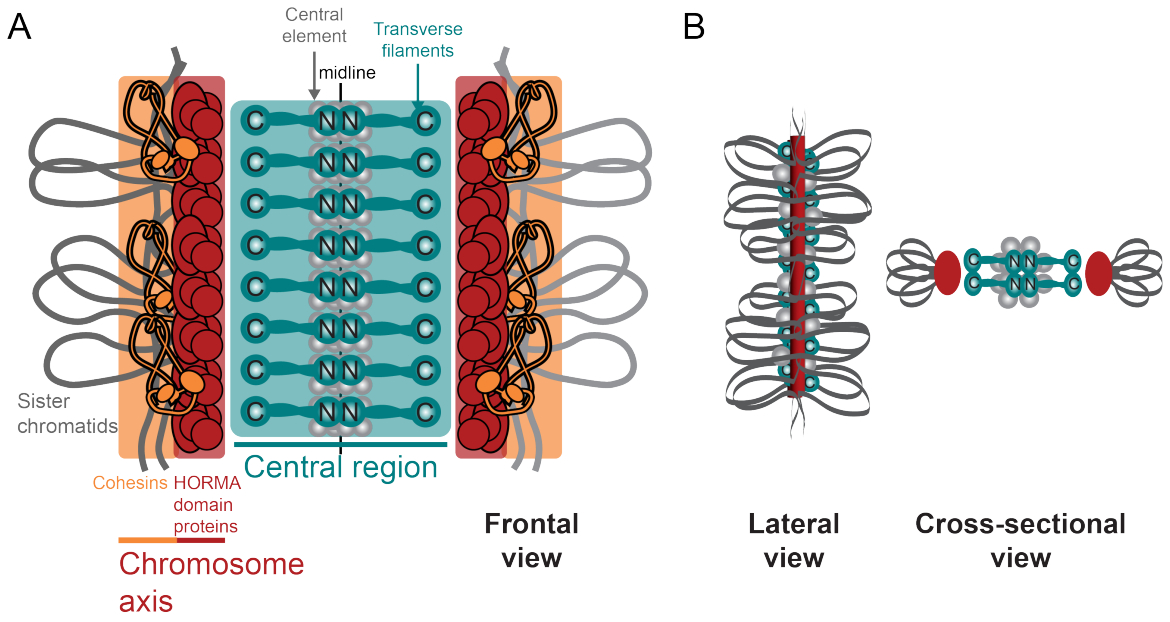


Figure 1.3. Organization of the synaptonemal complex
(A) Illustration of the evolutionary conserved organisation of the synaptonemal complex. The two chromosome axes assemble between sister chromatids of each homologous chromosome pair. The synaptonemal complex central region bridges the axes. The chromosome axes consist of HORMA domain proteins and meiosis-specific cohesin complexes in *C. elegans*. Within the central region, the transverse filaments span the width of the synaptonemal complex and are oriented in a head-to-head orientation, with their N-termini located at the midline, and their C-termini placed close to the chromosome axes. Additional central elements stabilize the synaptonemal complex. A frontal view is shown in A, and **(B)** shows the corresponding lateral and cross-sectional views.

1.4. Regulation of crossover number and distribution

To form crossovers, double-strand breaks must be repaired by using a homologous chromosome as a repair template (**Figure 1.4**). Crossovers not only increase the genetic variation among the progeny but are also important for proper segregation of homologous chromosomes (Pazhayam et al., 2021).

The ends are resected after the introduction of double-strand breaks by topoisomerase-like protein

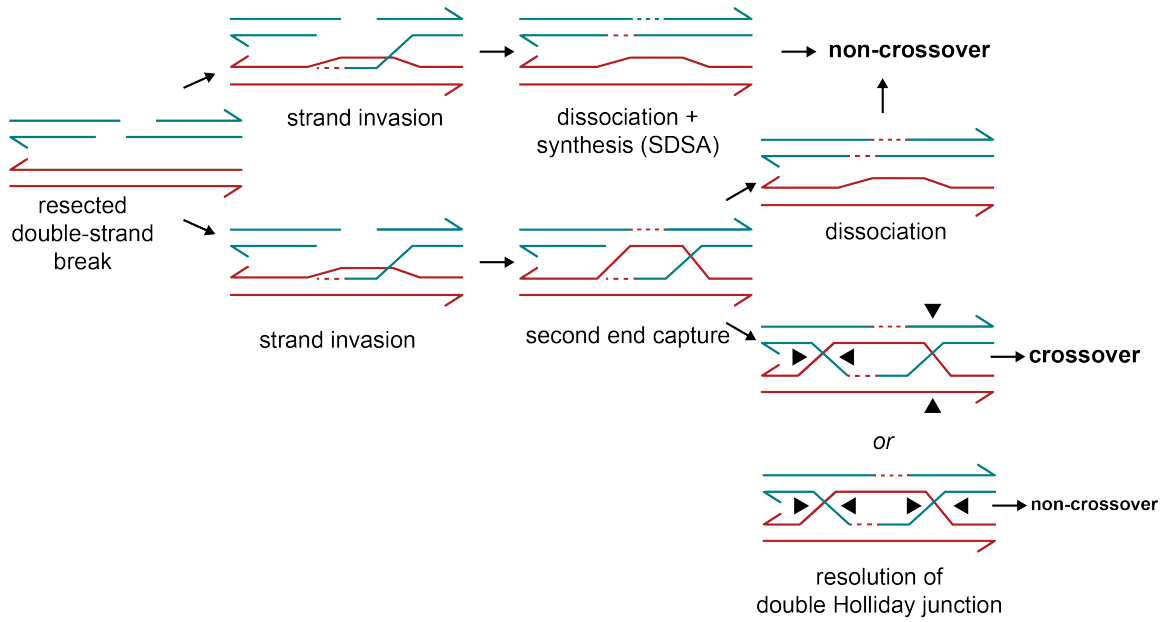


Figure 1.4. Meiotic double-strand break repair

Schematic overview of homologous recombination intermediates and crossover formation. Only dsDNA for one sister chromatid is shown for each pair of homologs (cyan and red lines). The illustration is adapted from Pazhayam et al. 2021 with several modifications, including the addition of the steps predicted by the original double-strand break repair (Szostak et al., 1983). I am not the author of the original graphic.

(SPO-11). Subsequently, meiotic-specific recombinases coat the single strand ends and lead the strand invasion (**Figure 1.4**) into the homologous template, forming the D-loop. Stabilising the D-loop by extending the invading strain or association with stabilising proteins leads to the formation of the single end invasion events (Hunter, 2015). This is followed by the second end capture, where the other strand (non-invading) of the broken DNA is annealed to the displaced strand of the template (**Figure 1.4**). Further processing involving the synthesis, ligation, and possibly branch migration results in the formation of the double Holliday junction (Ahuja et al., 2021). Only a small subset of double-strand breaks will result in a crossover, and the majority will be repaired into the non-crossovers (Hunter, 2015). Furthermore, it is currently thought that only a small subset will result in the formation of the double Holiday junction and that the majority of non-crossover results from earlier dissociation and subsequent synthesis-dependant strand annealing (SDSA, Allers and Lichten 2001).

Initially, it was proposed that all double-strand breaks are processed into double Holliday junctions. Subsequently, a small subset of these double Holliday junctions would then be resolved into crossover

events while the majority would give rise to non-crossovers by differential resolution of the junction (**Figure 1.4**, arrowheads) (Szostak et al., 1983). In this model, the distinction of the crossover and non-crossover events happens at the very last step of the repair by differential cleavage of the double Holliday junction (**Figure 1.4**). However, subsequent studies of recombination intermediates have revealed that the distinction between crossover and non-crossover events happens early in the process. A new model was proposed (Allers and Lichten, 2001) where all double Holliday junctions produce crossovers, while most (or all) non-crossovers are the result of the dissociation of the invading strand and synthesis dependant strand annealing (**Figure 1.4**).

Studies in yeast showed that the formation of the first detectable crossover-specific intermediate (single-end intermediate, Hunter and Kleckner 2001) coincides with the formation of synapsis.

The formation of crossovers during meiosis is regulated on two main levels: First, it has to be assured that each homolog pair has at least one crossover, which provides a physical link between the homologs; Second, it has been observed that crossover events are non-randomly distributed along the length of a chromosome pair, and they are less likely to appear near each other. This phenomenon has been termed crossover interference (Sturtevant, 1913; Zickler and Kleckner, 1999). Crossovers that are sensitive to crossover interference are known as type I crossovers. In many organisms, additional, non-interfering crossovers may occur (type II). Additionally, crossovers are also suppressed in certain regions of the genome, such as around centromeres. Centromeric suppression was, e.g. observed in humans, fruit-fly, budding, and fission yeast (Pazhayam et al., 2021). However, the mechanism of how crossover formation is regulated remains unknown. These crossover regulation processes are extremely robust in *C. elegans* wild-type animals where each pair of homologs receives exactly one crossover. Therefore, crossover assurance and interference are complete (Lui and Colaiácovo, 2013) making *C. elegans* an ideal model organism to study these processes.

1.4.1. Crossover interference models

Over the years, the crossover interference phenomenon has been described by several models: the polymerization model, the compartmentalised signal model, the spatial cluster model, the beam-film

model, or the coarsening model (Pazhayam et al., 2021; Girard et al., 2023). The latter two models, the beam-film model and the coarsening model are the most commonly used models in the field.

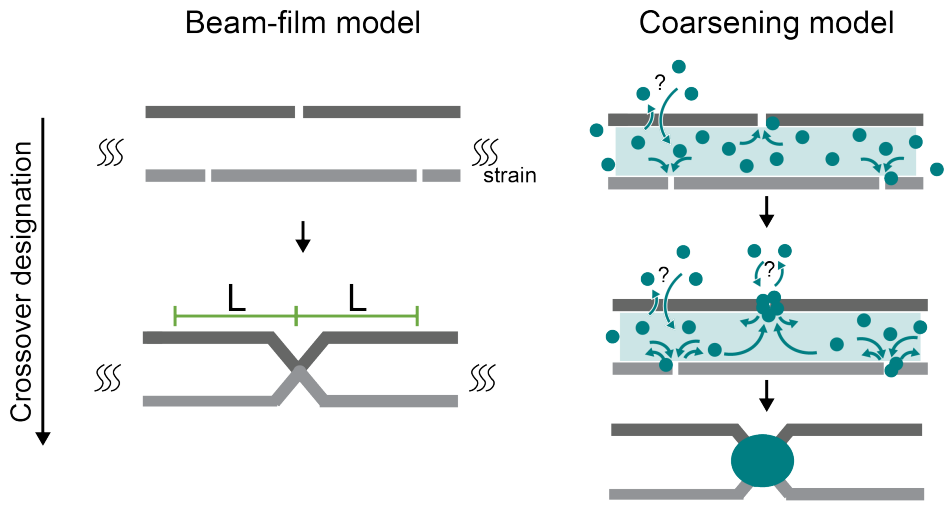


Figure 1.5. Models of crossover interference

The cartoons illustrate the two main proposed models of crossover interference: the beam film model (Kleckner et al., 2004; Zhang et al., 2014) and the coarsening model (Morgan et al., 2021).

The beam-film model is a mechanistic model based on the notion that the designation of a crossover leads to the spread of an outward signal that prevents other crossovers in the proximity (Kleckner et al., 2004). The model proposes that meiotic chromosomes behave as elastic beams covered by a thin, brittle film that contains flaws (double-strand breaks). These flaws can crack once mechanical stress is introduced by a strain on the beam (Pazhayam et al., 2021). The formation of a crack (crossover) on the film leads to local relaxation of the stress and prevents the occurrence of another crack nearby (**Figure 1.5**). The distance between cracks or crossovers, therefore, depends on the mechanical properties of the system and the introduced strain. The beam-film model has been used to model crossover distributions in various organisms (Zhang et al., 2014). Furthermore, it has been proposed that the mechanical stress accumulation and propagation of the mechanical stress happens via the interaction of DNA and proteins at the chromosome axis (Girard et al., 2023).

More recently, a new model of crossover interference has been proposed based on cytological evidence from *Arabidopsis thaliana* (Morgan et al., 2021) and *C. elegans* (Zhang et al., 2018, 2021). This

model suggests that crossovers are designated by the accumulation of the pro-crossover factors at the subset of the recombination intermediates while the factors are depleted from neighbouring sites along the chromosome (Girard et al., 2023). The model was termed the coarsening model, reflecting the coarsening dynamics of the pro-crossover factors.

In this model, the synaptonemal complex is proposed as a medium through which coarsening proteins (HEI10 in *A. thaliana*, and ZHP-3 in *C. elegans*) diffuse between recombination intermediates (**Figure 1.5**). The retention of the coarsening factor at the recombination intermediates leads to the formation of differently-sized foci. Through a coarsening process, larger foci accumulate more material, and they grow at the expense of smaller foci, resulting in the designation of larger foci into crossovers (Morgan et al., 2021).

Since all synaptonemal complexes within the nucleus initially load a certain amount of coarsening proteins and diffusion is assumed to mainly occur within the synaptonemal complex (less between the synaptonemal complex and the nucleoplasm), the model proposes that crossover assurance and interference can be explained by a same regulatory mechanism (Morgan et al., 2021; Zhang et al., 2021).

1.4.2. Crossover regulation in Caenorhabditis elegans

In *C. elegans*, crossover interference is established on a distance longer than the chromosomes themselves, which is why only one type I crossover can be observed on each pair of homologous chromosomes. These crossover sites are characterised by the accumulation of pro-crossover factors such as COSA-1, MSH-5, and ZHP-1/2/3/4 (Yokoo et al., 2012; Zhang et al., 2018; Jantsch et al., 2004; Woglar and Villeneuve, 2018; Bhalla et al., 2008; Nguyen et al., 2018).

COSA-1 is the most commonly used cytological crossover marker. During mid-pachytene, putative recombination intermediates (**Figure 1.2**) can be identified as a 'dim' foci of COSA-1 protein, while in late pachytene, COSA-1 protein accumulates to six designated crossover sites that are markedly brighter than mid-pachytene foci (Woglar and Villeneuve, 2018). However, the exact point when crossover designation occurs remains unknown since it cannot be distinguished whether the accumulation of

COSA-1 is a designation-determining factor or a consequence of the same.

More recently, the coarsening behaviour of the ZHP-3 protein has been proposed as the driving factor of crossover designation in *C. elegans* (Zhang et al., 2021). This model implies that crossover designation occurs late an concomitant with the first observation of bright COSA-1 foci in *C. elegans*. This proposition is in contrast to what has been proposed for budding yeast and mice based on the biochemical studies of recombination intermediates. For these model organisms and *Sordaria macrospora*, crossover designation may occur early during meiotic prophase and presumably before the completion of synapsis (Fung et al., 2004; de Boer et al., 2006; Zickler et al., 1992). Importantly, these organisms differ in the dependence of synapsis on recombination. Specifically, recombination is required for synapsis in budding yeast and mice, while recombination is dispensable for synapsis in *C. elegans*. Therefore, the questions of when crossovers are designated and how crossover interference is implemented remain unsolved (Pazhayam et al., 2021; Hunter, 2015).

1.4.3. Synaptonemal complex and crossover regulation

Crossover formation and the synaptonemal complex assembly are the hallmarks of meiosis and have been studied extensively. However, whether the synaptonemal complex is involved in crossover regulation remains one of the key questions which still needs to be addressed in the field (Pazhayam et al., 2021).

The relationship between crossover regulation and the synaptonemal complex was first proposed based on the observation that some organisms, such as fission yeast that lack a synaptonemal complex, also lack crossover interference (Kohli and Bähler, 1994). Similarly, interference only persists in regions of the uninterrupted synaptonemal complex in other species (Sym et al., 1993; Sym and Roeder, 1994; Hayashi et al., 2010; Libuda et al., 2013; Wang et al., 2015). This led to the formation of the polymerisation model in which the synaptonemal complex polymerization is the basis of the crossover interference signal (King and Mortimer, 1990). The contribution of the synaptonemal complex in crossover regulation was further supported by other studies (Hayashi et al., 2010; Libuda et al., 2013; Duroc et al., 2014; Voelkel-Meiman et al., 2015; Rog et al., 2017; Capilla-Pérez et al., 2021).

However, studies in budding yeast and mice led to the observation that interference is established prior to synapsis. Therefore, these findings suggested that previously seen defects are the results of the cycle progression defects (Pazhayam et al., 2021).

Given the importance of crossover regulation to ensure the correct segregation of chromosomes, understanding the mechanism of crossover regulation is critical to truly comprehending why errors in segregation occur and how they can be prevented. Mapping of crossover site requires a resolution below 100 nm (the width of the synaptonemal complex; Rog et al., 2017), which is well below the limit of conventional diffraction-limited light microscopy and calls for the use of techniques such as super-resolution microscopy or electron microscopy.

1.5. Fluorescence microscopy

1.5.1. Confocal microscopy

Confocal microscopy is an umbrella term for various fluorescent microscopy techniques that share a basic principle. Namely, only a diffraction-limited spot is illuminated and detected, preventing the contribution of out-of-focus light and increasing the achievable resolution Elliott (2020).

The individual techniques differ in the scanning method they use. Particularly, spinning disc microscopy includes the introduction of the Nipkow disc to increase the speed of image acquisition. The disc contains an array of equally spaced pinholes that allow for the simultaneous illumination and detection of many points. The increased acquisition speed makes the spinning disc microscopy suitable for the *in vivo* imaging. Furthermore, lower laser intensities required compared to other confocal microscopy techniques help prevent phototoxicity during the *in vivo* imaging (Oreopoulos et al., 2014).

1.5.2. Super-resolution microscopy techniques

The main advantage of light (fluorescence) microscopy over electron microscopy is the possibility of detecting components of interest using fluorescent markers. However, the resolution of conventional light microscopy is limited to the diffraction limit of light of approx. 250 nm. New techniques,

termed super-resolution microscopy, allow us to resolve two fluorescent signals separated by a distance smaller than the diffraction limit. Currently, the main methods for super-resolution microscopy are single-molecule localisation microscopy (SMLM; Rust et al., 2006; Betzig et al., 2006; Hess et al., 2006), stimulated emission depletion (STED; Hell and Wichmann, 1994) microscopy, structured illumination microscopy (SIM; Gustafsson, 2000), or expansion microscopy (ExM; Chen et al., 2015).

1.6. Single-molecule localisation microscopy

The advantage of the SMLM techniques for imaging macromolecular complexes, such as the synaptonemal complex, is the superior resolution power that can be achieved without artificially expanding a structure of interest. SMLM harnesses the blinking properties of specific fluorophores in order to resolve objects at the sub-diffraction level (Xu et al., 2013).

The basic idea is that only a subset of fluorophores will be turned on at a given time point. The sample is then imaged repeatedly over time, allowing for the separation and, thus, resolving spatially overlapped fluorophores in time. The final SMLM image is created by assigning each observed signal (blinking event) with its extrapolated centroid position. To this end, fitting a point spread function (PSF) to the obtained signals across all acquired images results in a set of localizations associated with the coordinates and other parameters (e.g. frame number, localization precision) determined by the fit (Lelek et al., 2021). Importantly, the localization precision for each fluorophore is limited by the fitting accuracy and a resolution of approx. 15 nm can be achieved (Betzig et al., 2006; Thevathasan et al., 2019).

However, the achievable resolution of SMLM can vary between the biological samples and is generally determined by several factors such as labelling density and the blinking characteristics of the fluorophore. The relationship between labelling density and resolution is rooted in the Nyquist-Shannon criterion. Namely, objects within two times the average label-to-label distance can not be reliably resolved, so a high labelling density is needed for high-resolution imaging. Furthermore, if the on-cycle of the fluorophore is too long, spatially overlapping fluorophores may always be captured together, and hence, they cannot be resolved (Xu et al., 2013). Due to these two requirements, imaging a suf-

ficiently large number of images to get the structure of big macromolecular complexes can take a few hours.

The downside of these long imaging times in SMLM is that samples tend to drift due to effects like the movement of the stage or the current within the buffer solution. On a sub-diffraction resolution level, even the slightest movement on a scale of 10 nm can substantially affect the deconvoluted image and must be corrected for. If the two channels are imaged sequentially, the sample movements might be too significant. Subsequently, if the drift correction methods are not robust enough, images of separate channels will not be accurately overlayed (Wang et al., 2014).

Since biological questions often require precise detection and localisation of multiple targets within the same sample, introducing imaging artefacts due to wrongful overlay is possible. Ratiometric imaging methods (Lampe et al., 2012; Bossi et al., 2008) circumvent this issue by allowing for simultaneous imaging of multiple fluorophores. The fluorophores have partially overlapping excitation and emission spectra, but splitting the emission fluorescence by a dichroic mirror will result in multiple channels between which the ratio of the intensities for individual fluorophores will differ. Each detected signal is thus subsequently assigned to its respective channel based on the ratiometric fluorescence intensity (Winterflood et al., 2015).

Additionally, the three-dimensional information is necessary for studying the organisation of macromolecular complexes. In SMLM imaging, incorporating a cylindrical lens into the optical path of the emitted light is used to encode information about the third coordinate of a fluorophore into the SMLM images (Liu et al., 2022). The cylindrical lens distorts the shape of the PSF of a fluorophore depending on its distance to the focal plane. Furthermore, the shape of the PSF differs if the fluorophore is below or above the focal plane. Hence, by analysing the signal's shape, its precise position in the *z*-plane can be extrapolated (Xu et al., 2013). This allows for imaging the three-dimensional organisation of macromolecular complexes, such as the synaptonemal complex.

However, SMLM imaging is limited to the dissected and fixed germline tissue. Consequently, the dynamics of the meiotic progression can not be observed by this technique. To gain insight into the different aspects of meiotic progression, the utilisation of different imaging modalities is necessary at

this point. To this end, the dynamics of individual meiotic factors can be observed *in vivo* by diffraction-limited microscopy, while 3D-SMLM imaging can reveal the ultrastructure of their assemblies.

2. Aims

For sexually reproducing organisms, assuring the correct segregation of chromosomes during meiosis is key to obtaining healthy progeny. Proper segregation requires that homologous chromosomes stay adherent to one another until the first division. This is achieved by the assembly of the synaptonemal complex between homologs. After the synaptonemal complex disassembles, physical links that arise from class I crossover provide the connection between homologs. An imbalance in crossover distribution may lead to errors in chromosome segregation, which can have devastating consequences on the health of the progeny (Zickler and Kleckner, 1999). The mechanisms that regulate the distribution of crossover sites must be elucidated to understand how these errors occur and how to prevent them. Designation of crossover sites in *C. elegans* and many other model organisms is proposed to occur in the context of the synaptonemal complex, and recent studies point to an active role of the synaptonemal complex in crossover regulation (Hayashi et al., 2010; Libuda et al., 2013; Wang et al., 2015; Pattabiraman et al., 2017; Woglar and Villeneuve, 2018; Morgan et al., 2021; Köhler et al., 2020; Zhang et al., 2021). However, the underlying mechanism of crossover designation and its precise timing are not fully elucidated.

Some studies provide evidence for early crossover designation during the earlier stages of pachytene (Libuda et al., 2013; Machovina et al., 2016). These studies propose that the designated crossover sites interact with the synaptonemal complex, resulting in a change in the organisation of the synaptonemal complex that provides the basis of a crossover interference signal along the length of the synaptonemal complex (Libuda et al., 2013; Machovina et al., 2016). However, more recent studies point towards later crossover designation at the onset of late pachytene (Woglar and Villeneuve, 2018; Zhang et al., 2021; Haversat et al., 2022) and propose alternative crossover interference mechanisms (Zhang et al., 2021).

This study aimed to investigate crossover designation timing and putative interactions between desig-

nated crossover sites and the synaptonemal complex that could elucidate the mechanism of crossover regulation. To this end, insights into different aspects of crossover designation are required:

- Firstly, to gain insight into the dynamics of the crossover designation, I employ *in vivo* confocal imaging of the pro-crossover marker COSA-1 (Yokoo et al., 2012) at recombination intermediates.
- Secondly, I aim to investigate changes in the ultrastructure of recombination intermediates that coincide with crossover designation. To this end, I will visualise the organisation organisation of the MutSγ complex component MSH-5 at super-resulution that was previously implicated in the stabilisation of the recombination intermediates and Holliday junction (Snowden et al., 2004; Pochart et al., 1997; Baudat and Massy, 2007; Lynn et al., 2007; Woglar and Villeneuve, 2018; Haversat et al., 2022).
- Furthermore, by elucidating the organisation of the synaptonemal complex at recombination sites by single-molecule localisation microscopy, I aim to investigate the interaction of designated crossover sites and the synaptonemal complex, which could help elucidate the mechanisms of crossover regulation.

These *in vivo* and *in situ* approaches require optimisation of the experimental procedure and specifically tailored data quantification. In line with this, additional aims of this study include:

1. Optimisation of previously reported immobilisation methods for *in vivo* imaging of the *C. elegans* germline.
2. Optimisation of the immunohistochemistry protocols of dissected and fixed *C. elegans* gonads to increase the compatibility with single-molecule localisation microscopy (SMLM) of the synaptonemal complex and recombination intermediates. This protocol was previously published in Čavka et al. 2022.
3. Developing a specifically tailored pipeline that would allow for the description of individual meiotic nuclei during the acquired timelapse movie of *in vivo* meiosis.

4. Re-purposing existing 3D-SMLM data analysis tools for the descriptive analysis of the organisation of SMLM localisation data of synaptonemal complex components and associated proteins.

To demonstrate the performance of the single-molecule localisation microscopy pipeline, the optimised immunohistochemistry protocol was employed to study the localisation of the newly identified components SYP-5/6 (Hurlock et al., 2020) and SKR-1/2 (Blundon et al., 2023) within the ultrastructure of the synaptonemal complex by dual-colour 3D-SMLM.

3. Materials and methods

3.1. *Caenorhabditis elegans* maintenance

All *Caenorhabditis elegans* animals were maintained under standard conditions. Briefly, worms were kept at 20°C on standard nematode growth medium agar inoculated with *Escherichia coli* OP-50 (Brenner, 1974). In this study, genome editing and other experimental procedures were performed on 18-24 h post L4 larval stage worms. All *C. elegans* strains used in this study are listed in Appendix A.

3.2. CRISPR/Cas9-mediated genome editing

CRISPR/Cas9-mediated genome editing was performed by micro-injection of pre-assembled CRISPR/Cas9 complex into the gonad of adult worms according to previously reported procedures (Cho et al., 2013; Paix et al., 2015; Ghanta and Mello, 2020). Specifics to individual CRISPR/Cas9-mediated genome editings performed for this study are listed in Appendix B.

Generally, worms were injected with a mix containing 1.5 µM of Cas9 enzyme (Alt-R™ S.p. Cas9 Nuclease V3, 1081058, IDT) in complex with a specific guide RNA[1], and varying concentrations (Appendix B) of a target specific repair template diluted in nuclease-free water (AM9939, ThermoFisher Scientific) or duplex buffer (11-01-03-01, IDT). Additionally, the mix contained 5 ngµL^{-1} of pCFJ90, and 2.5 ngµL^{-1} of pCFJ104 plasmids that served as co-injection markers (Frøkjær-Jensen et al., 2008).

Injected worms were separated on individual agar plates. Successfully injected animals were identified under a fluorescence stereomicroscope (SteREO Discovery.V8, Zeiss) by the expression of the Pmyo-2::mCherry::unc-54utr (pharynx) or Pmyo-3::mCherry::unc-54 (muscle wall) constructs from the co-injection markers. Fluorescent F1 animals expressing the co-injection markers were placed on in-

[1] Guide RNA is a duplex of a gene-specific CRISPR-RNA and the trans-activating CRISPR (tracr) RNA, Alt-R® CRISPR-Cas9 tracrRNA)

dividual plates until the first generation of the F2 progeny reached the adult stage. Subsequently, successful genome editing events were identified through genotyping PCR (polymerase chain reaction) (details in B) and further confirmed by Sanger sequencing (Sanger et al., 1977) provided by Eurofins Genomics Germany GmbH (Anzinger Str. 7a,85560 Ebersberg Germany).

3.3. Brood counts

Fusing fluorescent proteins, epitope tags, or self-labelling tags to proteins of interest may interfere with their function. Since all tagged proteins are crucial meiotic factors, alleles created by CRISPR/Cas9-mediated genome editing could potentially disturb normal meiotic processes. To confirm the fidelity of meiosis in all generated strains, I assessed the fertility of all strains by brood counts. In *C. elegans*, any mutation affecting the function of meiotic factors can be detected by a reduction in the viability of progeny (caused, e.g. by missegregation of autosomes) and/or an increase in the incidence of male progeny (caused by missegregation of sex chromosomes) (Lui and Colaiácovo, 2013).

For each strain, I placed six hermaphrodite worms at the L4 larval stage on six individual NGM agar plates with an OP-50 lawn. I transferred these parent worms to fresh plates every 24 hours for five days. I counted the laid eggs and hatched L1 larvae immediately after each transfer to determine the brood size. Once the progeny reached adulthood, I assessed the number of the surviving and the male progeny. For each initial parent, I determined the viability of the progeny (the total count of surviving progeny divided by the total brood size) and the incidence of males (the total count of male progeny divided by the total count of surviving progeny). In all experiments, I also included the wild-type isolate (Bristol N2) as a control strain.

I compared the mean viabilities of the progeny of each assessed strain and the control strain using a Wilcoxon rank sum test. In contrast, the mean incidence of males were compared by a one-sided Wilcoxon rank rum testing if the incidence of males was significantly higher than in the control strain. Statistical analysis was performed using a *compare_means* function from *ggpubr* R (R Core Team, 2019) package (version 0.6.0, Kassambara 2023).

3.4. Cytology

3.4.1. Poly-L-lysine coated coverslips

To increase the adhesion of mounted tissue (Mazia et al., 1975), I coated the coverslips for super-resolution imaging with poly-L-lysine. To this end, I washed the coverslips (Precision coverslips, 24 mm, PK26.1, Carl Roth GmbH) for 20 min in ethanol and rinsed them in milliQ water. Once the coverslips were dry, I plasma-cleaned them (PlasmaPrep2, GaLa Instrumente GmbH) and applied 120 µL of 0.01% (w/v) aqueous poly-L-lysine (30,000-70,000 Da, P2636-25MG, Sigma-Aldrich) solution on each coverslip. I let the coating assemble for 10-20 min at room temperature. Afterwards, I rinsed the coverslips in milliQ water and left them at room temperature until completely dry. The poly-L-lysine coated coverslips were stored at 4°C and used within four weeks after preparation (Hurlock et al., 2020; Li et al., 2022; Čavka et al., 2022; Blundon et al., 2023).

3.4.2. Conjugation of F(ab')$_2$ fragments with organic fluorophores

Primary amines, mainly lysine residues, of F(ab')$_2$ fragments are commonly conjugated with organic fluorophores through a chemical reaction with commercially available succinimidyl (NHS) ester derivatives (Hermanson, 2013). When labelling F(ab')$_2$ fragments, I largely followed the labelling protocols suggested by the manufacturers of the succinimidyl (NHS) ester reactive fluorophores.

F(ab')$_2$ fragments used to obtain the results displayed in the chapter 4 were labelled according to the protocol that I have previously described in Čavka et al. (2022). For the remaining experiments, unless stated otherwise, I combined 27 µL of 0.6-0.7 mgmL^{-1} F(ab')$_2$ fragment in phosphate-buffered saline (PBS, 13.7 mM NaCl, 0.27 mM KCl, 1 mM Na_2HPO_4, 1.8 mM KH_2PO_4, pH 7.4), 3 µL of 0.1 M $NaHCO_3$ (pH 8.3), and 3 µL of 1 mM succinimidyl (NHS) ester reactive fluorophore in DMSO. In all the labelling reactions, I kept the molar ratio of final F(ab')$_2$ fragment and reactive fluorophore at around 1:18. To maximise protein recovery, the reaction mixture was assembled in a microcentrifuge tube with low propensity of protein binding (Protein LoBind® tubes, 0.5 mL, 0030108094, Eppendorf). I mixed the reaction solution by pipetting and incubated for one to two hours at room temperature protected from

light. To inactivate residual free fluorophore, I added 1.5 µL of 1 M Tris-HCl (pH 7.5) solution. $F(ab')_2$ fragments were then separated from the remaining free fluorophores using a desalting column (Zeba™ Spin Desalting Columns, 40K MWCO, 0.5 mL, 87766, ThermoFisher Scientific) that I had previously equilibrated with PBS. I stored the labelled $F(ab')_2$ fragments protected from light at 4°C and used them within 3 months after labelling.

3.4.3. Feeding worms with HaloTag ligands conjugated with fluorescent organic dyes

C. elegans worms at L4 larval stage were picked 18-24 hours before the planned *in vivo* imaging or dissection. At 12-15 hours before imaging, I transferred the worms to fresh NGM agar plates inoculated with 20-30 µL OP-50 bacteria[2] in M9 buffer (22 mM KH_2PO_4, 42 mM Na_2HPO_4, 85.5 mM NaCl, 1 mM $MgSO_4$, Sulston and Hodgkin 1988) containing 0.2% Tween® 20 containing 10 µM HaloTag ligand[3] Additional details on the HaloTag ligands used are listed in Appendix D.

3.4.4. Immunohistochemistry of Caenorhabditis elegans germline tissue

I dissected and fixed the germline tissue of age-matched *C. elegans* animals according to previously described protocols (Phillips et al., 2009; Crittenden et al., 1994). Briefly, 13-20 worms were dissected in a 30 µL droplet of Egg buffer (25 mM HEPES, 118 mM NaCl, 48 mM KCl, 2 mM EDTA, 0.5 mM EGTA, pH 7.4, Edgar 1995) with 0.2% (v/v) Tween® 20 (P9416-50ML, Sigma-Aldrich/Merck) and 0.02% (w/v) tetramisole hydrochloride (T1512-2G, Sigma-Aldrich/Merck). The dissection allowed the germline tissue to extrude from the body of the worms. Subsequently, an equal volume of fixative solution (4% (w/v) paraformaldehyde (Pierce 16% (w/v) formaldehyde, methanol free, 28906, ThermoFischer Scientific), 25 mM HEPES, 118 mM NaCl, 48 mM KCl, 2 mM EDTA, 0.5 mM EGTA, pH 7.4) was added to the droplet containing the dissected worms. Fixation was stopped after 1 min by transferring the dis-

[2] OP-50 bacteria for feeding HaloTag ligand were prepared by pelletting 1 mL overnight culture, washing with 1 mL M9 buffer, and resuspending the pellet in 100 µL

[3] 1 mM HaloTag ligand stock solutions were prepared by dissolving the fluorescently labelled HaloTag ligands in DMSO at 1 mM. The solution was split into single-use aliquots and kept frozen at -80°C until used.

sected worms to a PCR tube filled with Tris saline buffer (20 mM Tris-HCl, 150 mM NaCl, pH 7.5) with 0.1% (v/v) Tween® 20 (TBST). Residual active fixative was quenched by three washes with TBST, followed by two additional washes in phosphate saline buffer (PBS, 13.7 mM NaCl, 0.27 mM KCl, 1 mM Na2HPO4, 0.18 mM KH2PO4, pH 7.4) with 0.1% (v/v) Tween® 20 (PBST)[4], 1 min incubation in -20°C methanol, and two final PBST washes to remove methanol (Čavka et al., 2022).

To reduce unspecific binding of the antibodies, samples were blocked in 1XRoche blocking buffer (prepared in PBST, 11096176001, Roche) for 45-90 min at room temperature. Incubations with primary antibodies diluted in 1XRoche blocking buffer were done overnight at 4°C. The following day, I removed unbound primary antibodies by three 10-15 min washes in PBST. Subsequently, samples were stained with full-length secondary antibodies or their $F(ab')_2$ fragments conjugated with fluorescent organic dyes. For this, samples were incubated for 2 hours at room temperature in secondary antibody solutions diluted in 1XRoche blocking buffer[5]. The subsequent steps of sample preparation differ depending on which fluorescent microscopy method was used to image the samples as described below.

Confocal imaging

For confocal imaging, unbound secondary antibodies were removed with two 5-10 min washes in PBST, followed by a 10 min DNA staining in DAPI (D9542-1MG, Sigma-Aldrich/Merck) 0.1 ugmL^{-1} solution in PBST, and two additional 5 min washes in PBST. Finally, the samples were mounted between a glass slide (Fisherbrand Microscope slides T/F Ground 0.8-1.0 mm thick, 7107, Fisher scientific) and a coverslip (Circular cover glass 18 mm No. 1.5, LH23.1, Carl Roth) in 18 µL of mounting medium (Invitrogen ProLong Glass Antifade Mountant, P36982, ThermoFischer Scientific). Samples were kept overnight at room temperature, protected from light to cure the mounting medium. Unless stated otherwise, samples were imaged on the following day.

[4] I performed additional washes with PBST to remove Tris-HCl from the samples to prevent it from interfering with the later post-fixation step.

[5] For details on antibody concentrations and associated fluorophores for each experiment please consult the Appendix D

Super-resolution imaging

Super-resolution imaging, especially the single-molecule localisation microscopy technique, requires the sample to be closely attached to the coverslip (Čavka et al., 2022). For this reason, I have developed and optimised a protocol that is specifically tailored for mounting the *C. elegans* germline tissue for the super-resolution imaging (**Figure 3.1**, Čavka et al. 2022). Briefly, after removing unbound secondary antibodies with two 10 min washes in PBST, I post-fixed the samples in 2% paraformaldehyde (v/v) in PBS on poly-L-lysine coated coverslips (section 3.4.1). To covalently attach the germline tissue to the coverslip, I transferred the dissected tissue to the drop of the fixative solution on the poly-L-lysine coated coverslip and covered the droplet with a smaller coverslip (Circular cover glass 12 mm No. 1, Menzel-Gläser; 1,631-0713, VWR). Any excess of the fixative solution was removed with a piece of filter paper, and samples were left in the dark for 5 min at room temperature. The fixation was stopped by transferring the coverslip *"sandwich"* on an aluminum block placed on the dry ice. After 20-60 min, the smaller coverslip was removed with a razor (*freeze-crack* method).

For samples imaged by STED microscopy, the coverslip was picked up, *sample-up* with a glass slide containing a 20 µL drop of mounting medium (Invitrogen ProLong Glass Antifade Mountant). Samples were then left overnight at room temperature for the mounting medium to cure. Afterwards samples were stored at 4°C, and imaged within a week of mounting.

For SMLM imaging, samples were dipped in ice cold PBS or -20°C methanol post-*freeze-crack*, additionally rinsed in PBS, and stored in PBST until imaging. Immediately before the imaging (within a week after sample preparation), samples were mounted on a custom-made holder in imaging buffer and sealed with parafilm as previously suggested by Hoess et al. 2018 and Diekmann et al. 2020. The imaging buffer was freshly prepared by combining a 1 mL aliquot of buffer base (50 mM Tris-HCl, pH 8.0, 10 mM NaCl, 10% D-Glucose) with 53 µL enzyme mix (1916 UmL^{-1} glucose oxidase (Sigma G7141), 42350 UmL^{-1} catalase (Sigma C3155), 50 mM Tris-HCl pH 8.0, 51% glycerol) and 7-13 µL of 5 M 2-mercaptoethylamine (MEA, 30070-10G Sigma-Aldrich) pH 8.7.

Samples were prepared following an older version of the protocol to determine the localisation and orientation of SYP-5/6 proteins (section 4.2). Here, the dissected tissue was attached to the coverslip

immediately during the first 1 min fixation step that followed the dissection. This procedure is described in Hurlock et al. 2020. Consequently, the blocking and antibody solutions were applied to the coverslips with attached tissue and not within a PCR tube containing freely floating dissected tissue.

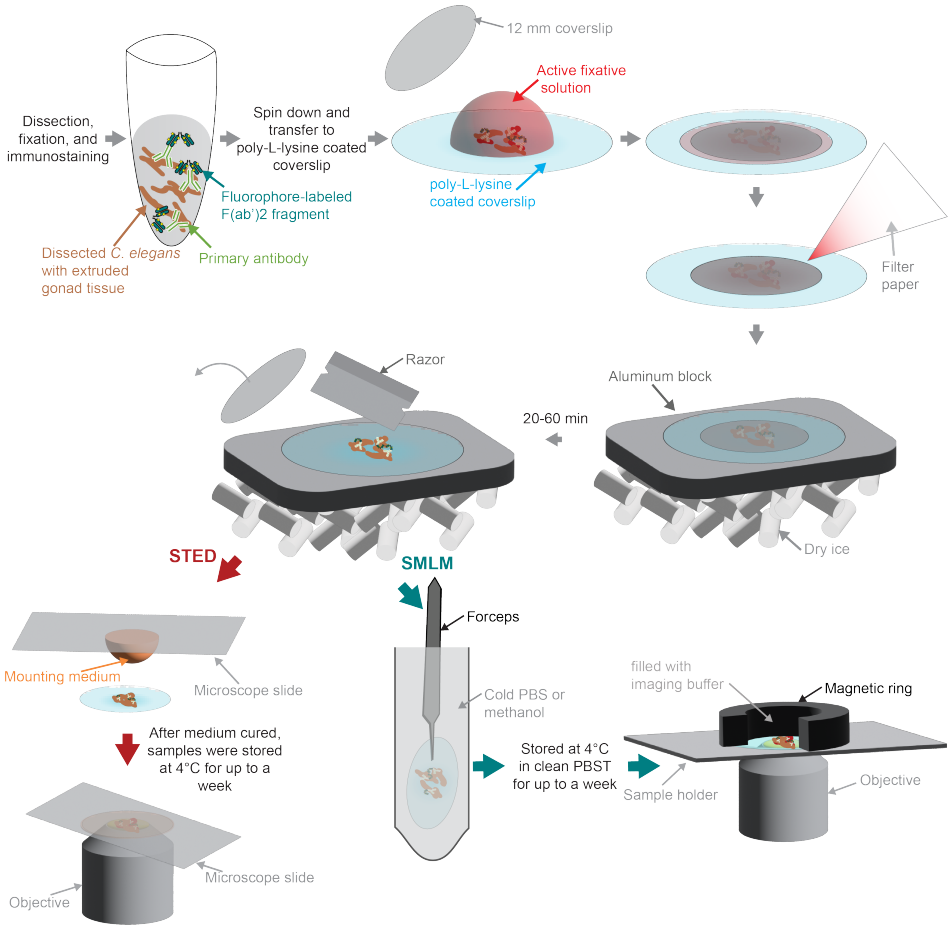


Figure 3.1. Mounting of *C. elegans* dissected tissue for super-resolution microscopy
Graphics indicate individual steps of the mounting procedures that are connected with grey arrows. The steps that differ between single-molecule localisation microscopy (SMLM) and stimulated emission depletion (STED) microscopy are indicated by dark-cyan (SMLM) and dark-red (STED) arrows. The figure is adapted from Čavka et al. 2022, and was originally made by me.

3.4.5. Confocal imaging of fixed germline tissue

Confocal microscopy images in section 5.5 were obtained with an Olympus IXplore SpinSR spinning-disk confocal microscope. I used a PLAPON 60X (NA 1.42) oil immersion objective combined with 3.2X post-magnification, and a SoRa spinning disk. For imaging, the 405 nm excitation laser was

used at the 10% power, the 488 nm laser was used at 40% power, while the 561 nm and 640 nm lasers were used at 5% and 30% power, respectively. A camera exposure time of 100 ms was used for the 405 nm, 561 nm, and 640 nm channels, while an exposure time of 200 ms was used for the 488 nm channel. The microscope was controlled via the OLYMPUS cellSens Dimension software (version 3.2). The image shown in the figure was prepared using the Fiji software (Schindelin et al., 2012). Specifically, maximum intensity projection images of the individual tiles were stitched using the Grid/Collection stitching (Preibisch et al., 2009) Fiji plugin to create the images of whole *C. elegans* gonads.

3.4.6. Stimulated emission depletion microscopy

I performed the stimulated emission depletion (STED) microscopy imaging together with Dr. Dietrich Walsh, an applications specialist with EMBL Imaging Centre (Heidelberg 69126, Germany).

Images displayed in the section 4.1 were acquired on Leica Stellaris 8 STED FALCON system equipped with a white light laser, a 775 nm pulsed STED laser, and the FALCON Fluorescence Lifetime IMaging (FLIM) module. The system offers enhanced resolution power when compared to traditional STED systems by accounting for the variation of fluorescence lifetimes in different areas of the depletion *doughnut*. Additionally, I used FLIM enhanced TauSTED module to remove background signal based on the differences in the fluorescence lifetime of the dye in the nucleoplasm versus fluorophore confined within the synaptonemal complex following the advice from the experts. Enhancing the contrast through removal of the background signal further improves the resolution achievable by the system. Samples were imaged with a HCPLAPOCS2 100x (NA 1.40) oil immersion objective. For excitation of the AlexaFluor 594 (A37572, ThermoFischer Scientific), the 580 nm laser at 4% power was used, while the 635 nm excitation laser at 3% power was used to image STAR 635P (ST635P-0002-1MG, Abberior). The 775 nm STED depletion laser power was used at 40% power. The Leica HyD X detectors were used in counting mode with a gain value of 10 for photon detection. The scan rate was 100 Hz, at a pixel size of 17 nm. TauSTED acquisition were performed in four-line accumulation mode (Čavka et al., 2022). LAS X software was used for the microscope control and image processing (contrast

enhancement).

3.4.7. Single-molecule localisation microscopy (SMLM)

SMLM imaging

All SMLM acquisitions in this study were performed at room temperature using two different custom-built microscopes built by the members of Ries group (EMBL) and Dr. Rory M. Power (EMBL Imaging Centre), respectively. The microscopes have similar configurations (Deschamps et al., 2016; Deschamps and Ries, 2020; Deschamps et al., 2023; Diekmann et al., 2020). The main differences include the camera type, the astigmatic lens, the available objectives, and the module used to achieve a homogeneous laser illumination (Schröder et al., 2020; Stehr et al., 2019). **Table E.1** in appendix E provides a list of the different 3D-SMLM microscope configurations used in this study. Generally, the astigmatism required for 3D imaging was achieved by introducing a cylindrical lens (SMLM Ries Group) or a compound cylindrical lens (SMLM EMBL Imaging centre). The dual-color acquisition was achieved by ratiometrically splitting the emission light by a 665 nm long-pass dichroic mirror and by filtering the transmitted and reflected photons by a 685/70 nm (SMLM Ries Group) or 700/100 nm (SMLM EMBL Imaging centre) and a 676/37 nm filter, respectively. Both reflected and transmitted emissions were recorded as separate channels at distinct parts of the same EMCCD (SMLM Ries Group) or sCMOS (SMLM EMBL Imaging centre) camera. The details about the individual components and control of the SMLM microscopes can be found in previously published scientific articles as listed in **Table E.1**.

All SMLM acquisitions were performed following the advice for acquisition and result interpretation from Dr. Jonas Ries, Dr. Philipp Hoess, Dr. Takahiro Deguchi, other members of the Ries group, and Dr. Rory M. Power. Briefly, I located the germline tissue on the coverslip under bright-field illumination. While exposing the sample to 638 nm illumination at very low irradiance in rising mode (pulse length between 3,000-5,000), I focused the objective on the bottom-most section of the germline with stretches of the synaptonemal complex. I then exposed the field of view to 638 nm illumination at high irradiance of about 13 $kWcm^2$ until an appropriate fluorophore blinking rate was achieved. Subse-

quently, 150,000-250,000 frames were acquired with an exposure time of 20-30 ms and 13-20 kWcm^2 irradiance. In some acquisitions, I used automated fluorophore activation by a UV laser at a ~3 kWcm^2 in rising mode with maximum pulse length set to 10,000 (Deschamps and Ries, 2020). The specific laser power, exposure times, and number of acquired frames for each experiment are listed in **Table D.2** (Appendix D).

SMLM image reconstruction and post-processing

SMLM image reconstruction and post-processing was performed as previously suggested by Mund et al. 2018, 2023, Li et al. 2022, and Diekmann et al. 2020. All SMLM images analysed in this study were reconstructed from the raw data using the SMAP software (Super-resolution Microscopy Analysis Platform, Ries 2020). With the exception of the SMLM images used for mapping the orientation of SYP-5/6 proteins[6], I used the global fitting algorithm globLoc (Li et al., 2022) using an experimental PSF model, and linking all three coordinates of the emitters between the two channels. The experimental astigmatic PSF model and the transformation between the two channels were generated with the *calibrate3DsplinePSF* plugin of the SMAP software (Ries, 2020) from z-stack images of fluorescent beads (TetraSpeck Microspheres, T7279, ThermoFischer Scientific). This microscope calibration was performed for each SMLM experiment (Li et al., 2018).

The reconstructed images were corrected for sample drift using a custom algorithm based on redundant cross-correlation within the SMAP software (Ries, 2020) as described in (Mund et al., 2023). Additionally, I removed dim and out-of-focus emitters by filtering the localisations according to their localisation precision and their *z* position, respectively. I only used localisations with *z* position within a range from -300 to 300 nm, and with a localisation precision above 10 or 15 nm in lateral (*xy*) and 25 or 30 nm in axial (*z*) direction. The channel assignment of the individual localisations was performed according to their relative brightness in the two channels (Lampe et al., 2012; Bossi et al., 2008). The super-resolved image were rendered in the SMAP software (Ries, 2020) by plotting Gaussians at the fitted positions with a width proportional to their localisation precision and assigning the color based on the assigned channel (Mund et al., 2018; Hurlock et al., 2020; Diekmann et al., 2020; Mund et al.,

[6]Please consult Hurlock et al. 2020 for details on the reconstruction of these images.

2023; Blundon et al., 2023). To assess the quality of the SMLM images, I estimated their Fourier ring correlation (FRC) resolution (Nieuwenhuizen et al., 2013; Banterle et al., 2013) with the FRC resolution plugin in the SMAP software (Ries, 2020). For the plots displayed in **Figure 4.1**, the original FRC curves were smoothed with functions from the *ggplot2* package (Wickham, 2016) as previously described in Čavka et al. 2022.

3.5. *In vivo* imaging of crossover designation in *C. elegans*

3.5.1. Sample preparation

As a master student in the Köhler lab, Emine Berna Durmus had made an effort to optimise a mechanical immobilisation method (Gomez and Schvarzstein, 2018) for long-term imaging of C. elegans meiosis. This optimisation effort was later continued by an intern, Lauren (Mickey) Sloat. I have acquired all the timelapse movies for this study, largely following this optimised protocol.

Briefly, I pipetted 40 µL of 7% (w/v) agarose (Invitrogen UltraPure™ Agarose-1000, 16550100, ThermoFisher Scientific) solution in MilliQ water onto a vinyl record, covered it with a glass slide, and left it to form a gel. Importantly, tape was used to create spacers between the record and the glass slide. By casting gels on the record, channels roughly corresponding to the width of the worms, were formed in the agar (Gomez and Schvarzstein, 2018). After the gel was polymerised, I lifted it from the record and covered it with *agarose soaking solution* (20 mM serotonin creatinine sulfate monohydrate (H7752-1G, Sigma-Aldrich), 0.002% (w/v) of tetramisole hydrochloride in M9). The gel was left in a humid chamber to incubate in the soaking solution for at least 30 min. The agarose pad was then dried with a tissue and cut into smaller pieces (approximately a quarter or smaller). The cutout was placed onto a 12 mm coverslip, and worms were mounted within the channels. Subsequently, I transferred the pad with worms on a metallic lid of a glass test tube, and added 3-4 droplets (approx. 2 µL) of *mounting solution* (20 mM serotonin solution in M9 buffer, or simply M9 buffer) around the pad. The coverslip and the pad were then picked up with an imaging dish with a glass bottom (µ-Dish 35 mm, high Glass Bottom,

81158, Ibidi). To keep the sample from drying out I placed wet tissue rolled up in a ring around the plastic edge inside the dish, away from the agarose pad. The *agarose soaking* and *mounting solution* that contained serotonin were always freshly prepared on the day of imaging.

For *in vivo* imaging of crossover designation, I imaged a *C. elegans* worm strain expressing SYP-1 tagged with mNeonGreen (Shaner et al., 2013) fluorescent protein, and pro-crossover factor COSA-1 N-terminally tagged with HaloTag7 (Los et al., 2008). Additionally, the strain contains deletions in the *gur-3* gene (*ok2245*), and a point mutation in *lite-1* gene (*ce314*). The two mutations compromise the locomotion in response to blue and UV light (Bhatla and Horvitz, 2015). The worms were fed (section 3.4.3) with a specific HaloTag ligand conjugated with a JF639 organic dye that was developed by Claire Deo (Deo et al., 2021).

3.5.2. Confocal imaging

Timelapse images were acquired at 20°C with an Olympus IXplore SpinSR spinning-disk confocal microscope. I used a UPLSAPOS100X (NA 1.35) silicon oil immersion objective combined with a CSUW1 -TS 2D 50 µm spinning disk. Both fluorescent reporters were excited simultaneously by a 488 nm laser at 2-7% power, and a 640 nm laser at 35-70% power. Emitted fluorescence was subsequently split into two separate channels by a 561 nm long-pass dichroic mirror. The two channels were imaged on two separate sCMOS cameras. Additionally, the light of the reflected and transmitted channels was passed through a 525/50, and a 685/40 band-pass filter, respectively. The microscope was controlled through the OLYMPUS CellSens Dimension software (version 3.2).

In the following sections, I describe the data analysis of the microscopy data. First, I list the methods I used to describe the organisation of synaptonemal complex components and MutSγ component (MSH-5) within super-resolved images acquired by STED or SMLM microscopy. This is followed by the description of a custom analysis pipeline for segmentation, foci detection, and tracking used to identify and describe the changes in the number of HALO::COSA-1 foci within in vivo timelapse movies acquired by confocal microscopy.

3.6. Aligning the line profiles of regions of interest in STED images

As reported in Čavka et al. 2022, I generated line profiles of regions of interest that contain the synaptonemal complex in frontal or slightly tilted views with Fiji ImageJ (Schindelin et al., 2012) to assess the localisation of components within the synaptonemal complex in STED images. To quantify the line profiles, I wrote a custom R script (version 4.1.2): Individual line profiles were fitted with double gaussians to determine the distances between the antibodies SYP-5::HA or HTP-3. Next, line profiles of the synaptonemal complex in frontal view were aligned to create an averaged profile. To determine the localisation of SYP-5::HA or HTP-3 within the synaptonemal complex in frontal view (**Figure 4.3B**), the signal within the averaged profiles were also fitted with bi-modal gaussian distribution (Čavka et al., 2022).

3.7. Data analysis for the 3D-single molecule localisation microscopy data

3.7.1. Mapping positions and orientation of SYP-5/6 proteins by 3D single-molecule localisation microscopy

As reported in Hurlock et al. 2020, I selected individual regions of interest containing the synaptonemal complex in frontal view in dual-color SMLM images of late-pachytene nuclei to map the localisation of SYP-5 and SYP-6 within the synaptonemal complex. Frontal views of the synaptonemal complex were identified by the presence of two clearly separated, parallel and straight stretches of HIM-3 localisations[7]. The number of individual stretches and the total length of the annotated regions of the synaptonemal complex are listed in Appendix F. Subsequently, I rotated and aligned the individual stretches using a custom script in R (version 3.6.0). To determine the positions of individual domains of both SYP-5 and SYP-6, I fitted the densities of aligned localisations in frontal (x) and cross-sectional (z) views by unimodal or bimodal gaussian distributions. In doing so, I was able to obtain peak-to-peak

[7] Examples can be seen in the Appendix F

distances (d, for bimodal distributions only) and widths (HWHM, half width at half maximum). Standard deviations of these parameters were determined by a bootstrapping approach that was previously described in Köhler et al. 2017 (Hurlock et al., 2020).

3.7.2. Localisation of SKR-1/2 within the substructure of the synaptonemal complex

To assess the localisation of SKR-1/2 within the synaptonemal complex, I manually annotated the midlines of the synaptonemal complex stretches using the *plot3D_annotate* plugin of SMAP software (Ries, 2020) as reported in Blundon et al. 2023. SMLM localisations around the annotated polyline were straightened, aligned, and rendered to create frontal and cross-sectional views displayed in **Figures 4.6** and **4.5**.[8] Subsequently, I used the *Line profiles* plugin in SMAP (Ries, 2020) to determine the profiles of the straightened localisations along the *x* and *z* axes. I used a 2 nm bin width to calculate the histograms. These histograms were then fitted by a mono- or bi-modal Gaussian distribution for each ed synaptonemal complex component to describe their distributions within the annotated regions. Finally, I visualised the histogram counts and the fitted Gaussian distributions with a custom R (version 4.4.2) script in which I used the *ggplot2* package (Wickham, 2016). This analysis is also described in (Blundon et al., 2023).

3.7.3. Straightening of SMLM localisations along an annotated polyline

To straighten synaptonemal complexes within 3D-SMLM images, I specified individual regions of interest that contained a single continuous stretch of the synaptonemal complex (**Figure 3.2A**). The midline of each stretch was traced with a 3D-polyline (**Figure 3.2B**, *step 1*). Subsequently, the points of the polyline were interpolated by a 3D cubic Hermit spline and equidistantly spaced (15-25 nm, **Figure 3.2B**, *step 2*: orange line) points were sampled along the spline using the *interparc* MATLAB function written by John D'Errico (D'Errico, 2012). This new interpolated set of points (from here onward

[8] More details about the custom MATLAB script that I wrote to straighten and align the SMLM localisations are described in the following subsection 3.7.3.

midline[9]; **Figure 3.2B**, *step 2*) was used to further limit the region of interest by only considering localisations within 350 nm of the *midline* for further analysis. To create straightened and aligned views of multiple synaptonemal complexes (**Figure 3.2B**, *step 4*), SMLM localisations in individual stretches were assigned to the closest segment of the *midline* and rotated according to a local tangent and tilt of the chromosome axes localisations (**Figure 3.2B**, *step 2-3*).

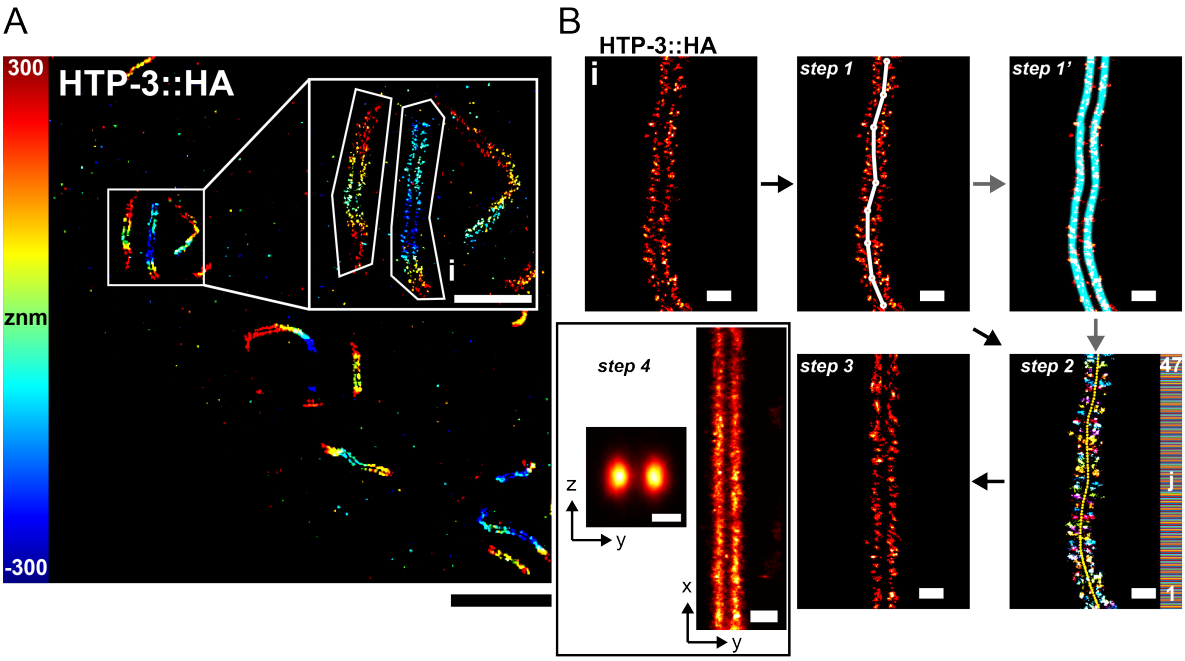


Figure 3.2. Workflow to straighten SMLM localisations along an annotated polyline

(A) 3D-SMLM image showing the bottom-most section of a *C. elegans* germline stained for the C-terminus of HTP-3 (anti-HA antibody targeting HTP-3::HA) with SMLM localisations coloured by their respective *z*-coordinate. The inset shows a zoomed-in view of the nucleus outlined by the white square. White polygons in the inset specify individual regions of interest each containing a continuous stretch of a synaptonemal complex. Scale bars: 5 µm (black), 1 µm (white). **(B)** The *midline* of each individual stretch is annotated with a polyline (*step 1*). Subsequently, equidistantly spaced (15-25 nm) points were sampled along a spline (*step 2*, orange line) and the surrounding SMLM localisations were divided into 47 segments. Individual segments were rotated and aligned to create a straightened view of the region of interest (*step 3*). Multiple continuous stretches were processed and combined to create averaged images of the synaptonemal complex in frontal (*step 4*, right), or cross-sectional view (*step 4*, left). Since the quality of the straightening procedure greatly depends on how well the annotated polyline describes the true midline of the synaptonemal complex, the coordinates of the original polyline can also be optimised by fitting a maximum likelihood model of a ribbon-like model (cyan in top-right panel, *step 1'*) to the SMLM localisations using LocMoFit framework (Wu et al., 2022). In that case, *step 2* is performed after step *step 1'*. Scale bars: 100 nm. All panels were rendered using the SMAP software (Ries, 2020).

[9]Therefore, this *midline* corresponds to the midline of the synaptonemal complex (**Figure 1.3**)

Specifically, the equidistantly spaced points along the *midline* are defined as

$\mathcal{K} = \{\boldsymbol{P_i} = (x_i, y_i, z_i) \mid i = 1, 2, 3, ..., m\},$

where m is the number of *midline* points.

I then sub-selected a set of SMLM localisations that are within 350 nm of this *midline* creating

$\mathcal{L} = \{\boldsymbol{L_i} = (x_i, y_i, z_i, \lambda_i) \mid i = 1, 2, 3, ..., n\}.$

Here, each point $\boldsymbol{L_i}$ represents a single SMLM localisation defined by its 3D coordinates (x_i, y_i, z_i) and its localisation precision λ_i.

To divide the localisations $\mathcal{L}$ into $(m - m\,mod\,2)/2$ segments, individual segments

I_k ($k = 2, 4, ..., (m - m\,mod\,2)/2$)

were defined by a set of three consecutive *midline* points

$\mathcal{K}_k = \{\boldsymbol{P_i} = (x_i, y_i, z_i) \mid i \in \{k-1, k, k+1\}$ and $k = 2, 4, .., m - m\,mod\,2\}$

(**Figure 3.3 A**). This approach enables me to define each I_k as a space between two segment-specific planes R_{start} and R_{stop} that are defined by their normal vectors. These normal vectors of both planes are co-linear to the local tangent ($\boldsymbol{r_k}$, equation 3.2). The planes are positioned such that they pass through the first ($\boldsymbol{P_{k-1}}$) and the last ($\boldsymbol{P_{k+1}}$) point of the $\mathcal{K}_k$ segment, respectively.

Iterating $k = 2, 4, ..., (m - m\,mod\,2)/2$, I defined subsets of localisations $\mathcal{S}_k$ that are confined within the space of each I_k segment (**Figure 3.3 A**, red-filled circles). Details of the localisation assignment to the individual segments are outlined in **Algorithm 1**.

After their assignment to the corresponding segment, the localisations in $\mathcal{S}_k$ were centred around $\boldsymbol{P_k}$ and aligned to the *x*-axis by a standard 3D-rotation matrix (Altmann, 1986):

$$R_k(\mathbf{u}, \phi) = \begin{pmatrix} cos\phi + u_x^2(1 - cos\phi) & u_x u_y(1 - cos\phi) - u_z sin\phi & u_x u_z(1 - cos\phi) + u_y sin\phi \\ u_y u_x(1 - cos\phi) + u_z sin\phi & cos\phi + u_y^2(1 - cos\phi) & u_y u_z(1 - cos\phi) - u_x sin\phi \\ u_z u_x(1 - cos\phi) - u_y sin\phi & u_z u_y(1 - cos\phi) + u_x sin\phi & cos\phi + u_z^2(1 - cos\phi) \end{pmatrix} \tag{3.1}$$

where vector $\boldsymbol{u} = (u_x, u_y, u_z)$ is a cross product of the unit vector that lays on the *x*-axis ($\boldsymbol{x} = (1, 0, 0)$) and the numerically calculated and normalised local tangent $\boldsymbol{r_k}$ of the corresponding *midline* segment:

$$\boldsymbol{r_k} = \frac{\boldsymbol{P}_{k+1} - \boldsymbol{P}_{k-1}}{\|\boldsymbol{P}_{k+1} - \boldsymbol{P}_{k-1}\|} \tag{3.2}$$

The angle ϕ in equation 3.1 is defined by:

$$\phi = -arccos\left(\frac{\boldsymbol{x}\cdot\boldsymbol{r_k}}{\|\boldsymbol{x}\|\|\boldsymbol{r_k}\|}\right) \tag{3.3}$$

Since the synaptonemal complex is not rotationally symmetric but can also rotate along its *midline* (e.g. frontal vs. cross-sectional views), an additional transformation is required to align the segments into a consistent view of the synaptonemal complex. The orientation of the synaptonemal complex within each individual segment can be estimated by measuring the tilt between two parallel localisation bands formed by a component of the chromosome axes (HIM-3, HTP-3, or HTP-3::HA depending on the experiment).

Specifically, when a subset $\mathcal{A}_k$ of localisations in $\mathcal{S}_k$ that correspond to the chromosome axis channel ($\mathcal{A}_k \subset \mathcal{S}_k$) are projected onto the normal plane at point $\boldsymbol{P_k}$, two separate clusters of projections ($\mathcal{A}'_k$) corresponding to each chromosome axis can be distinguished (**Figure 3.3 B**). Irrespective of the orientation of the synaptonemal complex within the given segment, the polar angles (azimuths) of the two cluster centres should be separated by approximately 180°. However, depending on the orientation of the synaptonemal complex the two clusters will be tilted about the origin by a different angle (θ_k). I implemented two different methods to estimate the angle of an individual segment(θ_k):

The first method (suggested to me by Dr. Jonas Ries) estimates the angle of each segment as a cyclic average of polar angles (azimuths) of the chromosome axes localisations projected onto the normal plane ($\mathcal{A}'_k$, **Figure 3.3 B**). The polar angles of individual localisations were additionally weighted by weights inversely proportional to the corresponding localisation precision. I used a MATLAB function written by Dr. Jonas Ries (Ries, 2020) to calculate this cyclic average.

The second method relies on clustering of the projected localisations ($\mathcal{A}'_k$, **Figure 3.3 B**) into two clusters that correspond to each of the two chromosome axis localisation groups contained within a segment. The angle is subsequently estimated from a line fitted through the centres of the two clusters. The clustering is performed using MATLAB's Gaussian mixture model function (*fitgmdist*). To increase the robustness of the clustering, the initial parameters for the Gaussian mixture model fit were specifically selected for each segment. Namely, the coordinates of the means of the initial model were chosen by fitting the data with a line and selecting the two points of the fitted line that lay 60 nm away

from the origin in each direction for the first segment. For the following segments, the final fit of the previous segment was used as the initial set of parameters for the Gaussian mixture model fit.

The performance of both methods greatly depends on the proper selection of localisations that form the $\mathcal{A}_k$ set, and on how well the original polyline (**Figure 3.2 B, *step 1***) describes the true *midline* of the synaptonemal complex. To enhance the performance, the manually annotated polyline could be additionally optimised to better fit the true *midline* of the synaptonemal complex (section 3.7.4; Figure 3.2 B, grey arrows).

Additionally, the localisations within the region of interest can be filtered to remove sporadic localisations from nucleoplasmic background staining. To this end, I used the *alphaShape* MATLAB function to create a bounding volume of the localisations from $\mathcal{L}$. localisations that truly constitute the synaptonemal complex could be successfully grouped into a larger object using an appropriate α radius I of 25-40 nm, while neighbouring sporadic localisations were grouped into secondary, smaller objects and subsequently removed from the $\mathcal{A}_k$ set of localisations based on this association. This filtering method allowed the removal of sporadic localisations (e.g. **Figure 3.3 A**, red coloured circles without outlines) that could not be excluded by their distance to the *midline* without also removing localisations that truly correspond to the synaptonemal complex stretch within the region of interest.

Finally, to align the segments in a consistent view of the synaptonemal complex, localisation within them was additionally rotated by the matrix in equation 3.4 and stacked according to the corresponding cumulative segment length from the first polyline point to the point $\boldsymbol{P_k}$.

$$R(\theta_k) = \begin{pmatrix} 1 & 0 & 0 \\ 0 & cos(\pi - \theta_k) & -sin(\pi - \theta_k) \\ 0 & sin(\pi - \theta_k) & cos(\pi - \theta_k) \end{pmatrix} \tag{3.4}$$

Algorithm 1 Assigning SMLM localisations to each individual segment (I_k)

Input:

Midline segment specified by the set of three polyline points $\mathcal{K}_k = \{\boldsymbol{P_i} = (x_i, y_i, z_i) \mid i \in \{k-1, k, k+1\}\}$, each of which is specified by its coordinates.

A set of points $\mathcal{L} = \{\boldsymbol{L_i} = (x_i, y_i, z_i, \lambda_i) \mid i = 1, 2, 3, ..., n\}$, where each point $\boldsymbol{L_i}$ represents a SMLM localisation defined by its 3D coordinates (x_i, y_i, z_i) and its localisation precision λ_i. A Pre-selection radius H_0 is used to reduce the computation time.

Index (k) of the *midline* point that is regarded as the central point of $\mathcal{K}_k$.

Output:

Set of localisations $\mathcal{S}_k$ assigned to the segment I_k where $\mathcal{S}_k \subset L_k$.

$\mathcal{S}_k \leftarrow \{\}$ ▷ Initiate $\mathcal{S}_k$ as an empty set

$\mathcal{B}_k \leftarrow \{\boldsymbol{L} \in \mathcal{L} \mid \|\boldsymbol{L} - \boldsymbol{P}_k\| \leq H_0\}$ ▷ Pre-select points within H_0 of the polyline point $\boldsymbol{P_k}$

$\boldsymbol{r_k} \leftarrow (\boldsymbol{P}_{k+1} - \boldsymbol{P}_{k-1})/\|\boldsymbol{P}_{k+1} - \boldsymbol{P}_{k-1}\|$ ▷ Numerical calculation of the tangent

$R_{start} \leftarrow$ a plane defined by its normal vector co-linear to $\boldsymbol{r_k}$ and point $\boldsymbol{P}_{k-1}$

$R_{stop} \leftarrow$ a plane defined by its normal vector co-linear to $\boldsymbol{r_k}$ and point $\boldsymbol{P}_{k+1}$

for each $\boldsymbol{L} \in \mathcal{B}_k$ **do**

  if k is not the first or the last segment **then**

    if $\boldsymbol{L}$ lies between planes R_1 and R_2 **then**

      if $\boldsymbol{L}$ selected in earlier segments **then**

        if $\boldsymbol{L}$ is closer to current $\boldsymbol{P_k}$ than the one corresponding to a previous segment **then**

          $\mathcal{S}_k \leftarrow \mathcal{S}_k \cup \boldsymbol{L}$

        end if

      else if $\boldsymbol{L}$ is so far only selected for segment k **then**

        $\mathcal{S}_k \leftarrow \mathcal{S}_k \cup \boldsymbol{L}$

      end if

    end if

  else if k is the first polyline segment **then**

    if $\boldsymbol{L}$ and $\boldsymbol{P}_k$ are on the same side of the plane R_2 **then**

      $\mathcal{S}_k \leftarrow \mathcal{S}_k \cup \boldsymbol{L}$

    end if

  else if k is the last polyline segment **then**

    if $\boldsymbol{L}$ and $\boldsymbol{P}_k$ are on the same side of the plane R_1 **then**

      $\mathcal{S}_k \leftarrow \mathcal{S}_k \cup \boldsymbol{L}$

    end if

  end if

end for

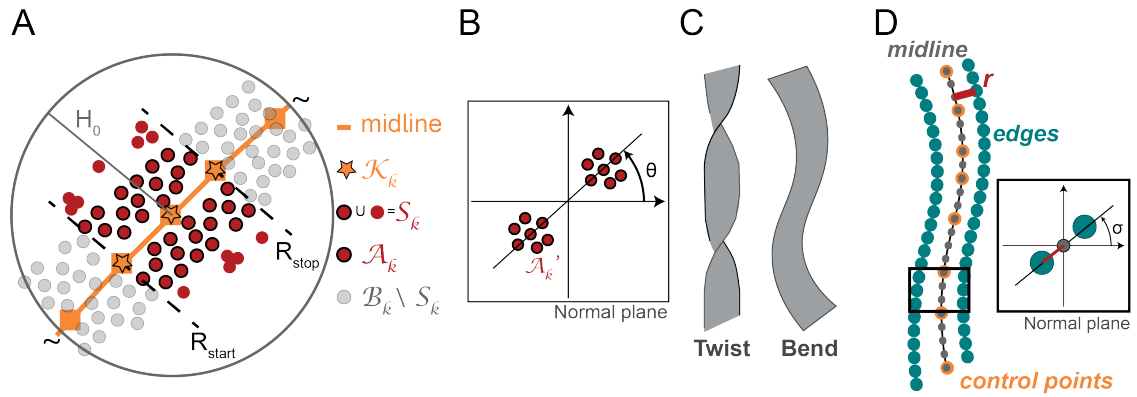


Figure 3.3. Describing the shape of chromosome axes in single-molecule localisation microscopy images

(A) SMLM localisations are divided into individual segments of the synaptonemal complex ($\mathcal{S}_k$). To this end, the *midline* of a continuous stretch of the synaptonemal complex is first defined by a set of equidistantly spaced points (orange rectangles connected by a line; the *midline* continues beyond the illustration ("~"). Since the orientation of the synaptonemal complex varies along the length of the stretch, the continuous stretch is divided into segments. Each segment is defined by three consecutive *midline* points (orange stars, $\mathcal{K}_k$), where k is the index of the central point ($\boldsymbol{P_k}$). Only localisations between the planes R_{start} and R_{stop} are assigned to the segment (red circles, $\mathcal{S}_k$), whilst the remaining localisations (grey circles) are assigned to a previous or following segment. R_{start} and R_{stop} (black dashed lines) are defined by their normal vectors and associated points. The normal vectors of both planes are co-linear to the local tangent, and the planes are positioned such that they pass through the first and the last point of the $\mathcal{K}_k$ segment, respectively. To save computation time, only localisations within a sphere with radius H_0 from the centre $\boldsymbol{P_k}$ are considered ($\mathcal{B}_k$) for assignment to the segment I_k. Additionally, sporadic localisations (red circles without outline) are removed to increase the robustness of the angle calculation. **(B)** A schematic illustrating the angle of the tilt between two chromosome axes (θ) that is estimated from projections ($\mathcal{A}_k'$) of axis component localisations onto a normal plane of the *midline*. **(C)** Illustration of twisting and bending of a ribbon. **(D)** Cartoon illustrating the main features of a ribbon-like model used to optimise the annotated 3D-polyline (subsection 3.7.3) by maximum likelihood fitting of the model to the SMLM localisations of the chromosome axes (Wu et al., 2022). The final model consists of edges (dark cyan) that are discrete points generated by symmetrically placing two points on both sides of each *midline* point. The placement of each pair of points depends on the constant r (ribbon's half-width, red line) and an angle (σ). The 3D coordinates of the control points, together with r, and angles for each segment, are the parameters of the model.

3.7.4. Describing the shape of a continuous stretch of the synaptonemal complex in SMLM images

When chromosome axis components are stained and imaged by super-resolution microscopy (**Figure 3.2 A**) their localisation signal consists of two tracks that resemble the edges of a ribbon. This ribbon-like structure the synaptonemal complex bends and twists along its length (**Figure 3.3 C** and **Figure 3.2 A**). To describe this behaviour, I estimated changes in the angle between the consecutive segments of chromosome axes (twist) and the curvature of the *midline* of the synaptonemal complex (bend).

To find the true midline of the synaptonemal complex stretch, the coordinates of the annotated 3D-polyline were further optimised (**Figure 3.2 B**, *step 1'*). To this end, I used the maximum likelihood model fitting framework LocMoFit developed by Dr. Yu-Le Wu in the Ries group (Wu et al., 2022). Specifically, I adapted a geometric model used for quantitative analysis of SMLM localisations of microtubules (Wu et al., 2022) into a ribbon model (**Figure 3.2 B** *step 1'* and **Figure 3.3 D**).

The model is defined as $f(\boldsymbol{p})$ where $\boldsymbol{p}$ is a set of model parameters that include the 3D coordinates of n control points that define the ribbon's *midline* ($\{x_i, y_i, z_i \mid i = 1, 2, 3, ..., n\}$), a half-width of the ribbon (r), and a set of angles ($\{\sigma_j \mid j = 1, 2, 3, ..., n-1\}$) describing the orientation of the edges within each segment bounded by two neighbouring control points (**Figure 3.3 D**). To create the discrete model ($f(\boldsymbol{p})$), the control points were fitted with a 3D cubic Hermit spline, and equidistant points were sampled along the spline (*midline*)[10]. I also assigned an angle describing the local tilt of the axis to each *midline* point. This angle was kept constant for each segment. The final model was composed by generating two points on each side of the individual *midline* point based on the segment's angle and the parameter r (60 or 65 nm).

The maximum likelihood model fit was initialised with control points corresponding to the points of a manually annotated polyline (**Figure 3.2 B**, *step 1*). Consequently, the number n of control points varied between different stretches of synaptonemal complexes. The parameter space was then searched to find a set of control points ($\{x_i, y_i, z_i \mid i = 1, 2, 3, ..., n\}$) and angles ($\{\sigma_j \mid j = 1, 2, 3, ..., n-1\}$) that best describe the SMLM localisations of the chromosome axes through maximum likelihood model

[10] The distance between the sampled points depends on the localisation precision of the data, and was typically between 15-25 nm.

fitting (Wu et al., 2022). The half-width of the ribbon r was kept constant at 60 or 65 nm which corresponds to the expected half width of the chromosome axes (Köhler et al., 2017).

In addition to these parameters described above that are intrinsic to the ribbon-like model, the model $f(\boldsymbol{p})$ also includes extrinsic parameters that are integral to LocMoFit (Wu et al., 2022). These include parameters describing rigid transformations and re-scaling of the model. However, these model transformations were turned off by fixing the corresponding parameters. Additionally, a parameter describing the uncertainty (Wu et al., 2022) of the model was set to 25 nm which blurs the model resulting in a wider edge as depicted in *step 1'* in **Figure 3.2 B**.

Subsequently, I used the optimised *midline* to divide the synaptonemal complex into segments (**Figure 3.2 B**, *step 1'-2*). On each segment, I estimated the angle and width between the two axis bands. This allowed me to describe changes in the width of the synaptonemal complex along its length, and sudden changes in the orientation of the axes between two consecutive segments (twisting). Additionally, I estimated the curvature of the optimised *midline* to estimate the bending of the synaptonemal complex. These optimisations are described below.

Quantifying bending of the synaptonemal complex

The bending of the synaptonemal complex is estimated as curvature (κ) of the 3D cubic Hermit spline that is fitted to the model's *midline* and is calculated for each point of the *midline* as:

$$\kappa = \frac{\|\boldsymbol{c'(t)} \times \boldsymbol{c''(t)}\|}{\|\boldsymbol{c'(t)}\|^3} \tag{3.5}$$

where $\boldsymbol{c(t)}$ is a curve describing the model's *midline*[11].

Quantifying twisting of the synaptonemal complex

To describe the twisting of the synaptonemal complexes, I estimated the axis angle for each segment of the model's *midline* as described in the previous subsection 3.7.3. Since the angle is estimated within a $[0, \pi]$ range, discontinuities are introduced into the phase angle along an analysed stretch of the synaptonemal complex. To correct these discontinuities, the phase angles were shifted when the

[11] $\boldsymbol{c(t)} =< X, Y, Z >=< f(t), g(t), h(t) >$, where f, g, and h represent 3D cubic Hermit spline that describe the 3D-coordinates of points that constitute the model's *midline*

difference between two consecutive angles was larger than $\frac{2\pi}{3}$[12], resulting in a continuous sequence of phase angles. To describe the twisting of the axes, I calculated the differences of the phase angles along the length of the *midline*. When chromosome axes gradually twist around each other, the difference in phase angles between consecutive segments is small. However, when a sudden twist occurs within a short distance, the difference in phase angles becomes large.

Quantifying width of the synaptonemal complex

To assess the variability of the width of the synaptonemal complex along a continuous stretch, I estimated the distance between the two chromosome axes localisations for each segment (**Figure 3.2 B**, *step 3*). To this end, the localisations were first projected onto a normal plane (**Figure 3.3 B**) and rotated to correct for the angle (θ_k) as described by the matrix $R(\theta_k)$ in equation 3.4. The width was then estimated by fitting a bi-modal gaussian distribution to a histogram (binwidth = 5 nm) profile of the projected and rotated localisations.

Code availability

The MATLAB code for the SMLM data analysis described in sections 3.7.3-3.7.4 is integrated into a plugin for the *ROIManager* of the SMAP software (Ries, 2020), and is available via the GitHub repository (https://github.com/jries/SMAP, *ic_develop* branch).

3.7.5. Describing the super-resolved organization of the MSH-5::V5 at recombination intermediates

To visualise the ultrastructure of recombination intermediates using 3D-SMLM, I imaged meiotic nuclei stained for the C-terminus of the crossover factor MSH-5 (anti-V5 antibody to visualise the V5 epitope tag of MSH-5::V5) and the C-terminus of the chromosome axis component HTP-3 (HTP-3::HA). I imaged nuclei at various stages during the pachytene stage. Hence, the MSH-5::V5 localisations will correspond to different stages of homologous recombination. To roughly time the individual recombi-

[12] If the angle identity is switched from one segment to the next, the estimated difference will be inflated since the angle artificially changes by approx. pi rad. Due to the spread of the chromosome axes corresponding SMLM localizations and resulting variability of the angle estimate, I choose a lower threshold of $\frac{2\pi}{3}$ (compared to pi) to rather underestimate than overestimate the observed change. Importantly, the extremely abrupt twists in the axes usually correspond to approx. $pi/2$ rad, so with the chosen threshold, I do not expect a significant underestimation of the angle change.

nation intermediates seen within the SMLM images, each nucleus was assigned with the number of remaining rows of nuclei until the end of pachytene.

Maximum likelihood fitting of the ellipsis

To describe the size of SMLM localisation clusters of antibodies bound to MSH-5::V5 at recombination intermediates and designated crossover sites, I selected individual regions of interest containing the synaptonemal complex in frontal to slightly tilted view in dual-color SMLM images with MSH-5::V5 in the AlexaFluor647, and HTP-3::HA in the CF660C/CF680 channel. Subsequently, localisations in the AlexaFluor647 channel were described by maximum likelihood fitting of an elliptical model (Wu et al., 2022). The fit was initialised by an elliptical model with a centre in the median coordinates of MSH-5::V5 localisations within the region of interest. Major and minor axes of the model were optimised from their initial values (35 and 65 nm respectively) while allowing for the model to be translated within the region interest or rotated around all three axes. Translation and rotation of the model are described by extrinsic parameters integral to the LocMoFit framework (Wu et al., 2022). I inspected the regions of interest for sites where the fit converged, and ellipsis engulfed the MSH-5::V5 localisations. Other sites were disregarded when plotting the major and minor axis using functions from *ggplot2* (Wickham, 2016).

DBSCAN Clustering of MSH-5::V5 localisations around the annotated polyline

To identify the significant sites of MSH-5::V5 localisations. The localizations within 350 nm around the ribbon model's *midline* (subsections 3.7.3 and 3.7.4) were clustered using the DBSCAN clustering algorithm (Ester et al., 1996)[13]. The identified clusters were additionally filtered based on the distance of their centre to the *midline*. Only clusters within 120 nm of the model's *midline* were identified as possible recombination intermediates and further inspected. I also discarded clusters that were of low quality[14] or corresponded to background (nucleoplasmic) signal.

The sites of MSH-5::V5 localisations within a 400 nm square around the cluster's centre were anno-

[13] To perform clustering, I used the *dbscan* MATLAB function with *epsilon neighbourhood* of 100 nm and *minimum number of neighbours required for a core point* set at 20

[14] Cluster that was potentially cut when filtering out localisations outside of the ±300 nm range from the focus plane (out-of-focus emitters filter, subsection 3.4.7)

tated and fitted with the elliptical model described in the previous section 3.7.5. Furthermore, each cluster was assigned a position along the *midline* of the associated synaptonemal complex stretch. To this end, a position of the cluster was equivalent to the cumulative arclength of the *midline* point closest to the cluster's centre. This allowed me to compare the organisation of the chromosome axes component HTP-3 as a function of the distance to a recombination intermediate or designated crossover.

3.7.6. Describing the super-resolved organization of HTP-3::HA at recombination sites

Variations in width, bending, and angle were calculated along the *midline* as described in section 3.7.4 and used as shape parameters to describe changes in the chromosome axes along the chromosomes as a function of the distance from a recombination intermediate. For each shape parameter, sliding windows of a specified size were sampled along the synaptonemal complex of interest. Cumulative distributions of the mean shape parameters were compared between windows that are adjacent to a recombination intermediate or a designated crossover, and all other windows sampled along the *midlines* of analysed stretches.

I plotted the results of these analysis using a custom R script that utilises the *ggplot* (Wickham, 2016) and *dplyr* (Wickham et al., 2023) packages.

3.8. Data analysis for the *in vivo* imaging of *C. elegans* germline

3.8.1. Quantification of the number of COSA-1 foci within individual meiotic nuclei

To track changes in the number of recombination intermediates within nuclei during meiotic progression, I visualised the pro-crossover factor COSA-1 using a self-labelling HaloTag taking *in vivo* timelapse movies of *C. elegans* (section 3.5). I then used a specifically tailored analysis pipeline by combining available segmentation, foci detection, and tracking tools to quantify the number of HaloTag::COSA-1 foci within each nucleus over time.

In the first step, I used cellpose2.0 (Stringer et al., 2020; Pachitariu and Stringer, 2022) to segment meiotic nuclei within a 3D image based on the blurred (Gaussian blurring, sigma=3.5) SYP-1-containing channel. To this end, I used a segmentation model trained by Dr. Simone Köhler to segment meiotic nuclei within *C.elegans* tissue based on the fluorescently labelled synaptonemal complex or chromatin signal. The identified 3D objects were filtered based on their size to remove partial and joint nuclei or aberrant structures. Additionally, I estimated the sphericity of each object (Φ, equation 3.6)[15] and removed objects with an estimated sphericity below 0.75 to remove crescent-shaped leptotene/zygotene nuclei.

$$\Phi = \frac{\sqrt{36\pi V^2}}{A} \tag{3.6}$$

The filtered segmentation masks and a channel containing the HaloTag::COSA-1 signal were fed into the spotMAX software (developed by Dr. Francesco Padovani in the Schmoller Lab at Helmholtz Zentrum in Munich) to identify HaloTag::COSA-1 foci within each 3D object (nucleus) that was identified by cellpose2.0. The parameters used to detect individual HaloTag::COSA-1 by spotMAX are listed in the **Table 3.1**. The detected foci were further filtered to remove falsely identified foci based on their size, shape, and Glass' delta effect size describing the difference between the signal of a detected focus and the background. SpotMAX then returns the parameter *A-fit*[16] was used as an estimate of foci brightness and is used synonymously with intensity in sections 5.1-5.3.

Both segmentation and foci detection are performed separately on individual frames of the timelapse movie. To track the changes within individual nuclei over time, I used the Fiji Plugin TrackMate (Tinevez et al., 2017; Ershov et al., 2021). Specifically, I used the linear assignment problem (LAP) tracker, disallowing merging or splitting of the tracks. The parameters used varied between timelapse movies[17] and typical values are listed in **Table 3.2**. Additionally, final tracks were inspected and manually corrected as necessary.

[15] V denotes the volume of a segmented 3D-object calculated by multiplication of voxel count and voxel size, while A corresponds to the surface of a mesh generated from the individual 3D-object using functions from the *scikit-image* (van der Walt et al., 2014) collection of algorithms for image processing in Python (Van Rossum and Drake, 2009).

[16] Parameter of a 3D gaussian fitted to each identified focus that correlates with the intensity of the peak.

[17] TrackMate parameters were varied depending on the movement of the imaged *C. elegans* animal.

To combine the results of spotMAX and TrackMate I wrote a custom Python script, while a custom R script was used for data exploration and visualisation of the results.

Table 3.1. SpotMAX parameters used to detect individual HaloTag::COSA-1 foci

spotMAX foci detection parameter	Value
Spots reporter emission wavelength [nm]	650
Spot minimum z-size [µm]	0.481
Resolution multiplier in y- and x- direction	0.82
Aggregate cells prior analysis	TRUE
Remove hot pixels	TRUE
Initial gaussian filter sigma	0
Sharpen spots signal prior detection	TRUE
Spots detection method	peak_local_max
Spots segmentation method	Thresholding
Spot detection threshold function	threshold_triangle
Optimise detection for high spot density	FALSE
Compute spots size	TRUE

Table 3.2. Typical TrackMate parameters used to track meiotic nuclei during timelapse movies of *Caenorhabditis elegans* germline

TrackMate parameter	Value
ALLOW_TRACK_SPLITTING	FALSE
ALLOW_TRACK_MERGING	FALSE
LINKING_MAX_DISTANCE [µm][18]	7-10
GAP_CLOSING_MAX_DISTANCE [µm][18]	10-20
MAX_FRAME_GAP[18]	3-5
LINKING_FEATURE_PENALTIES	{'POSITION_Y': 2.,'POSITION_Z': 15.,'RADIUS': 7.}
GAP_CLOSING_FEATURE_PENALTIES	{'POSITION_Y': 2., 'POSITION_Z': 7.,'RADIUS': 5.}

3.8.2. Determining the position of meiotic nuclei within the germline

To align germlines from multiple timelapse movies, I used principal component analysis (PCA) on the centroids of the segmentation masks. The germlines were then rotated such that the axis of meiotic progression is parallel to the *x*-axis [19]. The central line of the gonad was approximated by local

[18] Ranges of typically used values are listed.

[19] To increase the robustness of the rotation, PCA was performed on objects that were not as stringently filtered as described in section 3.8.1. This meant that joint, partial, and transition zone (leptotene/zygotene) nuclei to determine the proper rotation were included for the alignment of the germlines.

polynomial regression fitting (*loess* function in R) of the rotated coordinates of the centroids. Subsequently, each meiotic nucleus (3D segmented object) was assigned with its corresponding position on the germline centre line. Additionally, the positions of the nuclei on the centre line were centred on the transition from mid- to late pachytene. This mid-to-late transition point was set to correspond to the point where the nucleus-wide mean *A-fit* parameter suddenly increased. The direction of the sudden increase was used to identify the orientation of the gonad. Late pachytene nuclei were assigned to positions greater than 0, whilst nuclei in the earlier stages were assigned positions lower than 0. Data handling was performed using a custom R script that relied on the use of several R (R Core Team, 2019) packages (*dplyr* (Wickham et al., 2023),*minpack.lm* (https://CRAN.R-project.org/package=minpack.lm), *numDeriv* (https://cran.r-project.org/package=numDeriv), *reshape2* (Wickham, 2007), *tidyverse* (Wickham et al., 2019)).

3.8.3. Mean intensity and number of HaloTag::COSA-1 foci per nucleus

Using a custom R script, I calculated the mean of *A-fit* (subsection 3.8.1) parameter of HaloTag::COSA-1 foci belonging to each nucleus. Data for the first timeframe of three timelapse movies were collected and the mean *A-fit* parameter and number of foci values were plotted along the position of the nucleus within the gonad (section 3.8.2) using functions from *ggplot2* (Wickham, 2016).

Four nuclei around the transition from mid- to late-pachytene were selected from one of the timelapse movies and inspected closer to quantify changes in the number of foci and mean foci intensity (*A-fit*) during the timelapse. Additionally, I inspected the distribution of HaloTag::COSA-1 foci along individual chromosomes of these four nuclei (see below).

3.8.4. Quantifying the distribution of HaloTag::COSA-1 foci along individual chromosome

To describe the distribution of HaloTag::COSA-1 foci along individual chromosomes, I manually traced the SYP-1::mNeonGreen signal of all six chromosome pairs for four nuclei of interest using the BigTrace v.0.2.1 plugin for Fiji (https://github.com/ekatrukha/BigTrace). Traces were further processed

and individual foci identified by spotMAX were assigned to the closest synaptonemal complex trace (**Figure 3.4**) by a custom Python script that relies on several Python libraries (*NumPy* (Harris et al., 2020), *Pandas* (The *pandas* development team, 2020), *scikit-image* (van der Walt et al., 2014), *scikit-learn* (Pedregosa et al., 2011), *SciPy* (Virtanen et al., 2020), *tifffile* (https://pypi.org/project/tifffile/)). Briefly, raw traces from BigTrace were smoothed using the spline interpolation from *SciPy* (Virtanen et al., 2020). I then sampled equidistant points (120 nm spacing) along the processed traces[20]. Next, I assigned the HaloTag::COSA-1 foci to the trace by finding the minimal distances between the coordinates of HaloTag::COSA-1 given by spotMAX and the points along the trace. Importantly, I corrected the coordinates of the foci for the offset between two channels in the timelapse movie of *C. elegans* germline prior to this assignment of the foci to the trace of the synaptonemal complex (**Figure 3.4** and **3.5A**).

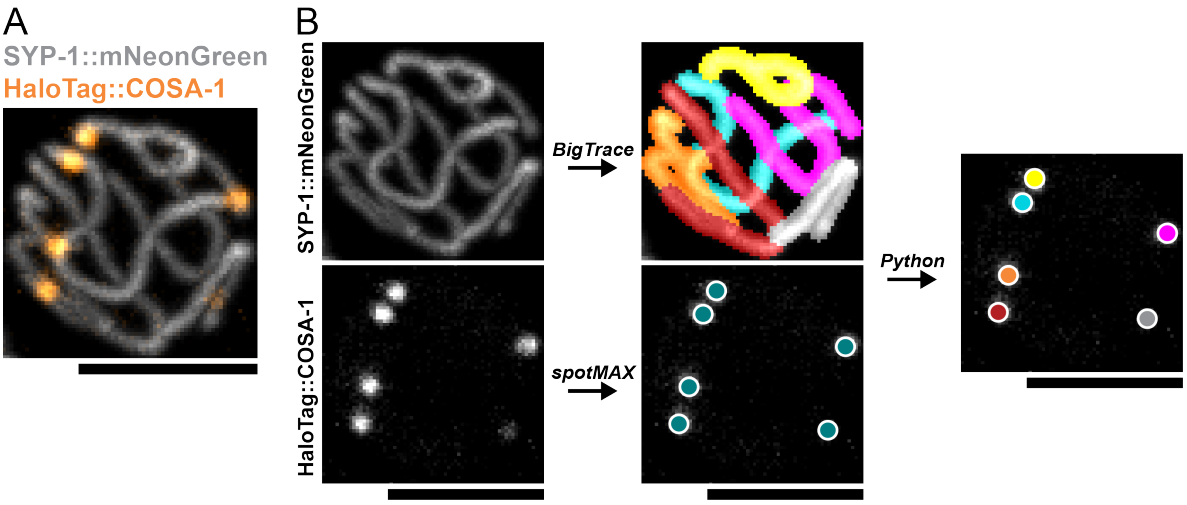


Figure 3.4. Association of HaloTag::COSA-1 foci to individual synaptonemal complexes
(A) Maximum intensity projection image of a late pachytene meiotic nucleus with mNeonGreen (Shaner et al., 2013) fused to the synaptonemal complex component SYP-1 (SYP-1::mNeonGreen) and HaloTag7 (Los et al., 2008) fused to the crossover marker COSA-1 (HaloTag::COSA-1). **(B)** SYP-1::mNeonGreen signal of all six chromosome pairs was manually traced using BigTrace v.0.2.1 (https://github.com/ekatrukha/BigTrace) plugin for Fiji (top), while individual HaloTag::COSA-1 foci were detected by spotMAX that is developed by Dr. Francesco Padovani in the Schmoller Lab at Helmholtz Zentrum in Munich. Subsequently, a custom Python script was used to assign individual foci to the closest synaptonemal complex trace (right-most panel). Scale bars: 3 µm.

[20] I used a custom Python function that was based on the MATLAB function *interparc* (D'Errico, 2012).

For this colour correction, I used a custom Python function that estimates the offset based on the correlation of maximum intensity projections of normalised and thresholded channels of individual frames of the timelapse movie. The correction was performed consistently for all time frames in all three directions using shift values estimated in most frames. To determine the offset along the *z*-axis, maximum intensity projections along the *y*-axis were used, while offsets in *x* and *y* direction were estimated on maximum intensity projections along the *z*-axis.

Once the foci are associated to individual synaptonemal complexes, I calculated their position relative to the start of the trace. Importantly, when tracing the synaptonemal complex through different frames, I kept the start of the trace consistent at a single end of the synaptonemal complex. For this reason, I could identify the regions of the synaptonemal complex with persistent or transient association of HaloTag::COSA-1 foci (**Figure 3.5**).

Specifically, the position of a focus along the trace was equivalent to the cumulative segment length from the start of the trace to the point of the trace associated with the focus (**Figure 3.5 A**). Subsequently, I defined an interval around the position associated with a focus ($\pm$ resolution limit) in each time frame. Overlapping intervals across multiple frames were grouped and tagged as containing *persistent*, *blinking*, or *fading* foci (**Figure 3.5 B**).

To illustrate the distribution of HaloTag::COSA-1 foci along the traced synaptonemal complexes, I used the parameters from 3D gaussian fitted in spotMAX to create *intensity* profiles along each trace. To this end, the intensity profile along a single trace in a specific time point is given by:

$$I(\mu_i, \sigma_i, Afit_i) = \sum_{i=1}^{n} Afit_i \cdot e^{\left(\frac{x-\mu_i}{2\sigma_i}\right)^2} \tag{3.7}$$

where n is the number of foci associated to the trace, whilst μ_i, σ_i, and $Afit_i$ denote the position along the trace, the fitted standard deviation[21], and the intensity (subsection 3.8.1) of each focus, respectively. The final intensity profile (I) is a sum of 1D gaussian distributions that describe individual foci.

The visualisation of the results and the classification of HaloTag::COSA-1 focus associated regions

[21] I used the mean standard deviation in *x*- and *y*-direction fitted by spotMAX.

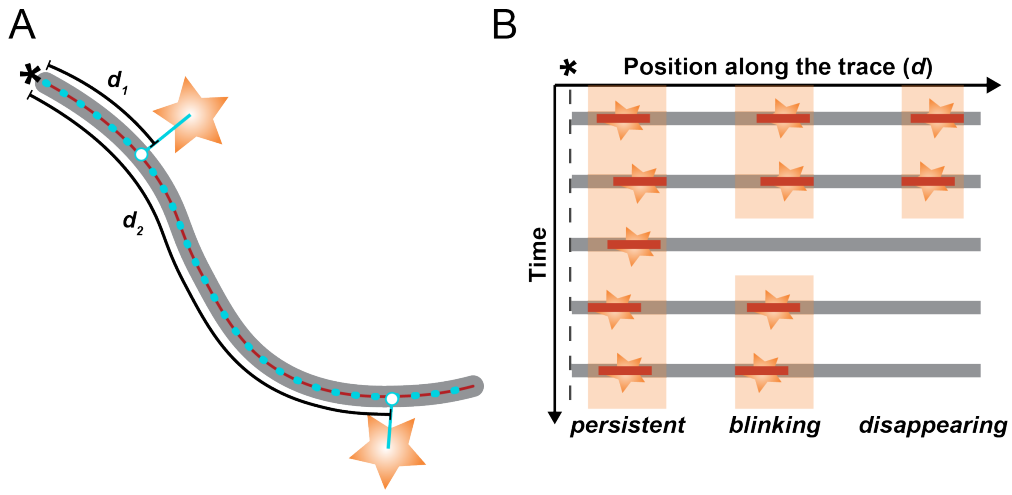


Figure 3.5. Describing the dynamics of HaloTag::COSA-1 foci along traced synaptonemal complexes

(A) Individual synaptonemal complexes (grey) are traced manually. The raw trace is fitted with a 3D cubic spline represented by a dark red line, and equidistantly spaced points are sampled along the spline (cyan points). The distances between HaloTag::COSA-1 foci (stars) and equidistantly spaced points are calculated, and individual foci are associated with their closest point along the trace (highlighted by white-filled circles with cyan outline). The position of a HaloTag::COSA-1 focus along the trace (d_1 and d_2) is equivalent to the cumulative distance from the start of the trace (indicated by *) to the focus-associated point. **(B)** To track individual foci along individual synaptonemal complexes, I defined intervals corresponding to the resolution limit around the coordinates of individual foci ($\pm$ resolution limit, red bars). Foci within overlapping intervals across time frames were grouped to create regions of the chromosome traces associated with COSA-1 foci (transparent orange rectangle). In this way, HaloTag::COSA-1 foci were effectively tracked over time. Depending on their presence or absence in the analysed frames, the foci were classified as *persistent*, *blinking*, or *fading*.

along synaptonemal complex traces were performed with a custom R script using *ggplot* (Wickham, 2016), *dplyr* (Wickham et al., 2023), *IRanges*, and *GenomicRanges* (Lawrence et al., 2013).

3.8.5. Additional image processing

All individual time frames of meiotic nuclei displayed in chapter 5 were corrected for photo-bleaching by histogram matching using the *scikit-image* (van der Walt et al., 2014) library for Python (Van Rossum and Drake, 2009). Additionally, the displayed images were enlarged 4-fold using Fiji (Schindelin et al., 2012).

Individual chromosomes were cropped from 3D *z*-stacks of meiotic nuclei that were previously resized

to isotropic voxel size. For this purpose, I used the *resize*[22] function from the *scikit-image* Python library (van der Walt et al., 2014). Subsequently, the voxels within a mask created around the trace (**Figure 3.4 B**, top-middle panel)[23] were selected to create images of individual chromosomes.

[22]Before resizing, images were convolved with a gaussian smoothing filter that is part of the *resize* function.

[23]The masks were created by selecting voxels that are within 1.75*resolution limit of the trace.

4. Super-resolution microscopy of the synaptonemal complex in *C. elegans* germline

The synaptonemal complex is essential to organise homologous chromosomes during meiosis (Zickler and Kleckner, 1999), and is a key regulator of numerous processes in meiotic prophase I including crossover regulation and meiotic checkpoint signalling (Ur and Corbett, 2021). Investigating the organisation of individual components within the synaptonemal complex is integral to understanding its many functions in meiosis. Since the width of the central region of ~100 nm (Rog et al., 2017) cannot be resolved by diffraction-limited fluorescence microscopy, super-resolution microscopy techniques have emerged as an invaluable tool to study the substructure of the synaptonemal complex. Various super-resolution microscopy techniques including structured illumination microscopy (SIM), expansion microscopy (Chen et al., 2015), stimulated emission depletion (STED) microscopy (Klar et al., 2000), and single-molecule localisation microscopy (SMLM, Rust et al. 2006; Betzig et al. 2006) have been used to study the molecular architecture of the synaptonemal complex in different model organisms (Schücker et al., 2015; Prakash et al., 2015; Cahoon et al., 2017; Köhler et al., 2017, 2020; Yoon et al., 2018; Xu et al., 2019; Hesse et al., 2019; Hurlock et al., 2020; Zwettler et al., 2020; Capilla-Pérez et al., 2021).

In this chapter, I show how optimising the immunohistochemistry protocol by directly fixing the tissue to the coverslip enabled me to study the substructure of the synaptonemal complex in intact, extruded *C. elegans* germline tissue with SMLM and STED microscopy (Čavka et al., 2022). I further present how I used this approach to determine the localisation of newly identified components of the synaptonemal complex in *C. elegans*. Specifically, I participated in demonstrating that SYP-5/6 transverse the width of the synaptonemal complex (Hurlock et al., 2020), while Skp-1 related proteins localise to the central element of the synaptonemal complex in *C. elegans* (Blundon et al., 2023). In both cases, elucidating the localisation of the components within the complex provided invaluable insights into the function of

these novel components within the synaptonemal complex.

4.1. Optimising the sample preparation for super-resolution microscopy of the synaptonemal complex

The resolution of SMLM methods strongly depends on the distance of the imaging plane from the coverslip (Schermelleh et al., 2019) since light scattering, background, and spherical aberrations increase with this distance. Therefore, only the bottom-most *z*-section of meiotic nuclei that contain the synaptonemal complexes should be imaged by SMLM to minimise light scattering and optical aberrations that occur within the germline tissue. To further minimise the distance of the germline tissue to the coverslip, I chemically fixed the tissue to a poly-lysine coated coverslip. However, due to the stochastic nature of this mounting procedure (**Figure 3.1**), the sections are still found at varying distances from the coverslip since the gonad tissue might not always lay perfectly flat on the coverslip (Čavka et al., 2022).

To determine how the quality of the SMLM image depends on the attachment of the *C.elegans* germline tissue to the coverslip, I compared the FRC resolution (**Figure 4.1**) of SMLM images acquired at different piezo distance from the coverslip[1]. Since the width of the central region of the synaptonemal complex is around 100 nm, it is expected that the quality of the images will deteriorate with increasing distances from the coverslip such that details within the ultrastructure of the synaptonemal complex may be lost.

To demonstrate how the drop in the quality limits the achievable insights into the ultrastructure of the synaptonemal complex, **Figure 4.2** compares two 3D-SMLM images acquired at two extreme distances from the coverslip. To this end, I have used 3D-SMLM to localise two components whose location within the synaptonemal was previously determined. Specifically, I localised the C-terminus of SYP-5 using a hemagglutinin (HA) epitope tag (SYP-5::HA) and the chromosome axis component HTP-3. If the quality of the SMLM images is sufficient, both components should localise within two parallel bands separated by 84 nm (SYP-5::HA, Hurlock et al. 2020) and 110 nm (HTP-3, Köhler et al.

[1] Piezo distance from the coverslip represents the piezo stage position of the imaging plane relative to the piezo stage position when the objective was focused on the coverslip.

2017) respectively.

In SMLM images acquired close to the coverslip, the FRC resolution is estimated at 38 nm for the AlexaFluor 647 channel and at 34 nm for the CF680 channel. Indeed, the C-termini of SYP-5::HA (~84 nm apart, Hurlock et al. 2020 and section 4.2) can be resolved independently of their orientation towards the direction of imaging (frontal or lateral view, **Figure 4.2B i and ii**). However, this is not the case for synaptonemal complexes that lay further away from the coverslip. At approximately 5 µm above the coverslip, the estimated FRC resolutions drops to 47 nm (AlexaFluor 647) and 41 nm (CF680). At this resolution, the two localisation bands of SYP-5::HA and HTP-3 (~110 nm, Köhler et al. 2017) can no longer be reliably resolved in cross-sections of the synaptonemal complex in lateral view (**Figure 4.2B i and ii**). The results suggested that the substructure of the synaptonemal complex is resolved reliably only within 2 µm from the coverslip, highlighting the importance of the close attachment of the tissue to the coverslip (Čavka et al., 2022).

The protocol presented in this thesis (see subsection 3.4.4) and in Čavka et al. 2022 was optimised to achieve this close attachment of the *C. elegans* germline tissue to the coverslip to allow imaging of the synaptonemal complex ultrastructure with SMLM. Importantly, the tissue was immunostained before it was attached to the coverslip which significantly increased the labelling density. The labelling density is a crucial factor in limiting the resolution achievable by the SMLM technique (Xu et al., 2013). Indeed, the FRC resolution was only 40-50 nm in previous SMLM imaging of the synaptonemal complex in the *C. elegans* germline in Hurlock et al. 2020 when samples were immunostained after the attachment to the coverslip. By contrast, the protocol presented here secured the higher quality with an FRC resolution of 30-40 nm in the SMLM images.

Therefore, immobilising the tissue by covalent attachment to the coverslip after immunostaining offered several advantages. The stable attachment reduced the sample drift and allowed the use of larger volume of imaging buffer, which increased the time during which the sample could be imaged. Specifically, an alternative immobilisation method included imaging of the germline tissue trapped between two coverslips (Köhler et al., 2017, 2020). The down-side of this method compared to the one presented here is the severe reduction in the volume of the imaging buffer that surrounds the tissue (a

few µL, compared to 1 mL), leading to the faster acidification of the buffer that reduces the time during which sample can be imaged (Shi et al., 2010; Olivier et al., 2013).

Together, the protocol presented here allows for studying the 3D organisation of the synaptonemal complex in its native environment at the high resolution provided by SMLM imaging. However, long acquisition time, high laser powers used, and limited imaging depth inherent to the SMLM imaging restrict the number of obtainable images of the synaptonemal complex (Schermelleh et al., 2019). Due to faster image acquisition, easier sample handling, lower sensitivity to the sample thickness, and larger imaging depth (Schermelleh et al., 2019), STED microscopy could be a good alternative to gain insight into the substructure of the synaptonemal complex. I therefore decided to test the resolving power of TauSTED microscopy within the germline tissue of *C. elegans*.

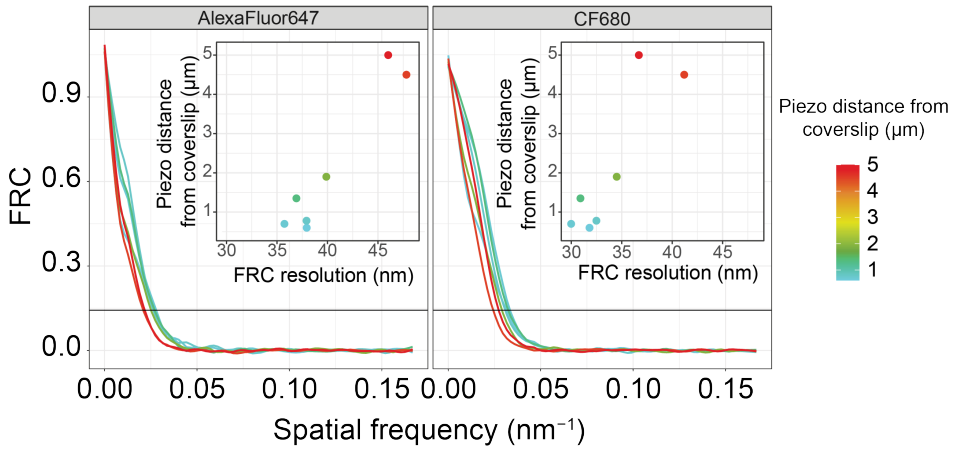


Figure 4.1. Dependence of the Fourier ring correlation resolution of single-molecule localisation microscopy images on the distance of the imaged *z*-plane from the plane of the coverslip

Colored lines show Fourier ring correlation (FRC) curves of images acquired at different distances (as depicted by the color bar) from the coverslip. The 1/7 threshold used to determine the FRC resolution is indicated by a black horizontal line. Insets show the dependence of the FRC resolution on the piezo distance from the coverslip. Piezo distance from the coverslip represents the piezo stage position of the imaging plane relative to the piezo stage position when the objective was focused on the coverslip. Taken from Čavka et al. 2022 and was originally made by me.

Similarly to the SMLM results, the two bands of HTP-3 and SYP-5::HA in frontal to slightly tilted views can be resolved by TauSTED microscopy. **Figure 4.3A** shows TauSTED images with the highest and lowest resolution that I was able to achieve. Within both images, two bands of both HTP-3 and

SYP-5::HA can be resolved (**Figure 4.3B**) demonstrating that the resolution I achieved must be below 84 nm in both images[2]. Furthermore, the C-termini of SYP-5::HA can be resolved in slightly tilted views of the synaptonemal complex when they are ~50 nm apart (**Figure 4.3C**, Čavka et al. 2022).

However, the resolving power of STED microscopy is generally lower than the resolution in SMLM images (Schermelleh et al., 2019). Since understanding the function of individual components can be limited by how precisely they can be localised within the complex, the higher resolving power of the SMLM method is oftentimes advantageous for investigating the structure-function relationship of the synaptonemal complex (Čavka et al., 2022).

4.2. SYP-5/6 transverse the width of the synaptonemal complex

In 2019, the Kim lab at Johns Hopkins University (Baltimore, MD 21218, United States), identified two new components, SYP-5 and SYP-6, of the synaptonemal complex in *C. elegans*. Their research identified these new components by mass spectrometry of proteins that were co-immunoprecipitated with GFP-tagged SYP-3, a component of the central region of the synaptonemal complex. The deletion of *syp-5/6* genes abolished the synaptonemal complex, demonstrating that SYP-5/6 are absolutely required for synapsis (Hurlock et al., 2020). The fact that SYP-5/6 are an essential part of the synaptonemal complex raised the question of where these proteins were localised within the complex. To address this question, I used 3D-SMLM to map the localisations of SYP-5/6 proteins within the synaptonemal complex in collaboration with the Kim and Ries research groups.

To precisely map the orientation of SYP-5/6 within the synaptonemal complex, I separately imaged both N- and C-terminus of SYP-5/6 each tagged with a hemagglutinin (HA) tag (Hurlock et al., 2020)). To map the orientation of the complex, I used immunofluorescent staining of the chromosome axis component HIM3 to identify frontal views of the synaptonemal complex. Indeed, two strands of HIM-3 could easily be distinguished in frontal views as expected (**Figure 4.4**) .

Averaging multiple stretches of the synaptonemal complex from several SMLM images revealed that

[2]The distance between the two localisation bands of SYP-5::HA, reported in Hurlock et al. 2020 and the following section 4.2

the HIM-3 axes are sparated by ~128 nm (**Figure 4.4 B**). Importantly, the positions of the N-terminal HA::SYP-5/6 and the C-terminal SYP-5/6::HA within the synaptonemal complex in late pachytene were clearly different. The N-termini of HA::SYP-5/6 were localised in the centre of the synaptonemal complex (**Figure 4.4**). On the other hand, two distinct stretches of the C-termini of both SYP::5-HA and SYP-6::HA were separated by 84 nm in frontal view (**Figure 4.4 B**). The C-termini of SYP-5 and SYP-6 are therefore placed adjacent to the HIM-3 axes (~21 nm). Additionally, the localisations of both ends of SYP-5/6 were confined to a narrow *z*-plane in cross-sectional views (**Figure 4.4 A**) with half widths at half maximum (HWHM) of 40 to 50 nm (Appendix F). The positioning of the two N-termini at the centre and the C-termini facing the axes in frontal views demonstrates that both SYP-5 and SYP-6 cross the width of the synaptonemal complex in a head-to-head manner (**Figure 4.4 C**, Hurlock et al. 2020). Additionally, the indistinguishable localisation of SYP-5 and SYP-6 proteins was consistent with their redundant roles within the assembly of the synaptonemal complex since the complex assembles in the absence of one of the two proteins (Hurlock et al., 2020).

4.3. SKR-1 and SKR-2 localise within the central region of the synaptonemal complex

In addition to SYP-5/6, the Kim and Gao labs also identified the Skp1-related proteins SKR1 and SKR2 (Nayak et al., 2002) in immunoprecipitates of synaptonemal complex components (Hurlock et al., 2020; Zhang et al., 2020). This interesting observation has led the Kim lab at Johns Hopkins University to investigate further the role of SKR-1 and SKR-2 during meiotic prophase I in *C. elegans*. Skp1-related proteins are a part of the SKP1-Cullin-F-box (SCF) ubiquitin E3 ligase. SCF ligases are involved in the polyubiquitination that leads to the degradation of specific protein targets. This target specificity of SCF ligases is provided by the F-box protein component of the complex, while Skp1 acts as an adaptor and binds different F-box proteins. Thus, Skp1 allows for the formation of different ligases with different target specificity (Cardozo and Pagano, 2004). Recently, HORMA domain proteins in the chromosome axes have been identified as targets of the SCF ubiquitin E3 ligase.

Specifically, it was shown that Skp1 plays a role in the eviction of HORMA domain proteins from the

synaptonemal complex upon entry into pachytene in mice spermatocytes. This study also showed that the Skp1 protein localises to the chromosome axes in mice (Guan et al., 2020). However, data from the Kim group suggested that Skp1-related proteins may be a structural component of the synaptonemal complex central region in *C. elegans* since genetic experiments revealed that the synaptonemal complex failed to assemble in the absence of the two paralogous Skp1 proteins SKR-1/2 (Blundon et al., 2023).

Experiments from the Kim lab also revealed that all previously identified components of the central region of the synaptonemal complex were co-immunoprecipitated with Flag tagged SKR-2 protein (SKR -2::3Flag, Blundon et al. 2023). Furthermore, cytological experiments showed that SKR-1 and SKR-2 proteins co- localise at the synaptonemal complex during meiotic prophase I. However, SKR-1/2 are absent from meiotic chromosome axes in *syp-2* mutants lacking the synaptonemal complex (Blundon et al., 2023) thus resembling other components of the central region (MacQueen et al., 2002; Couteau et al., 2004; Smolikov et al., 2007, 2009; Hurlock et al., 2020; Zhang et al., 2020). These findings suggested that Skp1 proteins may be a part of the synaptonemal complex central region in *C. elegans* and not, as previously observed in mice spermatocytes, of the chromosome axes (Blundon et al., 2023; Guan et al., 2020).

To further corroborate the claim that SKR-1 and SKR-2 are indeed a part of the central region of the synaptonemal complex in *C. elegans*, I performed 3D-SMLM to localise a hemagglutinin (HA) tag fused to the N-terminus of SKR-1 (HA::SKR-1) and a Flag tag fused to the C-terminus of SKR-2 (SKR -2::3Flag) in collaboration with the Kim and Ries groups. Indeed, SMLM images of late pachytene nuclei show that HA::SKR-1 and SKR-2::3Flag localise in the central region of the synaptonemal complex between the two chromosome axes in frontal views of the synaptonemal complex. Similarly, both Skp1 related proteins are confined within a narrow *z* plane in the cross-sectional views (**Figure 4.5** and **4.6**, Blundon et al. 2023).

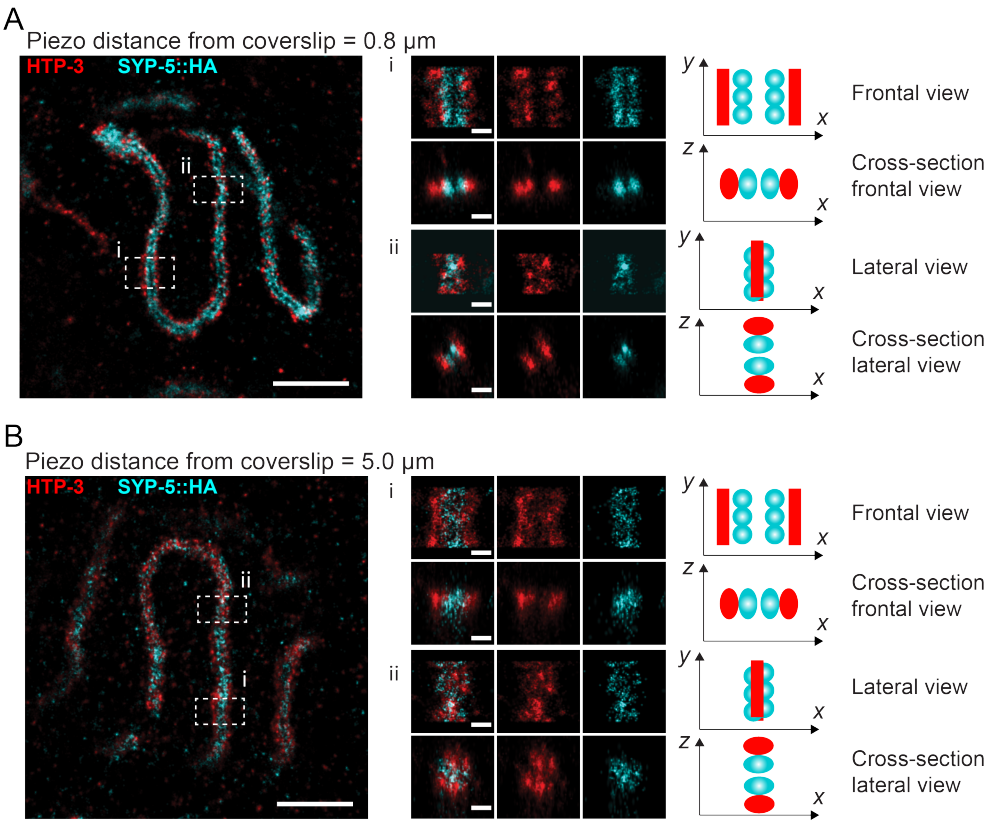


Figure 4.2. Single-molecule localisation microscopy of HTP-3 and the C-termini of the SYP-5
(A, B) Left: Single-molecule localisation microscopy (SMLM) images showing pachytene nuclei stained for HTP -3 and the C-terminus of SYP-5 (SYP-5::HA, scale bar: 1 µm). Centre: Zoomed-in images of regions of interest that are indicated in A and B (i, ii). The corresponding cross-sectional views are displayed below each image. Scale bar: 100 nm. The stretches of the synaptonemal complex within zoomed-in images are rotated to orient the chromosome axes parallel to the *y*-axis. Right: Graphical representation of the orientation of the synaptonemal complex in the zoomed-in regions. For each image, the piezo distance from the coverslip represents the piezo stage position of the imaging plane relative to the piezo stage position when the objective was focused on the coverslip. This figure was published in Čavka et al. 2022.

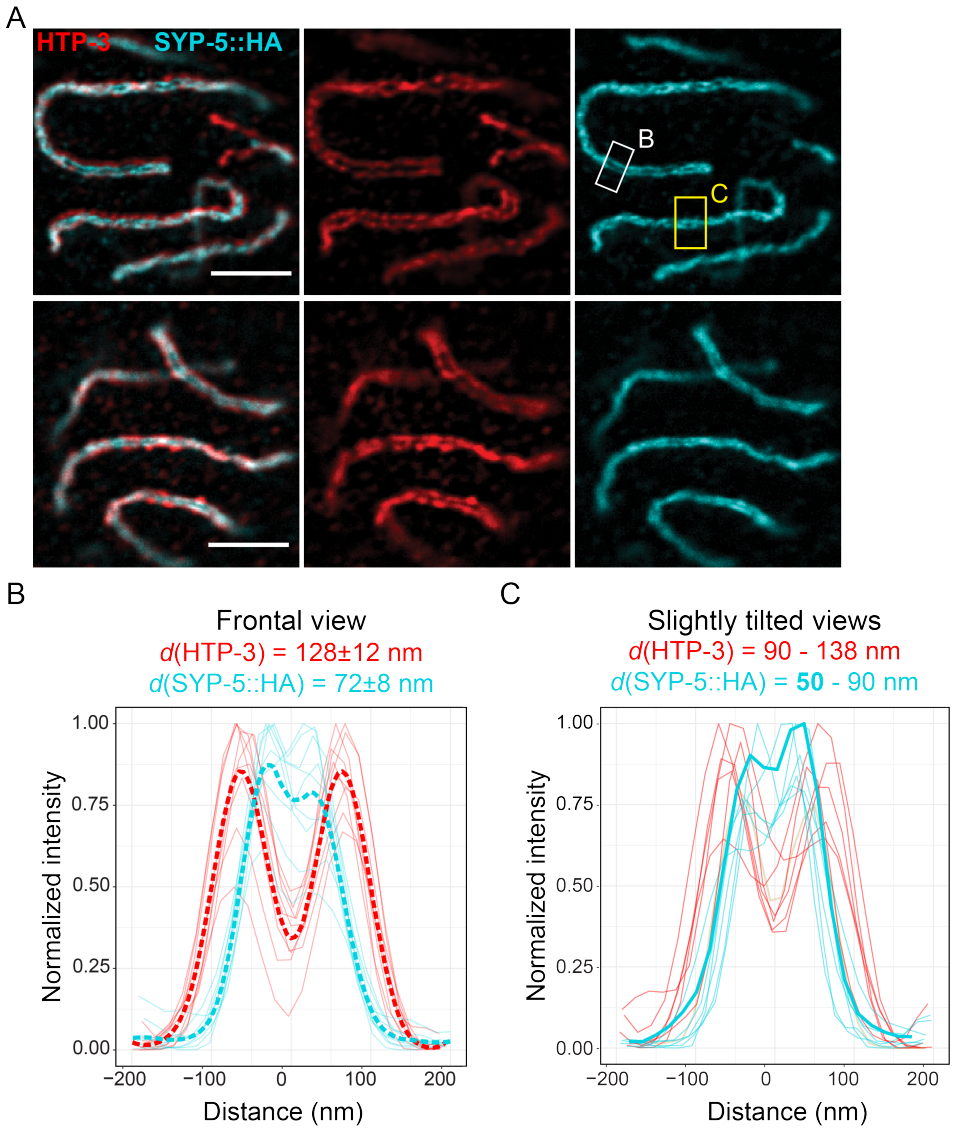


Figure 4.3. Fluorescence Lifetime Imaging enhanced TauSTED microscopy resolves two localisation bands for both, HTP-3 and the C-terminus of SYP-5

(A) Two representative TauSTED images show pachytene nuclei stained for HTP-3 (red) and the C-terminus of SYP-5 (SYP-5::HA, cyan) with higher (top) and lower (bottom) structural definition (scale bar: 1 µm). The rectangles mark regions with resolved C-termini of SYP-5 in frontal (white) and a slightly tilted view (yellow) of the synaptonemal complex. **(B, C)** Line profiles of regions of interest that contain the synaptonemal complex in frontal (B) or slightly tilted (C) views, are shown as full lines with intensity normalised to the maximum value. Dashed lines in B show the averaged data for each protein. The thick cyan line in C corresponds to the line profile with the shortest resolved distance between the C-termini of SYP-5. The distances between the antibodies targeting specific proteins (n = 9 (B), n = 7 (C)) were determined by fitting the line profiles with bi-modal gaussian distributions (section 3.6). Mean distance ± standard deviation (B) and the range with minimum value highlighted in bold (C) are indicated on top of each graph, respectively. Taken from Čavka et al. 2022.

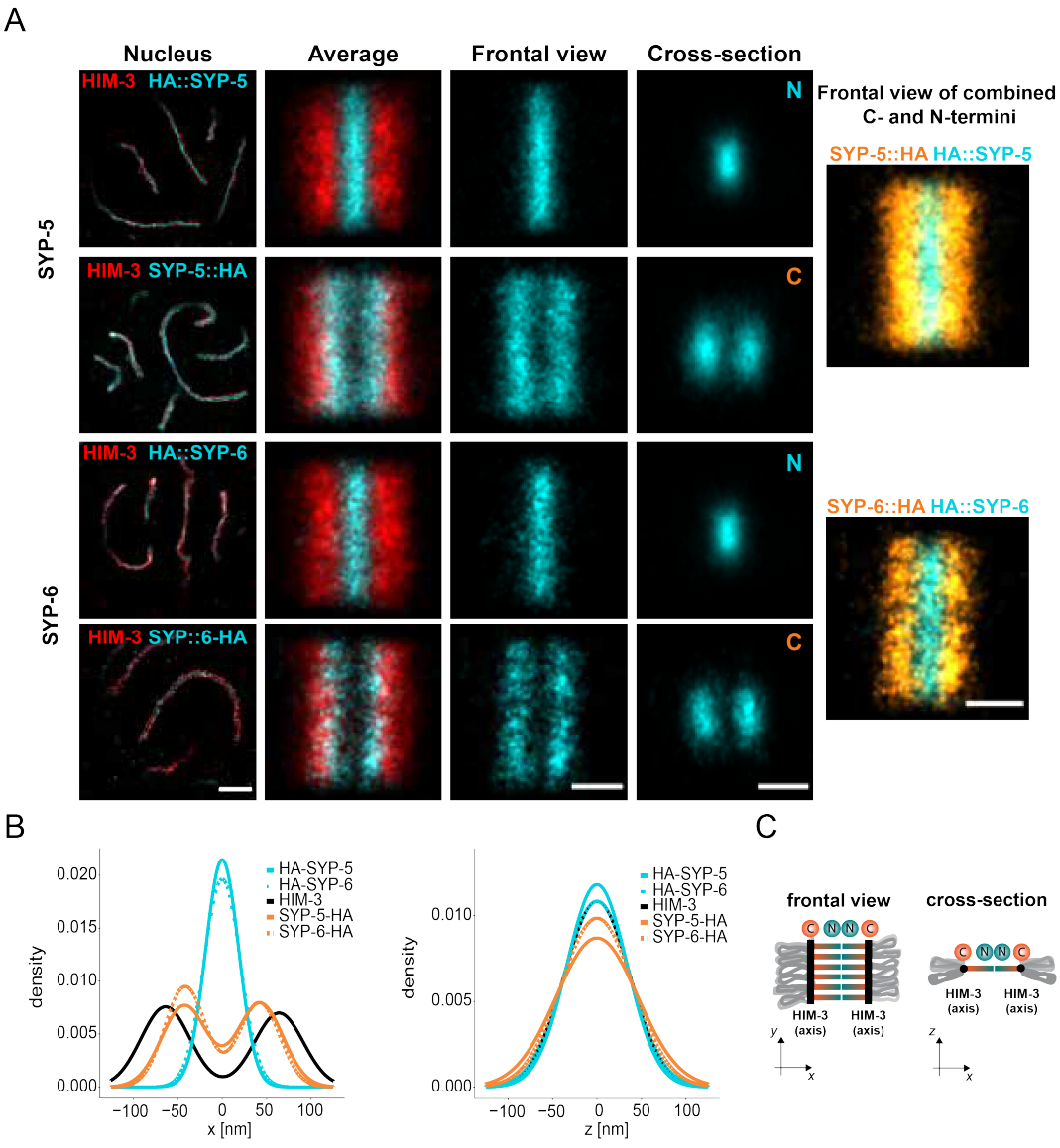


Figure 4.4. Aligned stretches of the synaptonemal complex in late pachytene

(A) Left: Single molecule localisation microscopy (SMLM) images showing late pachytene nuclei stained for HIM-3 and hemagglutinin (HA) tag fused to N-and C-termini of SYP-5 and SYP-6 (scale bars: 1 µm). Late pachytene nuclei were identified by the presence of designated crossovers marked by bright GFP::COSA-1 foci, Yokoo et al. 2012. Centre: The corresponding images of aligned stretches are shown in frontal (*xy*) and cross-sectional (*xz*) views (scale bars: 100 nm). Right: Combined frontal view of C-and N-termini of SYP-5/6 (scale bars: 100 nm). **(B)** The graph shows the resulting distributions of localisations for all mapped domains in *x* (left) and *z* (right) during the late pachytene. **(C)** A schematic highlighting the head-to-head orientation of SYP -5/6 within the synaptonemal complex. Modified from Hurlock et al. 2020 and was originally made by me.

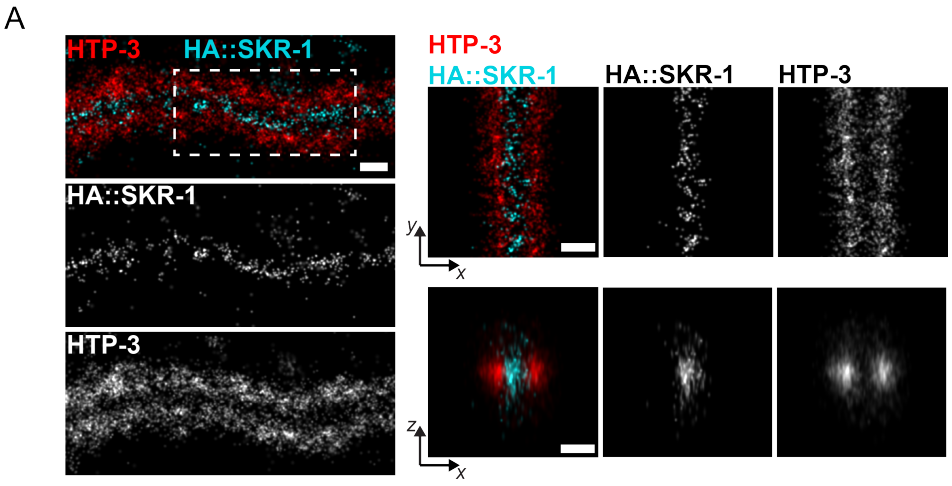


Figure 4.5. SKR-1 protein localises to the central region of the synaptonemal complex
Left: 3D-single molecule localisation microscopy (SMLM) images showing a stretch of a late pachytene synaptonemal complex stained for HTP-3 and hemagglutinin (HA) tag fused to the N-terminus of SKR-1 (Fourier ring correlation resolution = 50 nm). Right: SMLM localisations within the boxed region were straightened and rendered to create frontal (*xy*) and cross-sectional (*xz*) views of the synaptonemal complex. Scale bars: 100 nm. Adapted from Blundon et al. 2023. The original image was created by me.

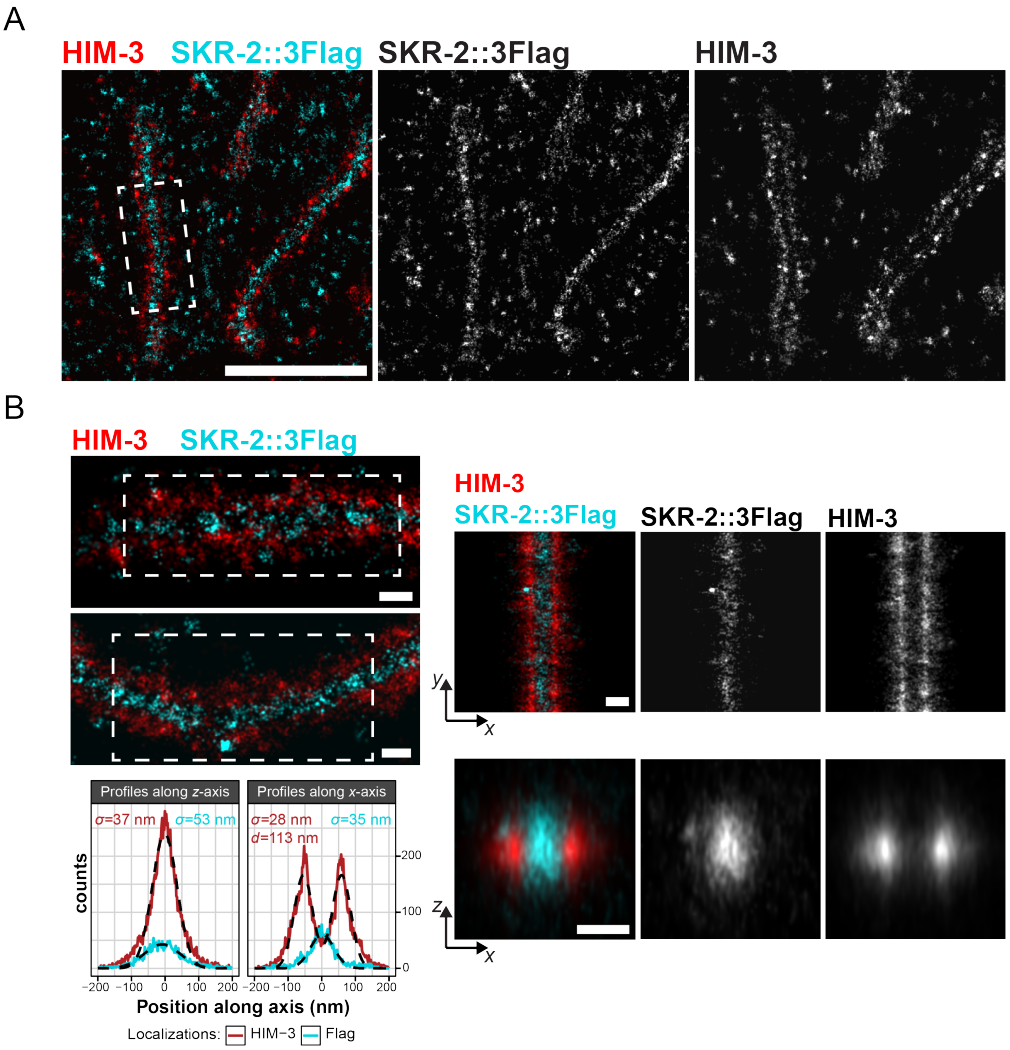


Figure 4.6. SKR-2 protein localises to the central region of the synaptonemal complex

(A) 3D-single molecule localisation microscopy (SMLM) images (Fourier ring correlation (FRC) resolution = 35 nm) showing a late pachytene nucleus stained for HIM-3 and a Flag epitope tag fused to the C-terminus of SKR-2 (scale bar: 1 µm). **(B)** Zoomed-in view of two stretches showing HIM-3 and SKR-2::3Flag in late pachytene showing the localisation of SKR-2 within the central region of the synaptonemal complex (top-left, FRC resolution = 40 nm, scale bars: 100 nm). SMLM localisations within the three boxed regions in A and B were straightened, aligned, and rendered to create averaged frontal (*xy*) and cross-sectional (*xz*) views (right, scale bars: 100 nm). Histogram counts (2 nm wide bins, bottom left) of straightened and aligned SMLM localisations along *x* and *z* axis, respectively, were fitted with gaussian distributions (black dashed lines). The respective standard deviations (σ), and peak-to-peak distance (d) are indicated in the plot. Adapted from Blundon et al. 2023. Original image was created by me.

4.4. Discussion

For this project, I specifically tailored an immunohistochemistry protocol to image the synaptonemal complex within intact, whole mount *C. elegans* gonad tissue (Hurlock et al., 2020; Čavka et al., 2022; Blundon et al., 2023) on custom built 3D-SMLM microscopes (Deschamps et al., 2016; Deschamps and Ries, 2020; Deschamps et al., 2023; Mund et al., 2018, 2023; Schröder et al., 2020; Diekmann et al., 2020). This process enhanced the resolution that 3D-SMLM can achieve and allowed me to map the localisation of novel components within the synaptonemal complex. Obtaining a precise localisation of these components is essential to understand their function within the synaptonemal complex.

Separate imaging of the N- and C-termini of SYP-5/6 revealed that the N-termini of SYP-5/6 are constricted at the centre of the synaptonemal complex while the C-termini are localised close to the chromosome axes. This finding manifested their role as transverse filament since they follow the well-known head-to-head orientation (**Figure 4.7**) that was previously observed for SYP-1 in *C. elegans* (Schild-Prüfert et al., 2011) and transverse filaments from other species (Sym and Roeder, 1995; Tung and Roeder, 1998; Liu et al., 1996; Schmekel et al., 1996; Anderson et al., 2005).

Data from mice spermatocytes suggested that Skp1-related proteins co-localise with the chromosome axis. However, my 3D-SMLM data revealed that SKR-2::3Flag localises in the centre of the synaptonemal complex similar to the N-termini of SYP-5/6. This localisation within the central region of the synaptonemal complex is also consistent with genetic data from the Kim lab (Blundon et al., 2023). However, the localisations of SKR-2::3Flag have a wider profile in both *x* and *z* axis than the N-termini of the transverse filament proteins I measured. Specifically, the standard deviations (σ) of a gaussian distribution fitted to the SKR-2::3Flag profiles (~35 nm along *x* and ~53 nm along *z* axis, **Figure 4.6** and Blundon et al. 2023) are higher than the corresponding standard deviations of localisation profiles of HA::SYP-5/6 (~21 nm and ~37 nm, Hurlock et al. 2020). This finding indicates that, contrary to the N-termini of SYP-5/6, the SKR-1/2 proteins are not constricted at the very centre of the synaptonemal complex, but are more likely distributed throughout the central region of the synaptonemal complex. The significance of the wider localisation profile of the SKR-2::3Flag is additionally supported by the

use of the shorter F(ab')$_2$ fragments compared to the full-length secondary antibodies used to localise the N-termini of SYP-5/6.

Precisely mapping the localisation of SKR-1/2 within the synaptonemal complex sheds light on how these proteins may function within the complex. A biochemical and genetic characterisation of SKR-1/2 showed that whilst their dimerisation is absolutely essential for the assembly of the synaptonemal complex, it prevents the assembly SCF ubiquitin ligase complex. Hence, the dimerisation of SKR-1/2 represents a molecular basis of their dual function as components of SCF ubiquitin ligase complex (monomers) and the synaptonemal complex (dimers, Blundon et al. 2023). Based on this observation, it is tempting to speculate that SKR-1/2 may serve as a *zipper* of the synaptonemal complex, holding the N-termini of the transverse filament joint at the mid-line of the synaptonemal complex. However, this function would require SKR-1/2 to be perfectly co-localised with the N-termini of the transverse filaments. By contrast, their wide distribution within the central region, as shown by SMLM imaging, contradicted this potential molecular function in *zipping* of the two sides of the synaptonemal complex. Indeed, further investigation of the SKR-1/2 function within the synaptonemal complex confirmed this alternative hypothesis, and concluded that SKR-1/2 proteins rather have a function in the elongation of the complex, potentially stabilising its assembly between homologous chromosomes during pachytene (**Figure 4.7**, Blundon et al. 2023).

While 3D-SMLM can reveal the ultrastructure of the synaptonemal complex and provide new insights into the function of components within the synaptonemal complex, it is important to consider that the fixed structure might not fully correspond to the native structure of the complex *in vivo*. To minimise artefacts, some precautions are taken during the preparation steps, such as the selection of intact, undamaged gonads and preventing the squishing of the tissue by avoiding desiccation of the sample during the post-fixation steps when tissue is trapped between two coverslips. Additionally, imaging of fixed tissue is blind to the dynamics of the native structure of the synaptonemal complex during meiosis. To a certain extent, this pitfall could be sidestepped by extrapolating the dynamics and the variability of the synaptonemal complex organisation from numerous *snapshots*. However, the success of this approach depends on the frequency of the change in the organisation and is hence limited by the

number of images that can be acquired to capture all the different states. Currently, the main hurdle to obtaining a higher number of SMLM images is the low sample density of the germline tissue on the coverslip. This low sample density prohibits the use of automated image acquisition pipelines that were successfully applied to investigate other biological questions (Thevathasan et al., 2019; Sabinina et al., 2021; Mund et al., 2018, 2023; Cieslinski et al., 2023; Sieben et al., 2018).

However, the unique organisation of the *C. elegans* gonad allows to circumvent the limited sampling to a certain degree since space corresponds to time in meiotic prophase, and we can directly target different stages. Previously, imaging the ultrastructure at different positions within the germline allowed for identifying the reorganisation within the complex (Köhler et al., 2020). However, faster and more dynamic processes can not be captured.

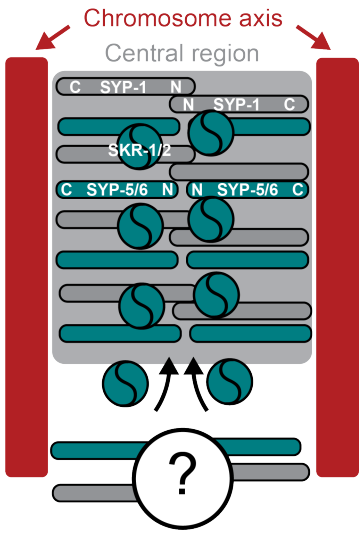


Figure 4.7. Localisation of the SYP-5/6 and SKR-1/2 proteins within the synaptonemal complex of *Caenorhabditis elegans*

The synaptonemal complex components SYP-5/6 and SKR-1/2 localise to the central region during the *C. elegans* meiosis. 3D-single-molecule localisation microscopy (SMLM) imaging shows that all four proteins localise between the two chromosome axes (red bars). However, the localisation patterns differ between proteins, pointing to their differing functions within the synaptonemal complex. The head-to-head orientation of SYP-5/6 proteins, with their N-termini at the centre of the complex and C-termini close to the chromosome axis, points to their role as transverse filaments of the synaptonemal complex (Hurlock et al., 2020). On the other hand, the SKR-1/2 proteins localise throughout the central region, contradicting a function in *zipping* of the two halves of the synaptonemal complex at the midline. Further investigation into the role of the SKR-1/2 proteins within the synaptonemal complex hints to their putative role in the elongation of the complex and the stabilisation of its assembly along homologous chromosomes (Blundon et al., 2023).

5. Timing of crossover designation in *Caenorhabditis elegans* meiosis

In this chapter, I investigated the timing of crossover designation and the putative role of the synaptonemal complex in this process on two levels. Firstly, I observed the dynamics of the crossover designation *in vivo* by diffraction-limited imaging of the *C. elegans* germline. Specifically, I explored the dynamics of foci formed by the crossover marker COSA-1 (Yokoo et al., 2012) tagged with HaloTag. These data revealed two populations of foci with differing dynamics. Secondly, I explored the disputed question of the active role of the synaptonemal complex in crossover designation. To this end, I investigated the organization of recombination intermediates and the surrounding synaptonemal complex at different stages of the homologous recombination repair by single-molecule localisation microscopy (SMLM). I identified changes in the organization of a pro-crossover factor, the MutSγ complex component MSH-5, and the chromosome axis that correlate with the observed changes in the number and dynamics of individual HaloTag::COSA-1 foci.

5.1. Image analysis pipeline faithfully captures the number and intensity distribution of COSA-1 protein along the germline

A major advantage of studying meiosis in the model organism *C. elegans* is the spatio-temporal organization of meiotic nuclei within the germline tissue (Lui and Colaiácovo, 2013). As meiotic nuclei progress through meiosis, they physically move within the tissue in a well-defined direction. For this reason, different stages of meiosis can be easily identified within the gonad. For example, the intensity of foci formed by a fluorescently labelled crossover marker, COSA-1 (Yokoo et al., 2012), sharply increases at the transition from mid- to late pachytene stage (**Figure 5.1A**). At this transition, the number of foci is reduced to exactly six foci that are significantly brighter compared to the foci before this transition. These bright foci correspond to the designated crossover sites, while dim foci at earlier stages mark earlier recombination intermediates (Yokoo et al., 2012; Woglar and Villeneuve, 2018). These previously well-established trends regarding the change in the number and intensity of fluorescently labelled COSA-1 protein are recapitulated for COSA-1 tagged with HaloTag7 used in this study (HaloTag::COSA-1, **Figure 5.1**). The specifically tailored image analysis pipeline (see section 3.8.1) successfully describes the relationship of HaloTag::COSA-1 foci number (**Figure 5.1B**) and intensity (**Figure 5.1C**) within a given nucleus and the position of that nucleus within the germline tissue. Interestingly, two nuclei that undergo apoptosis (zoomed-in views in **Figure G.1A**) are readily recognized as outliers in both foci number and mean foci intensity when compared to other nuclei with similar positioning within the gonad (**Figure 5.1B** and C denoted by ”*”).

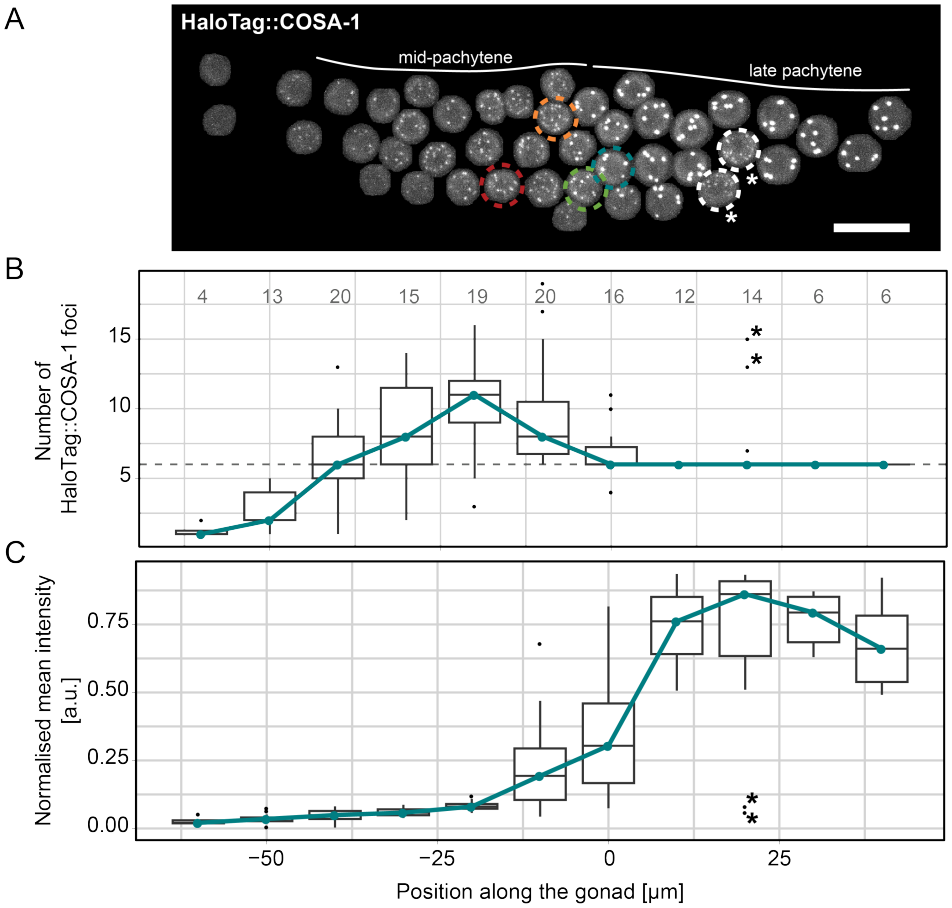


Figure 5.1. Distribution of HaloTag::COSA-1 foci along the *C. elegans* germline

(A) Maximum intensity projection image of a *C. elegans* germline with HaloTag::COSA-1 signal in grey (scale bar: 10 µm). The number of HaloTag::COSA-1 foci **(B)** and mean intensity **(C)** were assessed within each meiotic nucleus from three different germlines. The germlines are centred around the transition from mid- to late pachytene, recognized by an increase in foci intensity. Coloured dashed circles mark four different nuclei whose synaptonemal complexes were traced and their colouring is consistent throughout the sections 5.1-5.3. White dashed circles and "*" mark outliers in the late pachytene region. The grey numbers above the boxplots in B correspond to the number of meiotic nuclei within each 10 µm wide bin and are common for the plots in B and C. The boxplots in B and C show data from the first frame of the timelapse movies.

5.2. Optimised immobilization protocol allows for long-term imaging of the meiosis

To investigate the dynamics of recombination foci within individual nuclei, several steps were taken to mitigate potential imaging artefacts.

One of the main hurdles in the immobilization of *C. elegans* animals for imaging is the meiotic halt that occurs when animals are paralysed by an anaesthetic. Similarly, meiosis may stop due to other stressors as observed in previous (Rog and Dernburg, 2015), and initial attempts at *in vivo* imaging of *C. elegans* germlines by me and other members of the group. To this end, I, E. Berna Durmus, and Lauren (Mickey) Sloat combined efforts to integrate and optimize the application of previously suggested *in vivo* imaging protocols. To reduce the movement of the animals during the acquisition, we placed worms in channels of an agarose gel created by using a vinyl record as a template (Gomez and Schvarzstein, 2018). Additionally, we reduced light-induced stressors by introducing two mutations that reduce the locomotion in response to blue and UV light in our imaging strain (Bhatla and Horvitz, 2015). Furthermore, a serotonin solution was added to reduce stress responses further and prevent the occurrence of a meiotic halt during the acquisition (Rog and Dernburg, 2015).

To assess if meiosis continues during the timelapse movie, I confirmed the presence of chromosomal movement and nuclear rotations characteristic of meiotic progression. An example of this assessment is displayed in **Figure 5.2**.

Importantly, when HaloTag is conjugated to a specifically modified far-red fluorophore (Deo et al., 2021), dim foci of the mid-pachytene stage can be robustly imaged for several hours depending on the frequency at which time frames are acquired (data not shown). However, for any long-term imaging, the question of a potential loss of dim signal due to photobleaching must be assessed. Specifically, dimmer HaloTag::COSA-1 foci in mid-pachytene (**Figure 5.4B**) could be disproportionately lost compared to brighter foci. Thus, bleaching could greatly influence the conclusions about the dynamics of such foci.

Indeed, the comparison of empirical cumulative distributions (**Figure 5.3A**) demonstrates that later frames tend to have a smaller number of dim foci. To assess changes in the distribution of the foci

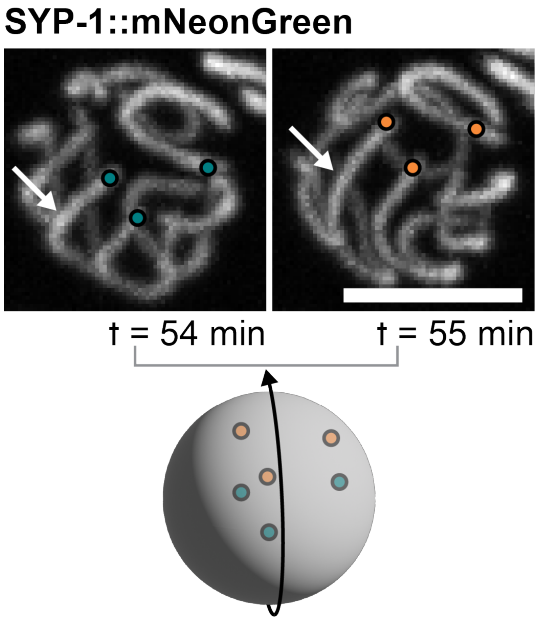


Figure 5.2. Progression of meiosis is confirmed by the presence of chromosome movement and nuclear rotation

Confocal images of meiotic nuclei at different time points during the timelapse movie with synaptonemal complex central region component SYP-1 C-terminally tagged with mNeonGreen are shown in grey. To confirm that meiosis has not stopped during the movie, nucleus rotation and synaptonemal complex movement are shown. White arrows indicate changes in the shape of an individual synaptonemal complex. Dark cyan and orange circles mark three positions within the nucleus at different time points. The graphics at the bottom illustrate the direction of the nuclear rotation between the two frames. Scale bar: 3 µm.

intensity, I performed a Kolmogorov-Smirnov goodness-of-fit test (Kolmogorov, 1933; Smirnov, 1939) between cumulative distributions of *A-fit* (spotMAX parameter used as a proxy for foci intensity) within the first and all subsequent frames of the timelapse movies (**Figure 5.3B**). The drop in the *p*-values after 40*th* time frame indicated that the distribution of foci intensity is significantly changed compared to the initial frame after this time. Thus, I excluded all subsequent frames (greater than 40) from further analysis unless indicated otherwise.

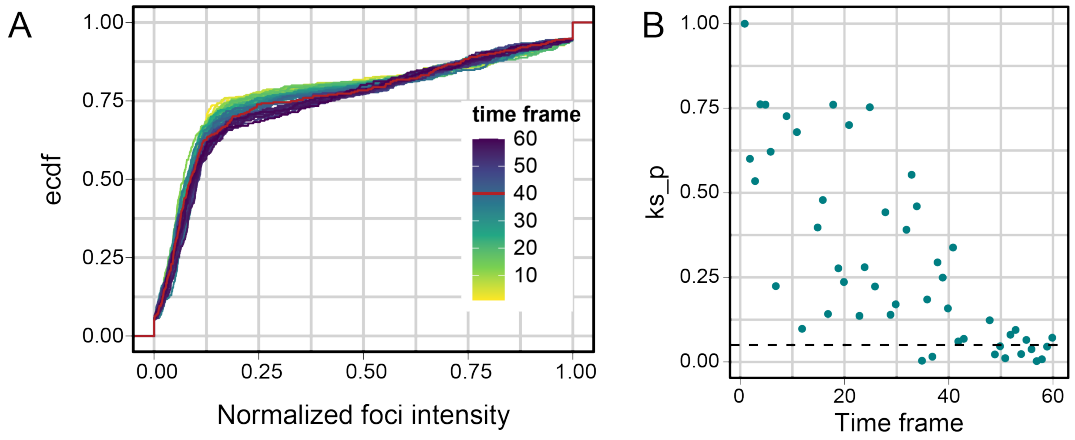


Figure 5.3. Photobleaching assessment

(A) Empirical cumulative distribution functions (ecdf) of normalized HaloTag::COSA-1 foci in individual frames of a timelapse movie of a *C. elegans* germline. The 40*th* time frame is highlighted in red. **(B)** Kolmogorov-Smirnov goodness-of-fit (Kolmogorov, 1933; Smirnov, 1939) test (R, version 4.2.2) between empirical cumulative distributions of *A-fit* (spotMAX parameter describing the peak of the 3D gaussian fitted to each focus) within each frame compared to the distribution of the same parameter in the first time frame. The ”p_KS” denotes the *p*-value, whilst the dashed line indicates a 0.05 significance threshold. To assure that any observed loss is not due to out-of-frame movement of some nuclei, only foci from nuclei that were present in more than 75% of the time frames were considered in A and B.

5.3. *In vivo* imaging of *C. elegans* germlines discovers intricate dynamics of HaloTag::COSA-1 foci

As expected, HaloTag::COSA-1 accumulates in six bright foci during late pachytene (Yokoo et al., 2012) that appear persistently attached to a specific region of each of the 6 synaptonemal complexes (**Figure 5.4 B**). However, foci of differing dynamics can be observed in mid-pachytene (**Figure 5.4 A**). Some foci are persistently associated with a single region of the synaptonemal complex while foci in other regions exhibit a *blinking* behaviour (**Figure 5.4 A** green arrows). These foci are absent in some frames of the timelapse but are detected in previous and subsequent frames.

Since some foci appear more persistent than others, I hypothesised that the persistent foci correspond to the designated sites and will eventually accumulate more COSA-1 molecules leading to the increase in foci brightness. To this end, I next investigated how the persistence of foci relates to their intensity, as well as which of the two types of foci is the last one to retain and accumulate COSA-1 protein.

To quantitatively describe the persistence of individual HaloTag::COSA-1 foci, individual foci must

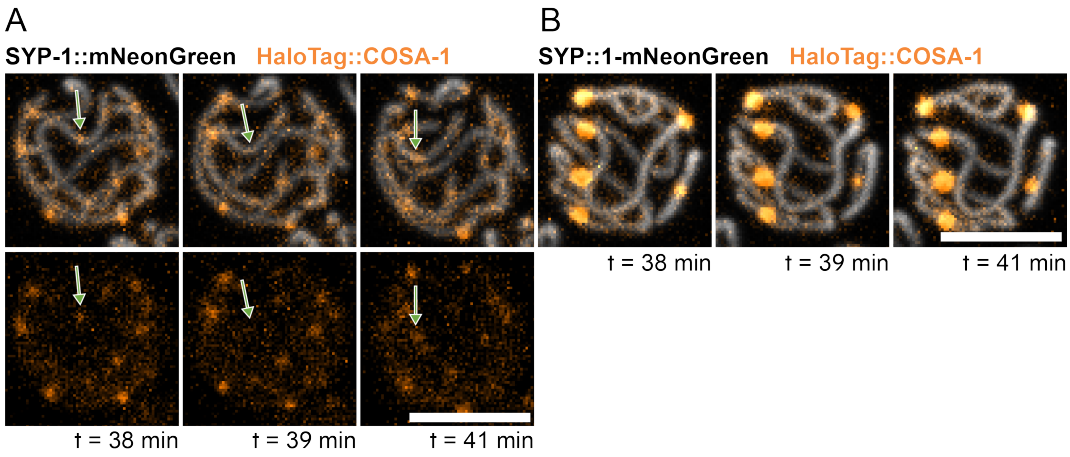


Figure 5.4. HaloTag::COSA-1 foci intensity at different timing during pachytene
Maximum intensity projection images of mid-pachytene **(A)** and late **(B)** nuclei with synaptonemal complexes in gray (SYP-1::mNeonGreen) and pro-crossover marker in orange (HaloTag::COSA-1). Arrows in B point to a HaloTag::COSA-1 focus that disappears and re-appears during the 3-minute interval shown here. Scale bars: 3 µm.

be identified across different time points. Since tracking individual foci over time is not trivial due to nuclear rotations, chromosomal movement (e.g. **Figure 5.2**), and the *blinking* behaviour of the foci (e.g. **Figure 5.4A**), I manually traced synaptonemal complexes marked by SYP-1::mNeonGreen. This tracing allowed me to associate each HaloTag::COSA-1 focus that was identified by spotMAX (see section 3.8.1) to its closest region of the synaptonemal complex. Thus, I was able to effectively follow individual HaloTag::COSA-1 foci for the duration of the timelapse movie.

Since manual tracing of the synaptonemal complexes in a large number of time frames is cumbersome, I could only analyse a limited number of nuclei. For this reason, I selected four nuclei at slightly different stages of meiotic progression that correspond to the transition between mid- to late pachytene (**Figure 5.1A** and **Figure G.1B**). I focused on nuclei close to the transition from mid- to late pachytene because I hypothesized that the dynamics that are related to crossover designation would be observed there since six bright COSA-1 foci in late pachytene that are known to correspond to the designated crossover sites (Yokoo et al., 2012) while earlier dim foci mark recombination intermediates (Woglar and Villeneuve, 2018). A closer look at the HaloTag::COSA-1 signal within the four selected nuclei revealed that a larger variation in number and a lower mean intensity of HaloTag::COSA-1 foci are

characteristic of nuclei that are in earlier stages of mid-pachytene and further away from late pachytene (**Figure 5.5**). On the other hand, the late pachytene nucleus (**Figure 5.5**, nucleus ”4”) has no variation in foci number and consistently has more than 2-fold higher mean intensity compared to the mid-pachytene nuclei (**Figure 5.5B**).

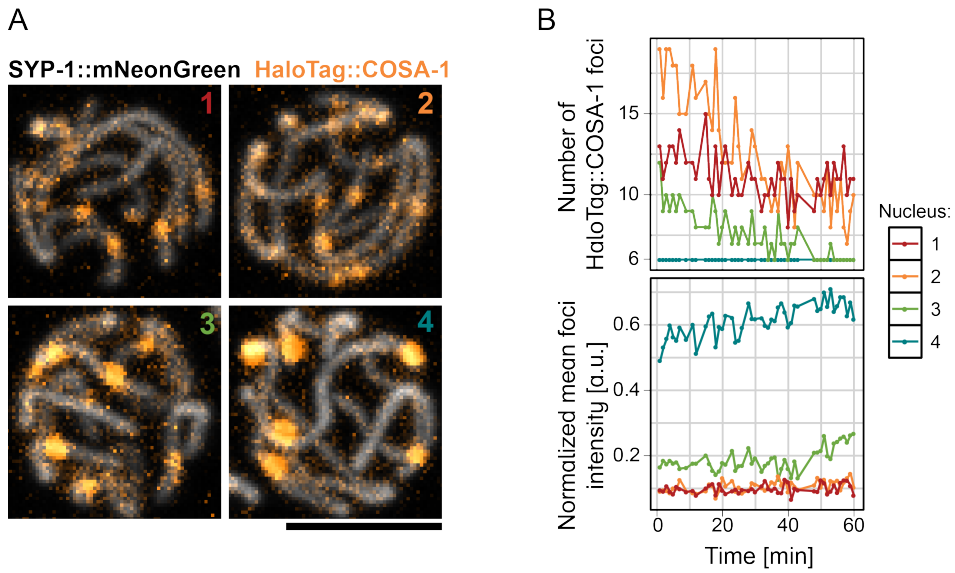


Figure 5.5. Nuclei whose synaptonemal complexes have been manually traced
(A) Maximum intensity projection images of four meiotic nuclei whose synaptonemal complexes have been traced manually to describe the change in the distribution of the pro-crossover marker COSA-1 (N-terminally tagged with HaloTag protein, orange) along the signal of the synaptonemal complex component SYP-1 (grey) tagged with mNeonGreen (scale bar: 3 µm). The number in the top-right corner of each panel and its colouring associates each nucleus with its corresponding number (top) and normalized mean intensity (bottom) of HaloTag::COSA-1 foci over time **(B)**. The numbering of the nuclei corresponds to their positioning along the germline tissue, with nucleus ”1” being the least and nucleus ”4” being the most advanced in meiosis.

Interestingly, the number of HaloTag::COSA-1 foci is reduced from twelve to six during the acquired timelapse in one of the traced nuclei (nucleus ”3”). The reduction in the number is followed by a slight increase in the mean focus intensity (**Figure 5.5B**). This was an interesting observation since in *C. elegans* the designation was related to the increase in the brightness. However, the mean intensity is the measure of the collective intensity within the nucleus. As such, the mean intensity increase can result from the disappearance of the dimmer foci and/or an increase in the brightness of individual foci. This further highlights that to relate the designation and accumulation, it is necessary to investigate the intensity of individual foci over time.

Unfortunately, this drop to 6 foci and the subsequent increase in brightness occurs after the 40*th* frame. Conservatively, I removed these frames from my analysis because the observed trend could also be a result of the dimmer foci being lost due to photobleaching. However, the fact that for several nuclei in the same timelapse (including traced nucleus ”1”, **Figure 5.5**), the number of HaloTag::COSA-1 foci fluctuates around the same number indicate that the trends observed for the nucleus ”3” are not the result of photobleaching in this experiment. Furthermore, dimmer foci than the ones within nucleus ”3” can consistently be identified and tracked in nuclei ”1” and ”2” at the same time when nucleus ”3” transits to a state with only six foci. Together, these data indicate that nucleus ”3” may indeed transition from mid-pachytene with more than 6 dim foci to a late-pachytene-like state with 6 bright(er) foci.

Importantly, since the intensity of the foci within the nucleus ”3” never reaches the levels of the foci within its neighbouring late-pachytene nucleus with six bright foci (nucleus ”4”, **Figure 5.5B**), this finding indicates that the accumulation of COSA-1 protein at designated crossover sites happens after the actual designation. Nevertheless, it will be important to confirm this trend by investigating other nuclei that transition from mid- to late pachytene. However, detecting the full transition from mid- to late pachytene is not trivial since only a limited number of nuclei could potentially undergo this transition within a one-hour window. There are several limitations that contribute to the low frequency at which this event can be observed: The transition from mid- to late pachytene happens seemingly instantaneously from one row to the next. This progression from one row to the next takes about 2 hours since there are 18-20 rows of pachytene nuclei in total and the entire pachytene stage is estimated to last 36 hours (Jaramillo-Lambert et al., 2007). However, only half of the tissue that is closer to the coverslip can be imaged due to increased light scattering and reduced signal-to-noise ratio associated with the imaging of the structures that are located deeper into the tissue. For this reason, usually three nuclei per row can be observed. Considering the time required for the progression from one row to the next, it is expected that only one of the three potential nuclei in the last mid-pachytene row will undergo the transition within a one-hour imaging interval. Thus, more data must be acquired and analysed to assess the transition from mid- to late pachytene *in vivo*.

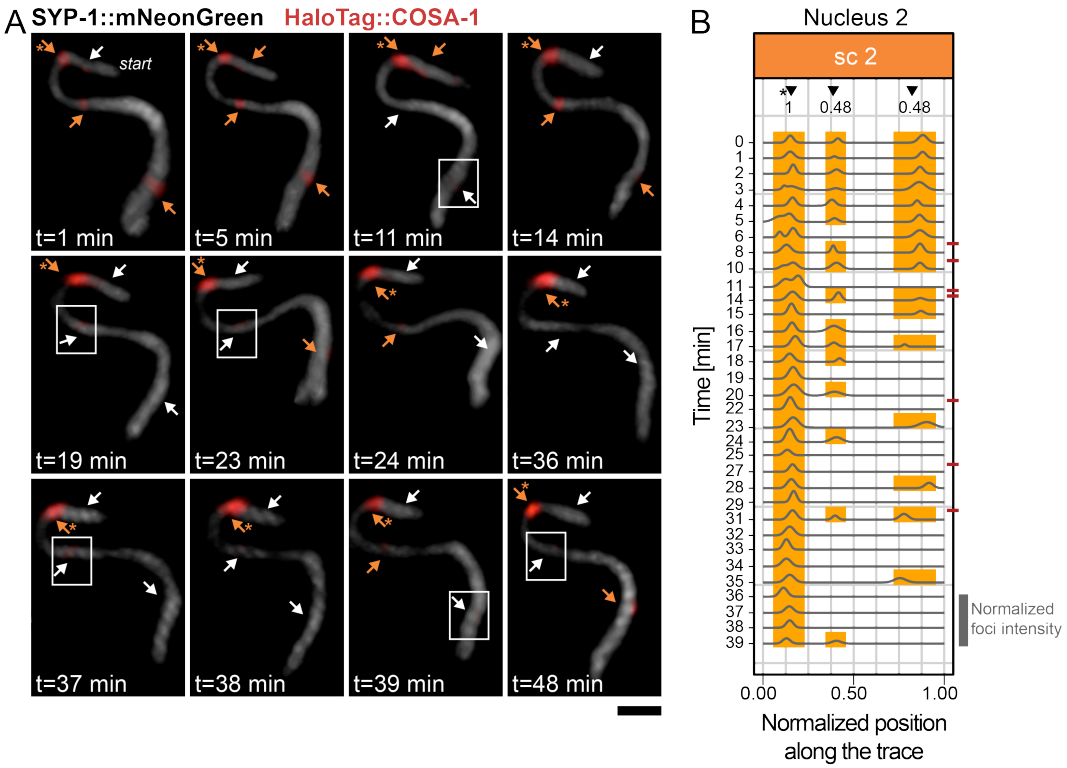


Figure 5.6. Comparison of the spotMAX results and the sharpened image of HaloTag::COSA-1 fluorescent signal

(A) Maximum intensity projection images showing one synaptonemal complex (marked by SYP-1::mNeonGreen, grey) and the pro-crossover marker COSA-1 (tagged with HaloTag7, orange). The HaloTag::COSA-1 signal shown corresponds to a sharpened image where the original image was processed with a difference of gaussian filter used in spotMAX prior to foci detection. The arrows point to regions of the synaptonemal complex that were associated with spotMAX-identified foci at least once during the timelapse. The orange colour of the arrow indicates that the foci were associated with a particular region at a given time point, whilst white indicates that the region has no associated foci (scale bars: 0.3 µm). Asterix next to the arrow denotes HaloTag::COSA-1 focus that is present and identified in all time frames. The white rectangles mark the regions of the synaptonemal complex with HaloTag::COSA-1 signal but without associated spotMAX-identified foci. The ”start” denotes the end of the synaptonemal complex that was used as a starting point of the trace and corresponds to position 0 along the synaptonemal complex in (B). The 3D views of the synaptonemal complex at different time points were aligned and rendered in the Imaris software (version 10.1.2). **(B)** Recreated HaloTag::COSA-1 intensity profiles along the traced synaptonemal complex at different time frames of a single time-lapse movie (scale bar: 1 [a.u.]. where 1 corresponds to the intensity of the brightest HaloTag::COSA-1 focus analysed in this study). The orange rectangle indicates the presence of at least one spotMAX-identified HaloTag::COSA-1 focus associated with a particular region of the chromosome. The number at the top of each region represents the fraction of frames in which the particular region of the synaptonemal complex is associated with at least one HaloTag::COSA-1 focus. The red lines on the right frame of the plot denote time frames that were excluded from the analysis due to severe movement of the animal during the acquisition of the Z-stack.

To investigate the dynamics of individual foci, I manually traced all six synaptonemal complexes for each of the four selected nuclei. I associated the spotMAX-identified foci to each of them based on the physical distance between the focus and synaptonemal complex[1]. **Figure 5.6** shows changes in the distribution of HaloTag::COSA-1 signal along one of the 24 traced chromosomes over 39 minutes. For this particular synaptonemal complex, one region is persistently associated with at least one HaloTag::COSA-1 focus for the entire duration of the timelapse movie **Figure 5.6A**, asterisk next to arrow). On the other hand, two additional regions are associated with a HaloTag::COSA-1 focus only at certain time frames (48% of the analysed frames, **Figure 5.6A**, arrows).

The comparison of the images of HaloTag::COSA-1 and the spotMAX analysis (**Figure 5.6A** for the sharpened HaloTag::COSA-1 signal[2] and **Figure G.4A** for the raw intensities), show that my analysis was able to faithfully describe the dynamics of HaloTag::COSA-1 over time. However, some discrepancies between the HaloTag::COSA-1 signal and the focus identification along the chromosomes remain. The discrepancies can primarily be attributed to the failure to identify very low signal as a focus (**Figure 5.6A**, white rectangles). Since this could at least in part be due to the stringent filtering of spotMAX-identified foci, better filtering methods for better foci detection methods should be explored in the future. Specifically, implementing a machine learning-based method to identify foci may further improve the results.

The fact that not all signal may be identified as a focus or that the signal of a small number of COSA-1 molecules may not be detectable above the background level highlights the limitation of the approach. For this reason, it is important to state that the terms *persistent* and *blinking* foci relate to the presence or occasional presence of a detectable fluorescent signal with a sufficient signal-to-noise ratio.

Nevertheless, my live imaging approach clearly identified two distinct populations of COSA-1 foci in mid-pachytene that differ in their dynamics that I termed *persistent* and *blinking* population. It is, therefore, tempting to speculate that *persistent* HaloTag::COSA-1 foci correspond to designated crossover sites, whereas *blinking* foci would correspond to other recombination intermediates that will be repaired

[1]For details on the length of the traces and distances between foci and their associated traces, please consult Figure G.2

[2]The sharpened image is the result of processing the raw signal with a difference of gaussian filter. This processing is performed by spotMAX before spot detection.

as non-crossovers. This would be a significant discovery since it is currently thought that crossover designation in *C. elegans*, similarly to plants (Morgan et al., 2021), is driven by an accumulation of pro-crossover factors at a subset of recombination intermediates that leads to the depletion of pro-crossover factors from other recombination intermediates (”coarsening model”, see section 1.4.1) (Zhang et al., 2018; Woglar and Villeneuve, 2018; Zhang et al., 2021). By contrast, my data indicates that crossover designation may be linked to the dynamics rather than the amount of certain pro-crossover factors. Furthermore, if *persistent* foci indeed correspond to designated crossover precursors, this would mean that the designation of the crossover site does not happen at the onset of late pachytene but earlier at some point during mid-pachytene.

To test whether recombination intermediates marked with persistently associated HaloTag::COSA-1 foci are indeed designated crossover sites, I took a closer look at the synaptonemal complexes that are associated with a single focus at the end of the timelapse movie (**Figure G.3**). The hypothesis is that the last remaining focus corresponds to the site at which COSA-1 protein would later accumulate, creating the bright focus in late pachytene.

Indeed, the recreated intensity profiles (**Figure 5.7**) show that the majority of the *blinking* foci can disappear and reappear several times before they disappear completely, and only a single focus remains along each synaptonemal complex. In most cases, the remaining focus is consistently present in all previous frames, and in other cases, the remaining focus is the focus present in the largest fraction of frames (97% for the analysed synaptonemal complexes; **Figure 5.7** the two left-most columns). I observed two synaptonemal complexes without persistent focus: For one (**Figure 5.7**, sc ”4” from nucleus ”1” (red), 11 min into the timelapse) of the two events, the absence is confirmed in the raw images (**Figure G.4B**, top-most panel). For the other event (**Figure 5.7**, sc ”1” from nucleus ”1” (red), 4 min into the timelapse) the region that is associated with the foci of the highest persistence cannot be easily distinguished from the region of the neighbouring *blinking* foci in the original image due to the orientation of the corresponding synaptonemal complex.

These results confirm that foci that are likely designated crossover precursors correspond to HaloTag::COSA-1 foci that are also persistent earlier in mid-pachytene. However, the final conclusion is only

valid if the notion is that the last remaining focus will also accumulate COSA-1 and create a bright focus once the nucleus reaches the late pachytene stage.

5.4. Blinking foci have lower intensity compared to persistent foci

To investigate the relationship between focus intensity and persistence at a given region of the synaptonemal complex, I identified foci reliably tracked for the duration of the timelapse. It is important to note that some regions, consistently or occasionally, have more than one associated focus (e.g. multiple peaks within orange rectangles of the left-most region in **Figure 5.6B** at 5 or 6 min into the timelapse) that are within the resolution limit from each other and cannot be distinguished reliably. Such foci were excluded when analysing the relationship between intensity and persistence (**Figure 5.8**) since the individual foci within such regions cannot be reliably tracked over time.

The intensity of *blinking* foci positively correlates with their ”frame presence”, which indicates the proportion of frames in which they were detected per movie. (**Figure 5.8**). However, *blinking* foci present in less than 75% frames have similar intensities. By contrast, confidently tracked *persistent* foci (n=3) have a higher intensity than the *blinking* foci. Importantly, *persistent* foci in mid-pachytene have lower intensities than *persistent* foci in late pachytene (nucleus ”4”). The intensity of the brightest mid-pachytene *persistent* focus is comparable to the intensity of the dimmest late pachytene focus, but it is 1.5 to 2.5-fold lower than the intensities of the remaining five late pachytene foci. In the time-lapse movies acquired so far, I observed that several late pachytene nuclei have a single focus that is dimmer than other foci. However, the prevalence of such nuclei remains to be assessed.

The current results indicate that the accumulation of COSA-1 at crossover precursors to the levels observed for late pachytene nuclei occurs after crossover are designated on all homologous chromosome pairs within a given nucleus. However, this conclusion can only be undoubtedly confirmed once the transition from mid- to late pachytene is observed within the time-lapse duration. Until such an event is observed, the notion that the high accumulation of the COSA-1 happens subsequently to crossover designation remains a speculation.

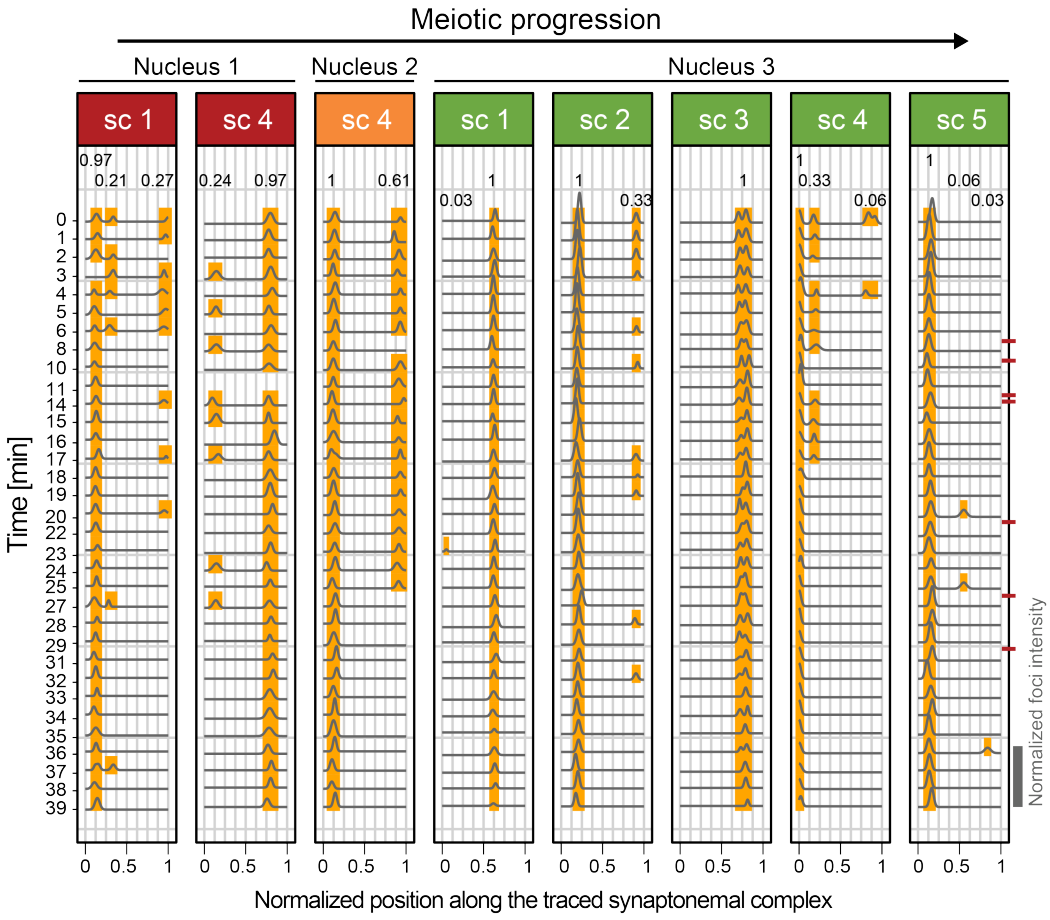


Figure 5.7. The last HaloTag::COSA-1 focus to remain attached to the individual synaptonemal complexes is, at the same time, the most persistent focus

HaloTag::COSA-1 intensity profiles along traced synaptonemal complexes recreated based on the spotMAX focus detection and 3D-gaussian fit results (scale bar: 1 [a.u.]. where value 1 corresponds to the intensity of the brightest HaloTag::COSA-1 focus analysed in this study). Only profiles of the mid-pachytene stage synaptonemal complexes that, by the end of the timelapse movie, have all but a single focus of HaloTag::COSA-1 associated with them are shown. The orange rectangles indicate the presence of at least one identified HaloTag::COSA-1 focus associated with a particular region of the synaptonemal complex at a given time point. The number at the top of each region represents the fraction of frames in which the particular region of the synaptonemal complex is associated with at least one HaloTag::COSA-1 foci. The red lines at the right-most edge of the plot mark time frames that are excluded from the analysis due to severe movement of the animal during the acquisition of the Z-stack. Differently coloured title boxes mark three different mid-pachytene nuclei from which the individual synaptonemal complexes were taken. The three nuclei are from different stages in mid-pachytene as indicated by the arrow at the top.

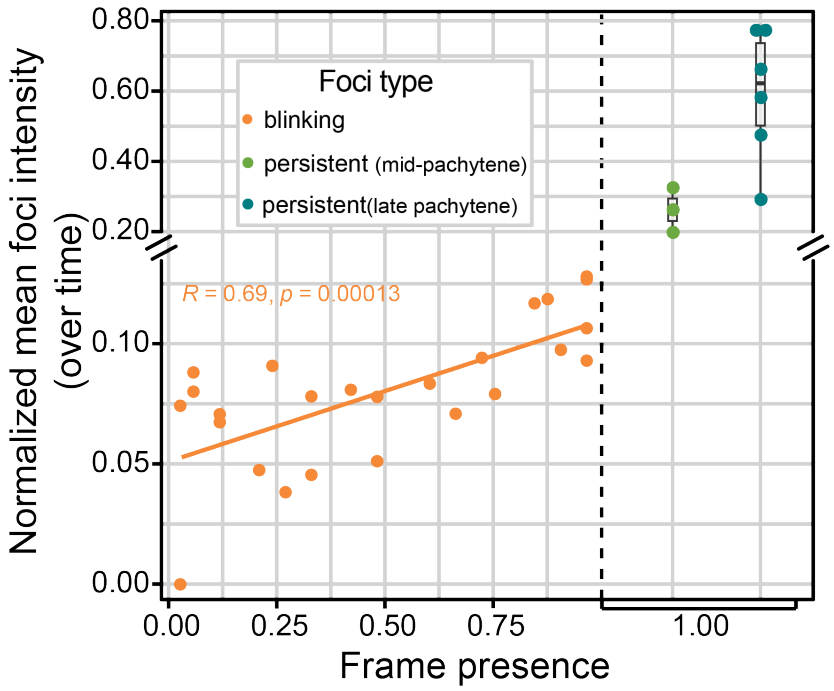


Figure 5.8. The relationship between HaloTag::COSA-1 focus intensity and persistence

For individual HaloTag::COSA-1 foci that can be confidently associated with a certain region of the manually traced synaptonemal complexes, the mean focus intensity during the timelapse movie was calculated and plotted against the fraction of time frames in which that focus is detected. For *blinking* foci whose frame presence varies, the Pearson correlation coefficient (R) was determined using functions from the *ggplot* (Wickham, 2016) R library.

5.5. Super-resolution imaging identifies the variety of MutSγ complex organization at recombination sites

I next asked whether the observed changes in the dynamics of COSA-1 foci correlate with changes in the ultrastructure of recombination intermediates during crossover designation. To analyze the ultrastructure of recombination sites, I used ratiometric 3D-SMLM to investigate the organization of a known pro-crossover factor, the MutSγ complex, at different stages of meiosis. Unlike the signalling molecule COSA-1 (cyclin-related protein, Yokoo et al. 2012), the MutSγ complex is present on all recombination intermediates due to its role in stabilizing recombination intermediates and the double Holliday junction (Snowden et al., 2004; Pochart et al., 1997; Baudat and Massy, 2007; Lynn et al., 2007). Additionally, the analysis of chromosome spreads of *C. elegans* meiotic nuclei suggested changes in the localisations of several crossover factors, including the MutSγ complex component MSH-5 (Woglar and Villeneuve, 2018).

However, the spreading of chromosomes only yields quasi-2D views and may distort critical structures, including the synaptonemal complex itself (Woglar and Villeneuve, 2018). Thus, valuable information that is crucial to elucidate how the designation of crossover sites influences its surrounding chromatin may be lost. For this reason, 3D-SMLM imaging is a valuable tool to investigate further the organization of crossover factors in their native environment.

Previous data from chromosome spreads suggested that designated crossovers are enclosed within a bubble formed by the synaptonemal complex components (Woglar and Villeneuve, 2018). However, when I localised the MutSγ complex component MSH-5 (tagged with V5 epitope tag MSH-5::V5) within meiotic chromosomes by 3D-SMLM, I observed that its signal is not confined within a bubble-like structure but that MSH-5::V5 rather localises above the plane of the synaptonemal complex (**Figure 5.9B**). This 3D-SMLM data thus resembles recombination nodules that were observed by electron microscopy of *Drosophila melanogaster* meiotic chromosomes (Carpenter, 1975).

Similar to work from Woglar and Villeneuve 2018, I acquired images at different regions of the gonad to capture the different stages of homologous recombination during mid- and late pachytene stages. This allowed me to roughly order the events by meiotic progression. To this end, I determined the

position of each nucleus imaged by SMLM relative to the position of the first row of diplotene nuclei (**Figure 5.9A**, numbers correspond to the number of rows of nuclei from diplotene).

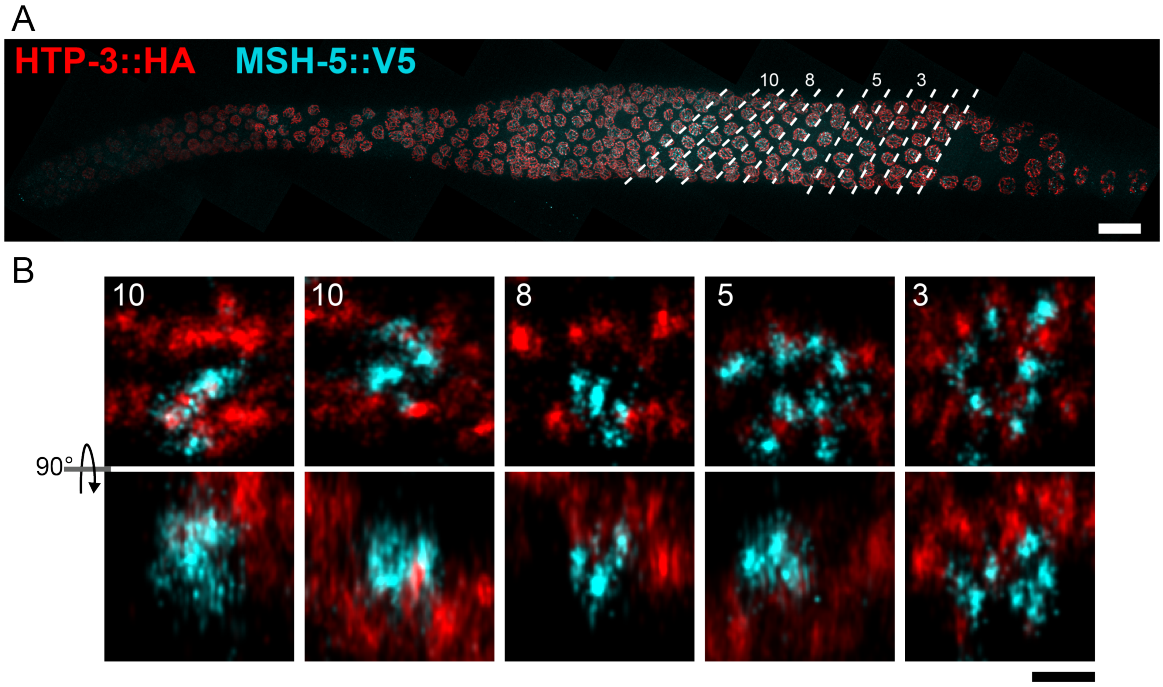


Figure 5.9. Ultrastructure of MSH-5::V5 foci resolved by single-molecule resolution microscopy

(A) Maximum intensity projection of a confocal microscopy image of a *C. elegans* germline stained for the chromosome axis component HTP-3 (C-terminally tagged with the hemagglutinin epitope tag, HTP-3::HA) and the pro-crossover factor and MutSγ complex component MSH-5 (C-terminally tagged with the V5 epitope tag, MSH-5::V5). Dashed lines separate rows of mid- and late pachytene nuclei, with the numbers indicating the number of rows left to the first row of diplotene nuclei. **(B)** 3D single-molecule localisation microscopy (SMLM) images of the ultrastructure of MSH-5::V5 foci at different stages of meiotic progression. Both frontal (top) and lateral views (bottom) are displayed. The number indicates the positioning of the nuclei within the gonad as shown in A. Scale bars: 10 µm (A), 100 nm (B).

As suggested by imaging chromosome spreads (Woglar and Villeneuve, 2018), the ultrastructure of MutSγ foci differs between mid- and late pachytene. In the previous study, imaging of chromosome spreads identified a ”singlet” configuration for MSH-5 foci in mid-pachytene and a ”doublet” organization in late pachytene (Woglar and Villeneuve, 2018). The doublet organization was connected to the formation of the double Holliday junction on the mechanistic level of double-strand break repair (**Figure 5.10B**). These double Holliday junctions are thought to yield crossovers, while singlet foci were interpreted as earlier recombination intermediates, e.g. single strand invasion events (**Figure**

5.10B) (Woglar and Villeneuve, 2018). However, the exact positioning is not known, and other possible association patterns of MutSγ complex are possible (e.g. **Figure 5.13A**).

The higher 3D resolution achieved by SMLM revealed that the ultrastructure of MSH-5::V5 foci is highly diverse across all imaged stages. To quantify the different shapes of MSH-5 foci, I annotated MSH-5 foci and fitted the localization pattern with an elliptical model (**Figure 5.10A**) using the maximum likelihood fitting framework (LocMoFit, Wu et al. 2022). The estimates of the major and minor axes of the model fitted to the individual sites of MSH-5::V5 localisation (**Figure 5.10A, C**) indicate that further progressed sites tend to have larger ultrastructures with larger major and minor axis estimates. It is important to note that this simple model cannot capture all of the detailed variations in the organization of the ultrastructure (e.g. **Figure 5.9B**). However, the model proved to be a valuable estimator of the spread of the MSH-5::V5 localisation at putative recombination intermediates.

Work from Woglar and Villeneuve 2018 established that the majority of late pachytene accumulations of the MutSγ complex at the synaptonemal complex represent designated crossover sites. Additional sites of MutSγ complex association with the synaptonemal complex that do not correspond to the six designated sites were occasionally observed in late pachytene, but in smaller numbers Woglar and Villeneuve (2018).

In the results of this study, late pachytene sites are sites that are less than seven nuclei rows away from the first diplotene nuclei. The 7th row from the diplotene generally corresponds to the transition from mid- to late pachytene since this row contains both nuclei with bright and nuclei with dim HaloTag::COSA-1 foci as observed in *in vivo* imaging of the germline (sections 5.1-5.3). Due to technical limitations[3], dim COSA-1 foci could not be detected and associated with the corresponding sites of MSH-5::V5 localisations. For this reason, the 7th row is only confirmed to have both nuclei with detectable and nuclei with undetectable signal in diffraction-limited images of HaloTag::COSA-1 signal. Based on the numbers of the MutSγ complex associations with the synaptonemal complex from Woglar and Villeneuve 2018, the majority of the MSH-5::V5 SMLM localisation sites in the 1st to 6th

[3]Here, the presence or absence of COSA-1 was recorded prior to SMLM acquisition by taking a snapshot of HaloTag::COSA-1 labelled with JaneliaFluor 503 (Grimm et al., 2015). The signal was then correlated with the MSH-5::V5 localisations. However, the JaneliaFluor 503 could not visualize dim COSA-1 signal in mid-pachytene nuclei.

row from diplotene correspond to the designated crossover sites in late pachytene. Therefore, I classified all sites with minor axis estimation above 40 nm and major axis estimate above 60 nm as putative designated sites. Indeed, the majority of late pachytene sites are identified as designated with these chosen boundaries (**Figure 5.10**)[4].

Furthermore, it is important to note that the separation is primarily based on separating the late and mid-pachytene sites, and upon closer inspection, I noticed four dominant shapes of MSH-5::V5 SMLM localisation across the sites (**Figure 5.10 C**, shaded areas). Although there is a certain degree of variability, a general shape describing the majority of the foci can be found within each group (**Figure 5.10C** and **5.10D**): large elliptical structures, large doublets, small doublets, and singlet structures. Interestingly, the relation between the organization of each shape and its meiotic timing had several important implications.

Firstly, large elliptical structures correspond to the largest observed ultrastructures (i.e. with minor axis above 55 nm). These structures only occur in late pachytene (closer than the 7th row to diplotene, **Figure 5.10C-D, *elliptical***). These sites tend to have a more elliptical organisation of the MutSγ complex (**Figure 5.10B-C**) or two parallel localisation bands that are longer (**Figure 5.9B-C**, two right-most images) than those observed for the sites grouped as *larger doublet* shape (**Figure 5.10C-D**).

Secondly, I observed organizations similar to the doublet organization of the MutSγ complex previously reported in structured illumination microscopy (SIM) imaging of chromosome spreads (Woglar and Villeneuve, 2018). However, with superior resolution of the 3D-SMLM and perhaps the preservation of the 3D organization lost in chromosome spreads, I could detect a doublet organization of the MutSγ complex prior to the late pachytene stage. This is an exciting result since a doublet organization was previously only associated with designated sites in late pachytene stage (Woglar and Villeneuve, 2018; Haversat et al., 2022). The earlier doublet organizations with two parallel groups of MSH-5::V5 localisations were observed as early as in the 11th row from diplotene, which is currently the earliest timing from which SMLM images have been acquired (**Figure 5.10D**, second image on the left). Such *small doublets* were named as such due to the small size of the two groups of MSH-5::V5 localisations

[4]Note, this classification will have to be confirmed by assessing the co-localisation with bright HaloTag::COSA-1 foci. However, the additional information required for this is not yet integrated into the data analysis

and are observed as late as the 5th row to diplotene. Somewhat *larger doublet* structures have been observed as early as the 9th, and as late as the 3rd row to diplotene stage.

Finally, all sites with a minor axis smaller than 30 nm have been termed singlet organizations of MSH-5::V5 SMLM localisations (**Figure 5.10C-D**, red). However, a variety of structures can be detected within the group. The ultrastructure of those sites mainly corresponds to small clusters of SMLM localizations (i.e. both axis estimated below 30 nm), or singlets that appear elongated with major axis up to 60 nm (**Figure 5.10D**). Occasionally, two singlet organizations can be observed in proximity to each other, at opposing sides or at different distances from the synaptonemal complex plane along the *z*-axis (direction of imaging). Two closely adjacent sites may also be grouped together into single sites giving rise to very long elliptical structures (**Figure 5.10C-D**, the major axis is two or four-fold larger than the minor axis). I hypothesize that two neighbouring recombination sites can explain such events. Indeed, double-strand breaks are frequently introduced in close proximity during meiosis (Johnson et al., 2021) indicating that two distinct recombination intermediates may be in close proximity to each other. Alternatively, these sites could result from the proximity of nucleoplasmic background staining (when localisation clusters are distant to the localisations of the chromosome axis). Further investigation is required to validate these claims since they are based on my manual inspection of the data as displayed in **Figure 5.10C**.

In summary, the current results provide insights into the organization of the MutSγ complex at different stages of double-strand break repair by homologous recombination. Specifically, singlet (**Figure 5.13B**) organizations likely correspond to the stabilization of single strand invasion events as previously implicated in Haversat et al. 2022. The *elongated singlets* could either correspond to the same events by extension of the invading strand or early second end capture events **Figure 5.13B**). In the first case, the addition of MutSγ complexes to the extending strand would result in two neighbouring clusters of MSH-5::V5 localisations associated with the invading strand[5]. However, while this scenario could explain the elongated singlets (marked as singlets in **Figure 5.10D**, red), it is unlikely that

[5]It is important to keep in mind that with the current set-up, the fluorophore associated to the MSH-5::V5 localisations is bound to its target protein through combination of the primary antibody and F(ab')$_2$. This means that the fluorophore is found at approx. 20 nm distant from the MSH-5 protein itself.

the *small doublets*, that I was able to observe for the first time, (**Figure 5.10C-D**, orange) correspond to anything but the stabilization of the second end capture events (**Figure 5.13B**). Similarly, *larger doublets* could correspond to subsequent processing events of a recombination intermediate after second end capture and double Holliday junction formation (**Figure 5.13B**). Following this reasoning, the differing sizes of *larger doublets*, as well as the larger *elliptical* ultrastructures observed in late pachytene could be explained by the subsequent processing of the double-strand break and branch migration (further discussed in section 5.7).

Interestingly, *large doublets* appear as early as in the 9th row from diplotene (**Figure 5.10D**, middle panel). This appearance of *large doublets* coincides with the observation of *persistent* HaloTag::COSA-1 foci in *in vivo* imaging experiments(section 5.1-5.3). I, therefore, believe that both super-resolution organisation and the *in vivo* imaging have identified a crossover precursor that can be distinguished from other intermediates in mid-pachytene. These exciting results would implicate that crossover designation in *C. elegans* happens earlier than the onset of the late pachytene.

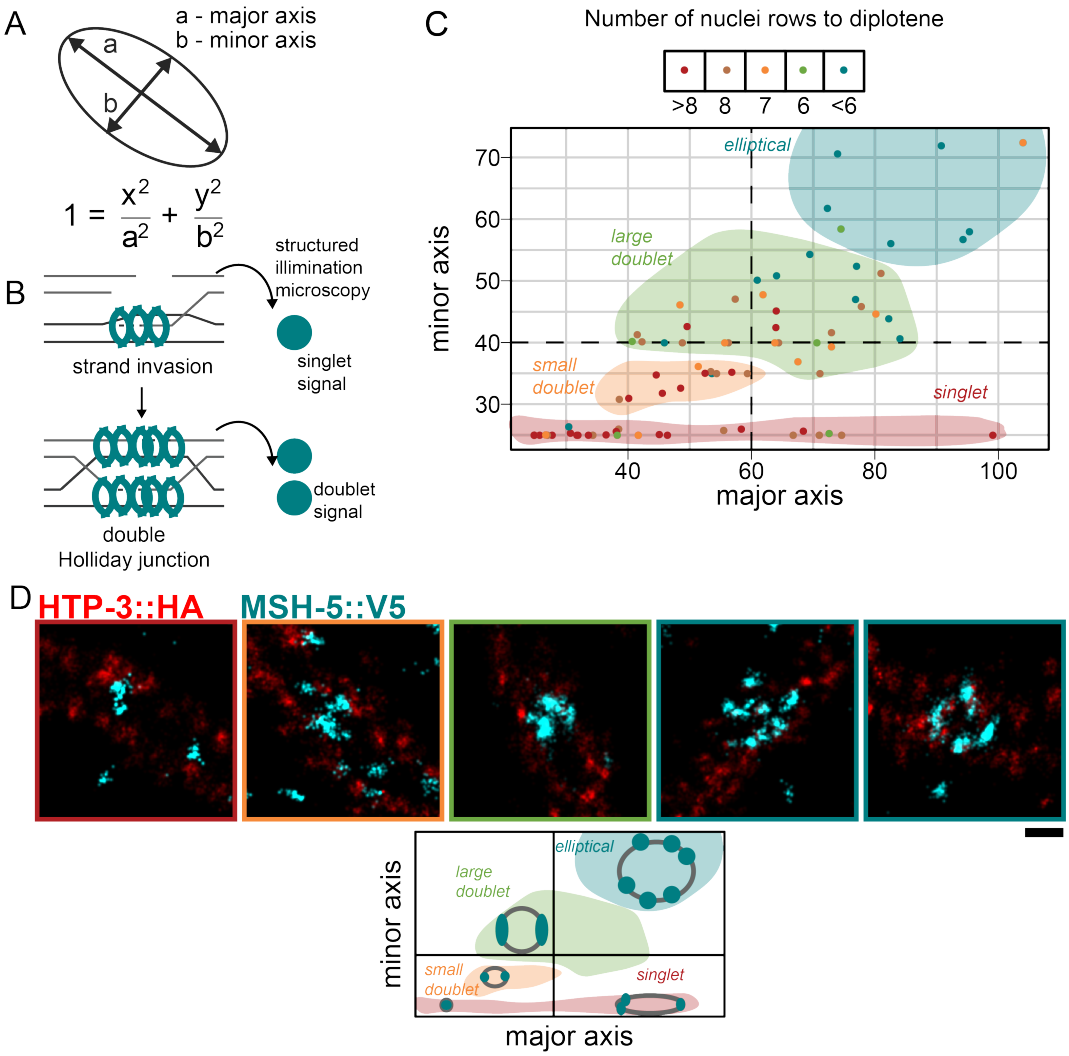


Figure 5.10. MutSγ complex distribution at recombination intermediates

(A) Graphic illustrating the two main parameters of the elliptical model that was fitted to the ultrastructure of MSH-5::V5 foci using the maximum likelihood fitting framework (LocMoFit, Wu et al. 2022), i.e. major and minor axis. **(B)** Illustration showing the association of a singlet and doublet signal in chromosome spreads imaged by structured illumination microscopy and the stage of the homologous recombination as proposed in Woglar and Villeneuve 2018. **(C)** The results of the maximum likelihood fitting of the elliptical model to the 3D localisations of the MSH-5::V5. The shaded areas group the sites with similar organisation of MSH-5::V5 SMLM localisations. The term used to describe the shape of each group is written in the corresponding colour. **(D)** Bottom: Illustration of the most dominant ultrastructure of MSH-5::V5 foci within each group specified in C. Top: Rendered images of single-molecule localisation microscopy (SMLM) localisations of MSH-5::V5. The images show several different organizations of MSH-5::V5 localisations (cyan). Additionally, the localisations corresponding to the chromosome axis component HTP-3::HA are shown in red to demonstrate the orientation of the synaptonemal complex and the view in which the localisations are observed (scale bar: 100 nm). The outline of each panel indicates to which shape group the site belongs to.

5.6. Chromosome axes distortions in proximity of crossover precursors

More recently, a growing number of evidence accumulated in support of the previously disputed active role of the synaptonemal complex in regulating crossover designation (Hayashi et al., 2010; Libuda et al., 2013; Wang et al., 2015; Pattabiraman et al., 2017; Woglar and Villeneuve, 2018; Morgan et al., 2021; Köhler et al., 2020; Zhang et al., 2021). It was suggested that the synaptonemal complex regulates the differential timing of crossover and non-crossover events by creating distinct compartments that isolate crossover precursors from other non-crossover destined intermediates (Woglar and Villeneuve, 2018).

In my preliminary studies of synaptonemal complex organization around the designated crossover sites, I observed differing degrees of structural rearrangements at recombination intermediates in both, mid-pachytene and late-pachytene nuclei (results not shown). The rearrangements can be described as an abrupt change in the angle between the chromosome axes (a sharp twist) or highly curved bends (high curvature of the synaptonemal complex midline). In extreme cases, chromosome axes on one side of the crossover site are perpendicular to the chromosome axes on the other side of the crossover site in late pachytene (**Figure 5.11**, right). Thus, the angle of the axes changes from 0° on the left side to 90° on the right side of the crossover site. This change in the angle is abrupt (i.e. it occurs within a short stretch of the synaptonemal complex), as opposed to the more frequently observed ribbon-like behaviour of gradual twisting of the synaptonemal complex. An example of the latter behaviour can be seen in the image of a mid-pachytene synaptonemal complex in **Figure 5.11** (left).

Importantly, SMLM images of designated crossovers in intact tissues did not recapitulate the previously postulated bubble-like organization of the synaptonemal complex that envelops crossover designated in chromosome spreads (Woglar and Villeneuve, 2018). However, the drastic twists and/or bending of chromosome axes at designated crossover sites may give rise to bubble-like structures upon spreading.

These preliminary data suggested that not only the ultrastructure of the pro-crossover factor MSH-5 but also the conformation of the chromosome axes changes upon crossover (or non-crossover) matu-

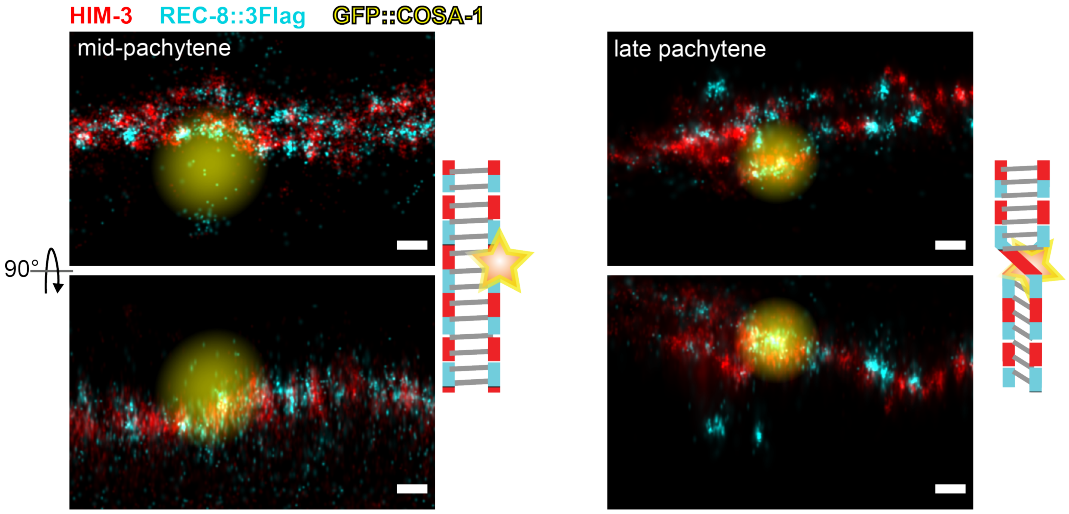


Figure 5.11. Chromosome axis rearrangements at crossover precursor sites
Images show the organization of the chromosome axis at different stages of meiotic progression. Left: recombination intermediate identified as a dim GFP::COSA-1 focus in mid-pachytene (no abrupt axis rearrangement is observed but the axes gradually bend along the overall structure). Right: designated crossover site identified as a bright GFP::COSA-1 focus in late pachytene (perpendicular placement of the axis on the opposing sides of the crossover site). Cartoons represent the observed organization of the synaptonemal complex with axes in red/cyan and central region for reference in grey. The recombination intermediate (left) and designated crossover (right) are shown as yellow stars.

ration. This was an interesting observation since chromosome axes have been previously connected with the spreading of the crossover interference signal (Kleckner et al., 2004), and such rearrangements could potentially be important for the execution of the crossover since axes are also exchanged between the two chromosomes Zickler and Kleckner (2015). I therefore next characterised the organization of the organization of the chromosome axis component HTP-3 (HTP-3::HA) around the designated crossover sites identified in the previous section 5.5 (**Figure 5.9**-**5.10**).

To this end, I first identified MSH-5::V5 sites that correspond to ”designated” sites (**Figure 5.10C**, minor axis above 40 nm and major axis above 60 nm). I then compared the distribution of parameters that describe the organization of the synaptonemal complex (curvature, axis angle change, synaptonemal complex width) between segments near designated crossover sites (350-400 nm) and more distant segments along annotated stretches of the synaptonemal complex[6] (**Figure 5.12**).

[6]The partitioning of synaptonemal complexes into segments and their analysis is described in sections 3.7.3-3.7.4. For details on the total length of the analysed stretches and the number of segments, please consult **Table G.1**. Additionally, the number of analysed MSH-5::V5 sites are listed in **Table G.2**

Excitingly, the analysis of the chromosome axis organization was able to capture several aspects of the distortions observed at ”designated” MSH-5::V5 sites. Chromosome axes bend more in the proximity of ”designated” MSH-5::V5 sites (greater curvature, **Figure 5.12A**), and axes twist abruptly (greater angle change, **Figure 5.12B**) compared to the general behaviour of the chromosome axes signal along stretches at a distance from designated crossovers. Interestingly, ”designated” MSH-5::V5 sites are associated with synaptonemal complex regions where chromosome axes are closer together (**Figure 5.12C**). However, this result remains preliminary and requires further investigation since the *p*-value for goodness-of-fit comparison of changes in width is higher than for changes in curvature and angle (**Figure 5.12**).

Previously, changes in the organization (Köhler et al., 2020) and dynamics (Nadarajan et al., 2017; Pattabiraman et al., 2017) of synaptonemal complex components have been associated with the transition from mid- to late pachytene. Since a majority of the sites marked as ”designated” are located after the transition, the observed differences in the chromosome axis organization in the proximity of ”designated” MSH-5::V5 sites may be a consequence of the general changes in synaptonemal complex organization connected with meiotic progression.

At this point, it remains difficult to precisely distinguish the cause-consequence relationship between crossover designation and the observed rearrangements of the axes, since the significant local rearrangements of the chromosome axes have been associated with sites that presumably are already designated crossover sites, and no significant rearrangements are associated with the remaining MSH-5::V5 sites (**Figure 5.12**). Thus, the observed rearrangements could be the consequence of the maturation of the recombination intermediates into crossover sites and the formation of a double Holliday junction. Whether these rearrangements could be subsequently involved in or contribute to the propagation of the crossover interference signal and prevent similar occurrences along the synaptonemal complex remains to be investigated.

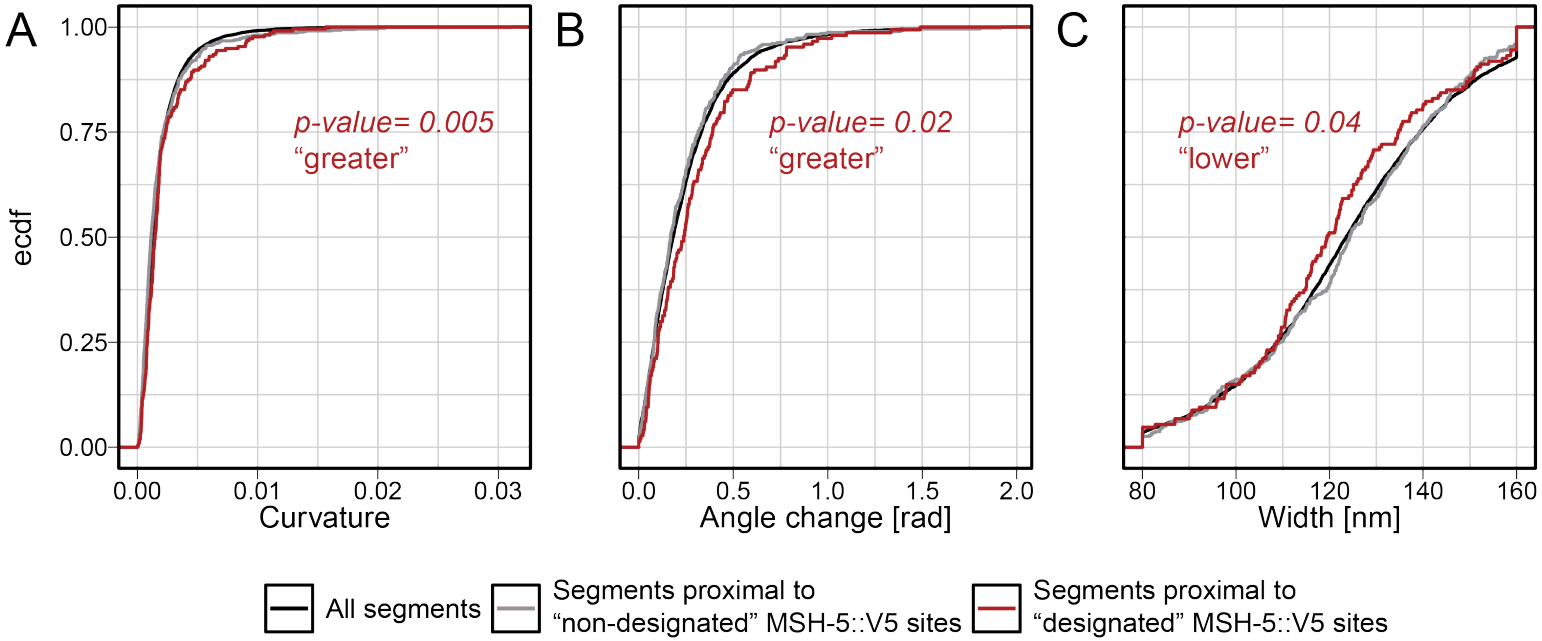


Figure 5.12. Characterising the organization of the synaptonemal complex in proximity to putative designated crossover sites

Comparison of empirical cumulative distributions (ecdf) of curvature **(A)**, angle change **(B)**, and the width of the synaptonemal complex **(C)** along analysed synaptonemal complex stretches at a distance from recombination sites (black) and segments in proximity to MSH-5::V5 foci labelled as designated in **Figure 5.10** (red), or in proximity to the remainder of MSH-5::V5 foci (grey). Distribution of each parameter in proximity to the sites termed as designates was compared to the overall distribution of the same parameter (”All segments”) by one-sided Kolmogorov-Smirnov goodness-of-fit (Kolmogorov, 1933; Smirnov, 1939) test (R, version 4.2.2). The resulting *p*-value, and the directionality of the test are indicated on the corresponding plots in red.

5.7. Discussion

In *C. elegans*, several different recombination factors are known to accumulate at designated crossover sites. These include pro-crossover factors such as COSA-1, MSH-5, and ZHP-1/2/3/4 (Yokoo et al., 2012; Zhang et al., 2018; Jantsch et al., 2004; Woglar and Villeneuve, 2018; Bhalla et al., 2008; Nguyen et al., 2018). These accumulations likely correspond to recombination nodules that were observed e.g. in electron micrographs of *Drosophila* oocytes (Carpenter, 1975). The majority of recombination intermediates are smaller nodules that are found along the synaptonemal complex. Further accumulation of pro-crossover factors may then give rise to larger recombination nodules that are thought to yield designated crossover sites that will eventually be resolved into class I crossovers (Zhang et al., 2018; Woglar and Villeneuve, 2018; Zhang et al., 2021).

MSH-5 is a component of the MutSγ complex that is involved in the stabilisation of recombination intermediates and Holliday junctions (Snowden et al., 2004; Pochart et al., 1997; Baudat and Massy, 2007; Lynn et al., 2007). In *C. elegans* meiosis, the number of immunostained MutSγ complex foci peaks in early pachytene and subsequently drops to largely six foci per nucleus in late pachytene, marking the designated crossover sites (Woglar and Villeneuve, 2018; Haversat et al., 2022). Recently, it has been proposed that CDK-2 (the kinase partner to the cyclin-like pro-crossover factor COSA-1) drives crossover designation through phosphorylation of the MutSγ complex component MSH-5 (Haversat et al., 2022; Zhang et al., 2021). The authors proposed that a positive feedback mechanism between CDK-2 and its target MSH-5 promotes the accumulation and activity of other pro-crossover factors. Structured illumination microscopy of chromosome spreads also suggested that designated crossovers are identified by a doublet ultrastructure of the MutSγ complex and specialised compartments formed by the synaptonemal complex (Woglar and Villeneuve, 2018; Haversat et al., 2022). By contrast, the MutSγ complex forms a ”singlet” structure in earlier recombination intermediates (Woglar and Villeneuve, 2018; Haversat et al., 2022). However, this observation does not exclude the possibility that a subset of such earlier recombination intermediates may already be designated to become crossovers before their ultrastructure changes from the singlet to the doublet state in chromosome spreads.

I propose that identifying the two distinct populations of recombination intermediates in mid-pachytene that differ in their dynamics vouches for an earlier designation that occurs separately on each chromosome pair. In this case, the accumulation of pro-crossover factors would follow once all chromosome pairs gain a designated crossover site and the crossover assurance checkpoint is satisfied. Indeed, such a timing of crossover designation in *C. elegans* would be consistent with the timing of crossover designation in yeast (Fung et al., 2004; Machovina et al., 2016).

My data suggested that sites with highly *persistent* HaloTag::COSA-1 foci that are observed in mid-pachytene correspond to the recombination intermediates that are designated crossover precursors. Consequently, the sites of more dynamic COSA-1 association (i.e. *blinking* foci) would correspond to recombination intermediates that result in non-crossovers. Furthermore, with SMLM imaging, a wider variety of MutSγ complex has been observed. Interestingly, the ”doublet” organizations that were previously only observed for designated crossover sites in late pachytene (Woglar and Villeneuve, 2018) are now also found earlier in mid-pachytene. In the previous study where chromosome spreads were imaged by structured illumination microscopy, the doublets observed in late pachytene are thought to represent double Holliday junctions (**Figure 5.10B**, and Woglar and Villeneuve 2018). If the formation of the double Holliday junction indeed corresponds to crossover designation, my data again implies an earlier crossover designation than previously thought in *C. elegans*. To this end, the *larger doublet* organisations (**Figure 5.10C-D**) of the MutSγ complex ultrastructure would correspond to stabilised crossover precursors that are also marked by *persistent* HaloTag::COSA-1 foci in vivo (**Figure 5.13B**). Indeed, the highly persistent foci and large doublet organisation compromise ~50% of recombination intermediates recognised in experiments in this study. For these calculations, *persistent* foci corresond to foci that are present more than 90% of the time (**Figure 5.8**). Additionally, very elongated *singlet* organizations (**Figure 5.10D-C**, high ratio of the major to minor axis estimates) are treated as two independent recombination intermediates each in *singlet organisation*. Together, these data strongly suggested that crossovers are indeed designated earlier than commonly thought in *C. elegans*. The timing of crossover designation in *C. elegans* may thus be more similar to the timing observed in other model organisms such as yeast (Fung et al., 2004). Therefore, the fundamental cellular mechanism

of crossover designation during meiosis may be more conserved than previously thought. However, the data presented here is still preliminary and a more direct comparison of the prevalence of potential early CO designation is required. To this end, the dynamics of the HaloTag::COSA-1 must be assessed in a more significant number of meiotic nuclei. Similarly, the co-localisation of the MutSγ complex and COSA-1 during the mid-pachytene must be analyzed.

Importantly, although the analogy of *persistent* foci and larger doublet organisation of MSH-5::V5 localisations is striking, the question of whether they truly correspond to designated crossover precursors must be tested further. Specifically, the proposition that MSH-5 doublets indeed correspond to designated crossovers relies on the hypothesis that a doublet organisation of the MutSγ complex represents the stabilisation of the second end capture and double Holliday junction. However, this hypothesis initially formed by Woglar and Villeneuve 2018 is yet to be confirmed. To this end, studying the organization of the MutSγ complex in mutants with reduced activity of double-strand break repair factors included in the Holliday junction formation could help shed light on the association between the two. Alternatively, a correlative study of the structure with SMLM and electron microscopy could provide evidence. However, this approach might prove difficult due to a limited number of events within the tissue and a lack of techniques for preparing the *C. elegans* germline tissue. Furthermore, the exact location of the MutSγ complex is not fully elucidated, and alternative organizations to the one proposed in (Woglar and Villeneuve, 2018) and in this study are possible **e.g. Figure 5.13A**. Hence, further structural studies of the MutSγ complex and its association with chromatin will provide answers to the validity of the currently proposed association between the MutSγ complex organization at recombination intermediates and the organizations observed by light microscopy.

Additionally, since I could only analyze the dynamics of HaloTag::COSA-1 foci in a limited number of nuclei, the conclusions must still be considered preliminary. Specifically, observing the transition from mid- to late pachytene with a drastic accumulation of COSA-1 after crossover designation is crucial. However, this transition is likely very rapid and thus rare (approximately 1 event per hour). Thus, more timelapse movies are required to observe this transition. Additionally, the contribution of photobleaching must be addressed in more detail.

Nevertheless, with the proposed assumptions in mind, the results of this study are consistent with several previously reported determinants of double-strand break repair processes and crossover regulation.

Namely, the previously reported phosphorylation dependant feedback loop between C-terminus of MutSγ complex component MHS-5 and COSA-1 dependant kinase CDK-2 (Haversat et al., 2022; Zhang et al., 2021) provides the basis for the analogy between the sites with highly *persistent* COSA-1 signal and sites of larger accumulation and changes in the ultrastructure of MSH-5::V5 localisations during mid-pachytene. In this scenario, persistent COSA-1 would activate more CDK-2 kinase, which will, in return, lead to the recruitment of more MutSγ complex due to the described feedback loop (Haversat et al., 2022).

Furthermore, a previous analysis of chromosome spreads showed that not all MutSγ complex foci co-localised with dim COSA-1 signal during mid-pachytene (Woglar and Villeneuve, 2018). However, the result of the *in vivo* imaging presented here suggests that the lack of the observed co-localisation between MutSγ complex and COSA-1 foci at certain recombination intermediates could result from the fact that the highly dynamic behaviour of COSA-1 cannot be captured in fixed images (discussed further in section 5.8).

The larger organisations of MSH-5::V5 in SMLM experiments that coincide with the appearance of bright COSA-1 signal in late pachytene could result from the reported propensity of MSH-5 protein for condensation (Haversat et al., 2022; Zhang et al., 2021). However, I hypothesise that such condensates would result in a less organised ultrastructure of MSH-5::V5 foci when imaged by SMLM. Alternatively, the changes in the ultrastructure of the MutSγ complex could reflect the underlying progression of double-strand break repair (**Figure 5.13B**) as previously proposed (Woglar and Villeneuve, 2018). In line with this argument, smaller organisations of MSH-5::V5 SMLM localisations could correspond to earlier recombination intermediates that precede the distinction between crossover precursors and other recombination intermediates. Various larger organisations may correspond to events proposed to be crossover-specific intermediates in yeast and mice. In these organisms, the double Holliday junction resolution is thought to be a crossover-specific feature (Peterson et al., 2020; Ahuja et al.,

2021). The larger organisation of MSH-5::V5 SMLM localisations in mid-pachytene could correspond to a higher number of MutSγ complexes needed to stabilise crossover specific intermediates such as the transition from single-end intermediate to second end capture (Hunter and Kleckner, 2001) or the Holliday junction itself (Holliday, 1964). Further accumulation of the MutSγ complex at the onset of late pachytene could be required to form the Holliday junction or reflect branch migration that was observed in yeast (Ahuja et al., 2021). However, the connection between MutSγ complex organisations observed in SMLM and the underlying double-strand break repair mechanisms remains highly speculative and further investigation is necessary to corroborate such claims (section 5.8).

Although more *in vivo* imaging data is necessary, the current data supports a model in which the accumulation of COSA-1 and MutSγ complex at the onset of the late pachytene happens after crossovers are designated on all six chromosome pairs. Although this scenario was questioned more recently for *C. elegans*, the claim is not without precedent since similar conclusions were drawn in Libuda et al. 2013 and Machovina et al. 2016. This sequence of events could be explained by the presence of a nucleus-wide regulation and the existence of a crossover assurance checkpoint at the transition from mid- to late pachytene that prevents the accumulation of pro-crossover factors before all chromosomes gained a designated crossover site. This nucleus-wide signal may consist of an interplay between the polo-like kinase PLK-2 and CHK-2 kinase that leads to the inactivation of CHK-2 at the onset of late pachytene (Zhang et al., 2023). Furthermore, the inactivation of CHK-2 kinase was connected to the accumulation of COSA-1 at designated crossover sites (Zhang et al., 2023). The basis for the changes in the organisation of the synaptonemal complex in response to crossover designation (Libuda et al., 2013; Machovina et al., 2016) that would lead to the establishment of the crossover interference could not be observed directly in this study. Future investigation in the organisation and dynamics of other synaptonemal complex components and pro-crossover factors might answer how the interference signal spreads from the designated site.

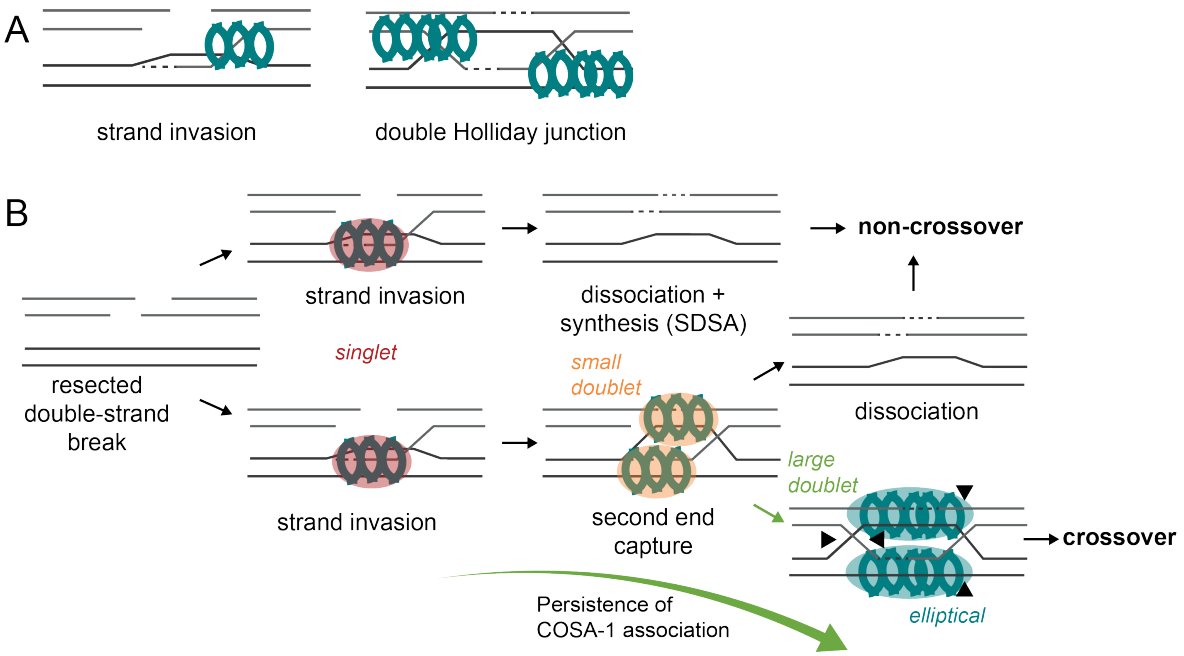


Figure 5.13. Model for the association of MutSγ complex at recombination intermediates
(A) The illustration shows examples of an alternative association of the MutSγ complex to the recombination intermediates. **(B)** Illustration showing a possible correspondence between homologous recombination intermediates and observed organization of the single-molecule localisation microscopy (SMLM) localisations of MutSγ complex component MSH-5. The MutSγ complex is represented by the dark-cyan rings, while the colour of the surrounding shading in B indicates association to a particular organization.

5.8. Outlook

The results of this study offer insights into the timing of crossover designation. However, some conclusions drawn from the results are still speculative and must be corroborated with additional tests of the assumptions on which they are based.

Firstly, more evidence for the analogy of *persistent* HaloTag::COSA-1 foci observed *in vivo* and the specific organisations of the MSH-5::V5 localisations in *in situ* SMLM is required. Secondly, capturing the transition from mid- to late pachytene of the individual meiotic nucleus is necessary to make definite conclusions on how crossover designation and the accumulation of pro-crossover factors to the designated sites relate in the sequence of events *in vivo*. Lastly, the relationship between the variety of MutSγ complex organisations observed by SMLM and the underlying double-strand break repair events needs to be tested further.

In vivo imaging of the MutSγ complex may address several limitations of this study. Specifically, as-

sessing the persistence and intensity of MutSγ complex foci could provide evidence that higher levels of MSH-5 accumulation relate to the *persistence* of COSA-1 foci. To this end, I have endogenously tagged MSH-5 with HaloTag9 (Frei et al., 2021) and COSA-1 with mNeonGreen. However, the required imaging experiments have not been performed yet. In the long term, it will be essential to study how inhibiting the formation of crossover-specific intermediates or perturbing the activity of meiotic kinases (e.g. CHK-2, CDK-2, PLK-2) influences the dynamics of recombination intermediates in mid-pachytene.

Currently, image analysis of both *in vivo* and super-resolution *in situ* experiments limit the amount of data that can be acquired and interpreted. Therefore, further automation of the image analysis pipeline developed in this study is required. Specifically, analysing individual synaptonemal complexes in *in vivo* imaging experiments remains cumbersome. Currently, a very limited amount of the acquired data can be quantitatively described, and investigation into the proposed perturbations would be unrealistic without increased automation.

Concluding remarks

The great advantage of the *C. elegans* as a model organism for studying meiosis is the large abundance and spatiotemporal orientation of meiotic nuclei within the germline tissue (Lui and Colaiácovo, 2013). These features are especially valuable for the cytological studies of meiotic events.

This study describes an optimised immunohistochemistry protocol that allows SMLM localisation of meiotic proteins within intact gonad tissues. In previously published work, the application of this protocol has led to valuable insights into the localisation and function of newly identified synaptonemal complex components (Hurlock et al., 2020; Blundon et al., 2023).

In this study, SMLM imaging of the intact germlines identified the organization of the MutSγ complex above the synaptonemal complex in a manner that resembles recombination nodules that were observed by electron microscopy of *Drosophila melanogaster* meiotic chromosomes (Carpenter, 1975). Additionally, SMLM imaging of the recombination intermediates presented here has hinted at the existence of several distinct organizations of the MutSγ complex. The appearance of distinct organizations of the MutSγ complex at recombination intermediates in mid-pachytene coincides with the observance of the distinct *persistence* of COSA-1 foci imaged *in vivo*. The distinction of the two populations of the recombination intermediates in mid-pachytene could have important implications on the timing of the crossover designation timing in *C. elegans*. However, additional confirmation of such claims will be necessary.

The study offers several tools for the cytological investigation of the *C. elegans* germline. Namely, the specifically tailored image analysis pipeline quantitatively describes the diffraction-limited foci within meiotic nuclei in *in vivo* time-lapse experiments. Furthermore, the re-purposing of existing tools for the analysis of the SMLM data allows for the investigation of 3D-SMLM localisations of synaptonemal complex components and proteins associated with the synaptonemal complex. These tools offer a basis for the further exploration of the crossover designation processes in *C. elegans*.

Bibliography

Ahuja, J. S., Harvey, C. S., Wheeler, D. L., and Lichten, M. (2021). Repeated strand invasion and extensive branch migration are hallmarks of meiotic recombination. *Molecular Cell*, 81(20):4258–4270.e4.

Allers, T. and Lichten, M. (2001). Differential timing and control of noncrossover and crossover recombination during meiosis. *Cell*, 106(1):47–57.

Almanzar, D. E., Gordon, S. G., and Rog, O. (2021). Meiotic sister chromatid exchanges are rare in *C. elegans*. *Current Biology*, 31(7):1499–1507.e3.

Altmann, S. L. (1986). Rotations, quaternions, and double groups.

Anderson, L. K., Royer, S. M., Page, S. L., McKim, K. S., Lai, A., Lilly, M. A., and Hawley, R. S. (2005). Juxtaposition of C(2)M and the transverse filament protein C(3)G within the central region of *Drosophila* synaptonemal complex. *Proceedings of the National Academy of Sciences of the United States of America*, 102:4482.

Banterle, N., Bui, K. H., Lemke, E. A., and Beck, M. (2013). Fourier ring correlation as a resolution criterion for super-resolution microscopy. *Journal of Structural Biology*, 183:363–367.

Baudat, F. and Massy, B. D. (2007). Regulating double-stranded dna break repair towards crossover or non-crossover during mammalian meiosis. *Chromosome Research*, 15:565–577.

Betzig, E., Patterson, G. H., Sougrat, R., Lindwasser, O. W., Olenych, S., Bonifacino, J. S., Davidson, M. W., Lippincott-Schwartz, J., and Hess, H. F. (2006). Imaging intracellular fluorescent proteins at nanometer resolution. *Science*, 313(5793):1642–1645.

Bhalla, N., Wynne, D. J., Jantsch, V., and Dernburg, A. F. (2008). ZHP-3 acts at crossovers to couple meiotic recombination with synaptonemal complex Disassembly and Bivalent Formation in *C. elegans*. *PLOS Genetics*, 4(10):e1000235.

Bhatla, N. and Horvitz, H. R. (2015). Light and hydrogen peroxide inhibit *C. elegans* feeding through gustatory receptor orthologs and pharyngeal neurons. *Neuron*, 85:804–818.

Blundon, J., Cesar, B., Bae, J. W., Čavka, I., Haversat, J., Ries, J., Köhler, S., and Kim, Y. (2023). Skp1 proteins are structural components of the synaptonemal complex in *C. elegans*. *bioRxiv*.

Bossi, M., Föiling, J., Belov, V. N., Boyarskiy, V. P., Medda, R., Egner, A., Eggeling, C., Schönle, A., and Hell, S. W. (2008). Multicolor far-field fluorescence nanoscopy through isolated detection of distinct molecular species. *Nano letters*, 8:2463–2468.

Brenner, S. (1974). The genetics of *Caenorhabditis elegans*. *Genetics*, 77:71–94.

Cahoon, C. K., Yu, Z., Wang, Y., Guo, F., Unruh, J. R., Slaughter, B. D., and Hawley, R. S. (2017). Superresolution expansion microscopy reveals the three-dimensional organization of the *Drosophila* synaptonemal complex. *Proceedings of the National Academy of Sciences*, 114(33):E6857–E6866.

Capilla-Pérez, L., Durand, S., Hurel, A., Lian, Q., Chambon, A., Taochy, C., Solier, V., Grelon, M., and Mercier, R. (2021). The synaptonemal complex imposes crossover interference and heterochiasmy in *Arabidopsis*. *Proceedings of the National Academy of Sciences*, 118(12):e2023613118.

Cardozo, T. and Pagano, M. (2004). The scf ubiquitin ligase: insights into a molecular machine. *Nature Reviews Molecular Cell Biology 2004 5:9*, 5:739–751.

Carpenter, A. T. (1975). Electron microscopy of meiosis in *Drosophila melanogaster* females. I. Structure, arrangement, and temporal change of the synaptonemal complex in wild-type. *Chromosoma*, 51(2):157–182.

Čavka, I., Power, R. M., Walsh, D., Zimmermann, T., and Köhler, S. (2022). Super-resolution microscopy of the synaptonemal complex within the *Caenorhabditis elegans* germline. *JoVE (Journal of Visualized Experiments)*, 2022:e64363.

Chen, F., Tillberg, P. W., and Boyden, E. S. (2015). Expansion microscopy. *Science*, 347(6221):543–548.

Cho, S. W., Lee, J., Carroll, D., Kim, J. S., and Lee, J. (2013). Heritable gene knockout in *Caenorhabditis elegans* by direct injection of Cas9-sgRNA ribonucleoproteins. *Genetics*, 195:1177–1180.

Cieslinski, K., Wu, Y. L., Nechyporenko, L., Hörner, S. J., Conti, D., Skruzny, M., and Ries, J. (2023). Nanoscale structural organization and stoichiometry of the budding yeast kinetochore. *The Journal of cell biology*, 222.

Colaiácovo, M. P. (2006). The many facets of SC function during *C. elegans* meiosis. *Chromosoma*, 115(3):195–211.

Colaiácovo, M. P., MacQueen, A. J., Martinez-Perez, E., McDonald, K., Adamo, A., La Volpe, A., and Villeneuve, A. M. (2003). Synaptonemal complex assembly in *C. elegans* is dispensable for loadingstrand-exchange proteins but critical for proper completion of recombination. *Developmental Cell*, 5(3):463–474.

Couteau, F., Nabeshima, K., Villeneuve, A., and Zetka, M. (2004). A component of *C. elegans* meiotic chromosome axes at the interface of homolog alignment, synapsis, nuclear reorganization, and recombination. *Current Biology*, 14(7):585–592.

Couteau, F. and Zetka, M. (2005). HTP-1 coordinates synaptonemal complex assembly with homolog alignment during meiosis in *C. elegans*. *Genes and Development*, 19(22):2744–2756.

Crittenden, S. L., Troemel, E. R., Evans, T. C., and Kimble, J. (1994). Glp-1 is localized to the mitotic region of the *C. elegans germ* line. *Development (Cambridge, England)*, 120:2901–2911.

de Boer, E., Stam, P., Dietrich, A. J. J., Pastink, A., and Heyting, C. (2006). Two levels of interference in mouse meiotic recombination. *Proceedings of the National Academy of Sciences*, 103(25):9607–9612.

Deo, C., Abdelfattah, A. S., Bhargava, H. K., Berro, A. J., Falco, N., Farrants, H., Moeyaert, B., Chupanova, M., Lavis, L. D., and Schreiter, E. R. (2021). The HaloTag as a general scaffold for far-red tunable chemigenetic indicators. *Nature Chemical Biology 2021 17:6*, 17:718–723.

Dernburg, A. F., McDonald, K., Moulder, G., Barstead, R., Dresser, M., and Villeneuve, A. M. (1998). Meiotic recombination in c. elegans initiates by a conserved mechanism and is dispensable for homologous chromosome synapsis. *Cell*, 94(3):387–398.

D'Errico, J. (2012). *interparc*. MATLAB Central File Exchange.

Deschamps, J., Kieser, C., Hoess, P., Deguchi, T., and Ries, J. (2023). MicroFPGA: An affordable FPGA platform for microscope control. *HardwareX*, 13:e00407.

Deschamps, J. and Ries, J. (2020). EMU: reconfigurable graphical user interfaces for Micro-Manager. *BMC Bioinformatics*, 21:1–13.

Deschamps, J., Rowald, A., and Ries, J. (2016). Efficient homogeneous illumination and optical sectioning for quantitative single-molecule localization microscopy. *Opt. Express*, 24(24):28080–28090.

Diekmann, R., Kahnwald, M., Schoenit, A., Deschamps, J., Matti, U., and Ries, J. (2020). Optimizing imaging speed and excitation intensity for single molecule localization microscopy. *Nature methods*, 17(9):909.

Duroc, Y., Lemhemdi, A., Larchevêque, C., Hurel, A., Cuacos, M., Cromer, L., Horlow, C., Armstrong, S. J., Chelysheva, L., and Mercier, R. (2014). The kinesin atpss1 promotes synapsis and is required for proper crossover distribution in meiosis. *PLOS Genetics*, 10(10):1–11.

Edgar, L. G. (1995). Blastomere culture and analysis. *Methods in cell biology*, 48(C):303–321.

Elliott, A. D. (2020). Confocal microscopy: Principles and modern practices. *Current protocols in cytometry*, 92:e68.

Ershov, D., Phan, M.-S., Pylvänäinen, J. W., Rigaud, S. U., Blanc, L. L., Charles-Orszag, A., Conway, J. R. W., Laine, R. F., Roy, N. H., Bonazzi, D., Duménil, G., Jacquemet, G., and Tinevez, J.-Y. (2021). Bringing TrackMate into the era of machine-learning and deep-learning. *bioRxiv*, page 2021.09.03.458852.

Ester, M., Kriegel, H.-P., Sander, J., and Xu, X. (1996). A density-based algorithm for discovering clusters in large spatial databases with noise. In *Proceedings of the Second International Conference on Knowledge Discovery and Data Mining*, KDD'96, page 226–231. AAAI Press.

Fraune, J., Alsheimer, M., Volff, J.-N., Busch, K., Fraune, S., Bosch, T. C. G., and Benavente, R. (2012). *Hydra* meiosis reveals unexpected conservation of structural synaptonemal complex proteins across metazoans. *Proceedings of the National Academy of Sciences*, 109(41):16588–16593.

Frei, M. S., Tarnawski, M., Roberti, M. J., Koch, B., Hiblot, J., and Johnsson, K. (2021). Engineered HaloTag variants for fluorescence lifetime multiplexing. *Nature Methods 2021 19:1*, 19(1):65–70.

Frøkjær-Jensen, C., Davis, M. W., Hopkins, C. E., Newman, B. J., Thummel, J. M., Olesen, S. P., Grunnet, M., and Jorgensen, E. M. (2008). Single-copy insertion of transgenes in *Caenorhabditis elegans*. *Nature genetics*, 40:1375–1383.

Fung, J. C., Rockmill, B., Odell, M., and Roeder, G. (2004). Imposition of crossover interference through the nonrandom distribution of synapsis initiation complexes. *Cell*, 116(6):795–802.

Ghanta, K. S. and Mello, C. C. (2020). Melting dsDNA donor molecules greatly improves precision genome editing in *Caenorhabditis elegans*. *Genetics*, 216:643–650.

Girard, C., Zwicker, D., and Mercier, R. (2023). The regulation of meiotic crossover distribution: a coarse solution to a century-old mystery? *Biochemical Society Transactions*, 51(3):1179–1190.

Gomez, K. A. R. and Schvarzstein, M. (2018). Immobilization of nematodes for live imaging using an agarose pad produced with a vinyl record. *microPublication Biology*, 2018.

Goodyer, W., Kaitna, S., Couteau, F., Ward, J. D., Boulton, S. J., and Zetka, M. (2008). HTP-3 links DSB formation with homolog pairing and crossing over during *C. elegans* meiosis. *Developmental Cell*, 14(2):263–274.

Grimm, J. B., English, B. P., Chen, J., Slaughter, J. P., Zhang, Z., Revyakin, A., Patel, R., Macklin, J. J., Normanno, D., Singer, R. H., Lionnet, T., and Lavis, L. D. (2015). A general method to improve fluorophores for live-cell and single-molecule microscopy. *Nature methods*, 12(3):244.

Guan, Y., Adrian Leu, N., Ma, J., Chmátal, L., Ruthel, G., Bloom, J. C., Lampson, M. A., Schimenti, J. C., Luo, M., and Jeremy Wang, P. (2020). SKP1 drives the prophase I to metaphase I transition during male meiosis. *Science Advances*, 6(13).

Gustafsson, M. G. (2000). Surpassing the lateral resolution limit by a factor of two using structured illumination microscopy. *Journal of Microscopy*, 198(2):82–87.

Harris, C. R., Millman, K. J., van der Walt, S. J., Gommers, R., Virtanen, P., Cournapeau, D., Wieser, E., Taylor, J., Berg, S., Smith, N. J., Kern, R., Picus, M., Hoyer, S., van Kerkwijk, M. H., Brett, M., Haldane, A., del Río, J. F., Wiebe, M., Peterson, P., Gérard-Marchant, P., Sheppard, K., Reddy, T., Weckesser, W., Abbasi, H., Gohlke, C., and Oliphant, T. E. (2020). Array programming with *NumPy*. *Nature*, 585(7825):357–362.

Haversat, J., Woglar, A., Klatt, K., Akerib, C. C., Roberts, V., Chen, S. Y., Arur, S., Villeneuve, A. M., and Kim, Y. (2022). Robust designation of meiotic crossover sites by CDK-2 through phosphorylation of the MutSγ complex. *Proceedings of the National Academy of Sciences of the United States of America*, 119:e2117865119.

Hayashi, M., Mlynarczyk-Evans, S., and Villeneuve, A. M. (2010). The synaptonemal complex shapes the crossover landscape through cooperative assembly, crossover promotion and crossover inhibition during *Caenorhabditis elegans* meiosis. *Genetics*, 186(1):45–58.

Hell, S. W. and Wichmann, J. (1994). Breaking the diffraction resolution limit by stimulated emission: stimulated-emission-depletion fluorescence microscopy. *Optics Letters*, 19(11):780.

Hemmer, L. W. and Blumenstiel, J. P. (2016). Holding it together: Rapid evolution and positive selection in the synaptonemal complex of *Drosophila*. *BMC Evolutionary Biology*, 16:1–17.

Hermanson, G. T. (2013). *Bioconjugate techniques*. Academic press.

Hess, S. T., Girirajan, T. P., and Mason, M. D. (2006). Ultra-high resolution imaging by fluorescence photoactivation localization microscopy. *Biophysical Journal*, 91(11):4258–4272.

Hesse, S., Zelkowski, M., Mikhailova, E. I., Keijzer, C. J., Houben, A., and Schubert, V. (2019). Ultrastructure and dynamics of synaptonemal complex components during meiotic pairing and synapsis of standard (a) and accessory (b) rye chromosomes. *Frontiers in Plant Science*, 10.

Hicks, T., Trivedi, S., Eppert, M., Bowman, R., Tian, H., Dafalla, A., Crahan, C., Smolikove, S., and Silva, N. (2022). Continuous double-strand break induction and their differential processing sustain chiasma formation during *Caenorhabditis elegans* meiosis. *Cell Reports*, 40(13):111403.

Hillers, K. J., Jantsch, V., Martinez-Perez, E., and Yanowitz, J. L. (2017). *Meiosis*. The *C. elegans* Research Community, WormBook.

Hoess, P., Mund, M., Reitberger, M., and Ries, J. (2018). Dual-color and 3D super-resolution microscopy of multi-protein assemblies. In *Methods in molecular biology (Clifton, N.J.)*, volume 1764, pages 237–251. Humana Press, New York, NY.

Holliday, R. (1964). A mechanism for gene conversion in fungi. *Genetics Research*, 5(2):282–304.

Hunter, N. (2015). Meiotic recombination: The essence of heredity. *Cold Spring Harbor Perspectives in Biology*, 7(12):a016618.

Hunter, N. and Kleckner, N. (2001). The single-end invasion: An asymmetric intermediate at the double-strand break to double-holliday junction transition of meiotic recombination. *Cell*, 106(1):59–70.

Hurlock, M. E., Čavka, I., Kursel, L. E., Haversat, J., Wooten, M., Nizami, Z., Turniansky, R., Hoess, P., Ries, J., Gall, J. G., Rog, O., Köhler, S., and Kim, Y. (2020). Identification of novel synaptonemal complex components in *C. elegans*. *Journal of Cell Biology*, 219(5).

Jantsch, V., Pasierbek, P., Mueller, M. M., Schweizer, D., Jantsch, M., and Loidl, J. (2004). Targeted Gene Knockout Reveals a Role in Meiotic Recombination for ZHP-3, a Zip3-Related Protein in *Caenorhabditis elegans*. *Molecular and Cellular Biology*, 24(18):7998–8006.

Jaramillo-Lambert, A., Ellefson, M., Villeneuve, A. M., and Engebrecht, J. (2007). Differential timing of S phases, X chromosome replication, and meiotic prophase in the *C. elegans* germ line. *Developmental Biology*, 308(1):206–221.

Johnson, D., Crawford, M., Cooper, T., Bouuaert, C. C., Keeney, S., Llorente, B., Garcia, V., and Neale, M. J. (2021). Concerted cutting by Spo11 illuminates meiotic DNA break mechanics. *Nature 2021 594:7864*, 594:572–576.

Kassambara, A. (2023). *ggpubr: 'ggplot2' Based Publication Ready Plots*. R package version 0.6.0.

King, J. S. and Mortimer, R. K. (1990). A polymerization model of chiasma interference and corresponding computer simulation. *Genetics*, 126 4:1127–38.

Klar, T. A., Jakobs, S., Dyba, M., Egner, A., and Hell, S. W. (2000). Fluorescence microscopy with diffraction resolution barrier broken by stimulated emission. *Proceedings of the National Academy of Sciences of the United States of America*, 97(15):8206–8210.

Kleckner, N., Zickler, D., Jones, G. H., Dekker, J., Padmore, R., Henle, J., and Hutchinson, J. (2004). A mechanical basis for chromosome function. *Proceedings of the National Academy of Sciences of the United States of America*, 101(34):12592–7.

Köhler, S., Wojcik, M., Xu, K., and Dernburg, A. F. (2017). Superresolution microscopy reveals the three-dimensional organization of meiotic chromosome axes in intact *Caenorhabditis elegans* tissue. *Proceedings of the National Academy of Sciences of the United States of America*, 114(24):E4734–E4743.

Köhler, S., Wojcik, M., Xu, K., and Dernburg, A. F. (2020). The interaction of crossover formation and the dynamic architecture of the synaptonemal complex during meiosis. *bioRxiv*, page 2020.02.16.947804.

Kohli, J. and Bähler, J. (1994). Homologous recombination in fission yeast: Absence of crossover interference and synaptonemal complex.

Kolmogorov, A. N. (1933). Sulla determinazione empirica di una legge didistribuzione. *Giorn Dell'inst Ital Degli Att*, 4:89–91.

Kursel, L. E., Cope, H. D., and Rog, O. (2021). Unconventional conservation reveals structure-function relationships in the synaptonemal complex. *eLife*, 10:e72061.

Lampe, A., Haucke, V., Sigrist, S. J., Heilemann, M., and Schmoranzer, J. (2012). Multi-colour direct storm with red emitting carbocyanines. *Biology of the cell*, 104:229–237.

Lawrence, M., Huber, W., Pagès, H., Aboyoun, P., Carlson, M., Gentleman, R., Morgan, M. T., and Carey, V. J. (2013). Software for computing and annotating genomic ranges. *PLOS Computational Biology*, 9:e1003118.

Lelek, M., Gyparaki, M. T., Beliu, G., Schueder, F., Griffié, J., Manley, S., Jungmann, R., Sauer, M., Lakadamyali, M., and Zimmer, C. (2021). Single-molecule localization microscopy. *Nature Reviews Methods Primers 2021 1:1*, 1:1–27.

Li, Y., Mund, M., Hoess, P., Deschamps, J., Matti, U., Nijmeijer, B., Sabinina, V. J., Ellenberg, J., Schoen, I., and Ries, J. (2018). Real-time 3D single-molecule localization using experimental point spread functions. *Nature Methods*, 15(5):367–369.

Li, Y., Shi, W., Liu, S., Cavka, I., Wu, Y.-L., Matti, U., Wu, D., Köhler, S., and Ries, J. (2022). Global fitting for high-accuracy multi-channel single-molecule localization. *Nature Communications 2022 13:1*, 13(1):1–11.

Libuda, D. E., Uzawa, S., Meyer, B. J., and Villeneuve, A. M. (2013). Meiotic chromosome structures constrain and respond to designation of crossover sites. *Nature*, 502(7473):703–6.

Liu, J. G., Yuan, L., Brundell, E., Björkroth, B., Daneholt, B., and Höög, C. (1996). Localization of the N-terminus of SCP1 to the central element of the synaptonemal complex and evidence for direct interactions between the N-termini of SCP1 molecules organized head-to-head. *Experimental cell research*, 226:11–19.

Liu, S., Hoess, P., and Ries, J. (2022). Super-resolution microscopy for structural cell biology. *Annual Review of Biophysics*, 51(1):301–326. PMID: 35119945.

Los, G. V., Encell, L. P., McDougall, M. G., Hartzell, D. D., Karassina, N., Zimprich, C., Wood, M. G., Learish, R., Ohana, R. F., Urh, M., Simpson, D., Mendez, J., Zimmerman, K., Otto, P., Vidugiris, G., Zhu, J., Darzins, A., Klaubert, D. H., Bulleit, R. F., and Wood, K. V. (2008). HaloTag: A novel protein labeling technology for cell imaging and protein analysis. *ACS Chemical Biology*, 3(6):373–382.

Lui, D. Y. and Colaiácovo, M. P. (2013). Meiotic Development in *Caenorhabditis elegans*. In *Advances in experimental medicine and biology*, volume 757, pages 133–170. Springer, New York, NY.

Lynn, A., Soucek, R., and Börner, G. V. (2007). ZMM proteins during meiosis: Crossover artists at work. *Chromosome Research*, 15:591–605.

Machovina, T. S., Mainpal, R., Daryabeigi, A., McGovern, O., Paouneskou, D., Labella, S., Zetka, M., Jantsch, V., and Yanowitz, J. L. (2016). A surveillance system ensures crossover formation in C. elegans. *Current Biology*, 26(21):2873–2884.

MacQueen, A. J., Colaiácovo, M. P., McDonald, K., and Villeneuve, A. M. (2002). Synapsis-dependent and -independent mechanisms stabilize homolog pairing during meiotic prophase in *C. elegans*. *Genes development*, 16(18):2428–42.

Martinez-Perez, E. and Villeneuve, A. M. (2005). HTP-1-dependent constraints coordinate homolog pairing and synapsis and promote chiasma formation during *C. elegans* meiosis. *Genes Development*, 19(22):2727–2743.

Mazia, D., Schatten, G., and Sale, W. (1975). Adhesion of cells to surfaces coated with polylysine. Applications to electron microscopy. *Journal of Cell Biology*, 66:198–200.

Morgan, C., Fozard, J. A., Hartley, M., Henderson, I. R., Bomblies, K., and Howard, M. (2021). Diffusion-mediated HEI10 coarsening can explain meiotic crossover positioning in Arabidopsis. *Nature Communications 2021 12:1*, 12(1):1–11.

Mund, M., Tschanz, A., Wu, Y.-L., Frey, F., Mehl, J. L., Kaksonen, M., Avinoam, O., Schwarz, U. S., and Ries, J. (2023). Clathrin coats partially preassemble and subsequently bend during endocytosis. *Journal of Cell Biology*, 222.

Mund, M., van der Beek, J. A., Deschamps, J., Dmitrieff, S., Hoess, P., Monster, J. L., Picco, A., Nédélec, F., Kaksonen, M., and Ries, J. (2018). Systematic nanoscale analysis of endocytosis links efficient vesicle formation to patterned actin nucleation. *Cell*, 174(4):884–896.e17.

Nadarajan, S., Lambert, T. J., Altendorfer, E., Gao, J., Blower, M. D., Waters, J. C., and Colaiácovo, M. P. (2017). Polo-like kinase-dependent phosphorylation of the synaptonemal complex protein SYP-4 regulates double-strand break formation through a negative feedback loop. *eLife*, 6.

Nayak, S., Santiago, F. E., Jin, H., Lin, D., Schedl, T., and Kipreos, E. T. (2002). The *Caenorhabditis elegans* Skp1-related gene family: Diverse functions in cell proliferation, morphogenesis, and meiosis. *Current Biology*, 12:277–287.

Nguyen, H., Labella, S., Silva, N., Jantsch, V., and Zetka, M. (2018). *C. elegans* ZHP-4 is required at multiple distinct steps in the formation of crossovers and their transition to segregation competent chiasmata. *PLOS Genetics*, 14(10):e1007776.

Nieuwenhuizen, R. P., Lidke, K. A., Bates, M., Puig, D. L., Grünwald, D., Stallinga, S., and Rieger, B. (2013). Measuring image resolution in optical nanoscopy. *Nature Methods*, 10(6):557–562.

Olivier, N., Keller, D., Gönczy, P., and Manley, S. (2013). Resolution Doubling in 3D-STORM Imaging through Improved Buffers. *PLoS ONE*, 8(7):e69004.

Oreopoulos, J., Berman, R., and Browne, M. (2014). Chapter 9 - spinning-disk confocal microscopy: present technology and future trends. In Waters, J. C. and Wittman, T., editors, *Quantitative Imaging in Cell Biology*, volume 123 of *Methods in Cell Biology*, pages 153–175. Academic Press.

Pachitariu, M. and Stringer, C. (2022). Cellpose 2.0: How to train your own model. *Nature Methods 2022 19:12*, 19:1634–1641.

Paix, A., Folkmann, A., Rasoloson, D., and Seydoux, G. (2015). High efficiency, homology-directed genome editing in *Caenorhabditis elegans* using CRISPR-Cas9 ribonucleoprotein complexes. *Genetics*, 201:47–54.

Pattabiraman, D., Roelens, B., Woglar, A., and Villeneuve, A. M. (2017). Meiotic recombination modulates the structure and dynamics of the synaptonemal complex during *C. elegans* meiosis. *PLOS Genetics*, 13(3):e1006670.

Pazhayam, N. M., Turcotte, C. A., and Sekelsky, J. (2021). Meiotic crossover patterning. *Frontiers in Cell and Developmental Biology*, 9.

Pedregosa, F., Varoquaux, G., Gramfort, A., Michel, V., Thirion, B., Grisel, O., Blondel, M., Prettenhofer, P., Weiss, R., Dubourg, V., Vanderplas, J., Passos, A., Cournapeau, D., Brucher, M., Perrot, M., and Duchesnay, E. (2011). *scikit-learn*: Machine learning in Python. *Journal of Machine Learning Research*, 12:2825–2830.

Peterson, S. E., Keeney, S., and Jasin, M. (2020). Mechanistic insight into crossing over during mouse meiosis. *Molecular Cell*, 78(6):1252–1263.e3.

Phillips, C. M., McDonald, K. L., and Dernburg, A. F. (2009). Cytological analysis of meiosis in *Caenorhabditis elegans*. In *Methods in molecular biology (Clifton, N.J.)*, volume 558, pages 171–195. Humana Press, Totowa, NJ.

Pochart, P., Woltering, D., and Hollingsworth, N. M. (1997). Conserved properties between functionally distinct muts homologs in yeast. *Journal of Biological Chemistry*, 272:30345–30349.

Prakash, K., Fournier, D., Redl, S., Best, G., Borsos, M., Tiwari, V. K., Tachibana-Konwalski, K., Ketting, R. F., Parekh, S. H., Cremer, C., and Birk, U. J. (2015). Superresolution imaging reveals structurally distinct periodic patterns of chromatin along pachytene chromosomes. *Proceedings of the National Academy of Sciences of the United States of America*, 112(47):14635–14640.

Preibisch, S., Saalfeld, S., and Tomancak, P. (2009). Globally optimal stitching of tiled 3D microscopic image acquisitions. *Bioinformatics (Oxford, England)*, 25(11):1463–5.

R Core Team (2019). *R: A language and environment for statistical computing*. R Foundation for Statistical Computing, Vienna, Austria.

Ries, J. (2020). SMAP: a modular super-resolution microscopy analysis platform for SMLM data. *Nature methods*, 17(9):870–872.

Rog, O. and Dernburg, A. (2015). Direct Visualization Reveals Kinetics of Meiotic Chromosome Synapsis. *Cell Reports*, 10(10):1639–1645.

Rog, O., Köhler, S., and Dernburg, A. F. (2017). The synaptonemal complex has liquid crystalline properties and spatially regulates meiotic recombination factors. *eLife*, 6.

Rosu, S., Libuda, D. E., and Villeneuve, A. M. (2011). Robust crossover assurance and regulated interhomolog access maintain meiotic crossover number. *Science*, 334(6060):1286–1289.

Rust, M. J., Bates, M., and Zhuang, X. (2006). Sub-diffraction-limit imaging by stochastic optical reconstruction microscopy (STORM). *Nature Methods*, 3(10):793–796.

Sabinina, V. J., Hossain, M. J., Hériché, J. K., Hoess, P., Nijmeijer, B., Mosalaganti, S., Kueblbeck, M., Callegari, A., Szymborska, A., Beck, M., Ries, J., and Ellenberg, J. (2021). A Highlights from MBoC Selection: Three-dimensional superresolution fluorescence microscopy maps the variable molecular architecture of the nuclear pore complex. *Molecular Biology of the Cell*, 32(17):1523.

Sanger, F., Nicklen, S., and Coulson, A. R. (1977). DNA sequencing with chain-terminating inhibitors. *Proceedings of the National Academy of Sciences of the United States of America*, 74:5463.

Schermelleh, L., Ferrand, A., Huser, T., Eggeling, C., Sauer, M., Biehlmaier, O., and Drummen, G. P. (2019). Super-resolution microscopy demystified. *Nature Cell Biology 2019 21:1*, 21:72–84.

Schild-Prüfert, K., Saito, T. T., Smolikov, S., Gu, Y., Hincapie, M., Hill, D. E., Vidal, M., McDonald, K., and Colaiácovo, M. P. (2011). Organization of the synaptonemal complex during meiosis in *Caenorhabditis elegans*. *Genetics*, 189(2):411–421.

Schindelin, J., Arganda-Carreras, I., Frise, E., Kaynig, V., Longair, M., Pietzsch, T., Preibisch, S., Rueden, C., Saalfeld, S., Schmid, B., Tinevez, J. Y., White, D. J., Hartenstein, V., Eliceiri, K., Tomancak, P., and Cardona, A. (2012). Fiji: an open-source platform for biological-image analysis. *Nature Methods 2012 9:7*, 9:676–682.

Schmekel, K., Meuwissen, R. L., Dietrich, A. J., Vink, A. C., Marle, J. V., Veen, H. V., and Heyting, C. (1996). Organization of SCP1 protein molecules within synaptonemal complexes of the rat. *Experimental cell research*, 226:20–30.

Schröder, D., Deschamps, J., Dasgupta, A., Matti, U., and Ries, J. (2020). Cost-efficient open source laser engine for microscopy. *Biomed. Opt. Express*, 11(2):609–623.

Schücker, K., Holm, T., Franke, C., Sauer, M., and Benavente, R. (2015). Cytoplasmic microtubular images in glutaraldehyde-fixed tissue culture cells by electron microscopy and by immunofluorescence microscopy. *PNAS*, 75(4):1820–1824.

Severson, A. F., Ling, L., Van Zuylen, V., and Meyer, B. J. (2009). The axial element protein HTP-3 promotes cohesin loading and meiotic axis assembly in *C. elegans* to implement the meiotic program of chromosome segregation. *Genes and Development*, 23(15):1763–1778.

Shaner, N. C., Lambert, G. G., Chammas, A., Ni, Y., Cranfill, P. J., Baird, M. A., Sell, B. R., Allen, J. R., Day, R. N., Israelsson, M., Davidson, M. W., and Wang, J. (2013). A bright monomeric green fluorescent protein derived from *Branchiostoma lanceolatum*. *Nature Methods 2013 10:5*, 10:407–409.

Shi, X., Lim, J., and Ha, T. (2010). Acidification of the oxygen scavenging system in single-molecule fluorescence studies: in situ sensing with a ratiometric dual-emission probe. *Analytical chemistry*, 82(14):6132–6138.

Sieben, C., Banterle, N., Douglass, K. M., Gönczy, P., and Manley, S. (2018). Multicolor single-particle reconstruction of protein complexes. *Nature Methods 2018 15:10*, 15(10):777–780.

Smirnov, V. N. I. (1939). On the estimation of the discrepancy between empirical curves of distribution for two independent samples. *Bull. Math. Univ. Moscou*, 2(2):3–14.

Smolikov, S., Eizinger, A., Schild-Prufert, K., Hurlburt, A., McDonald, K., Engebrecht, J. A., Villeneuve, A. M., and Colaiácovo, M. P. (2007). SYP-3 restricts synaptonemal complex assembly to bridge paired chromosome axes during meiosis in *Caenorhabditis elegans*. *Genetics*, 176:2015–2025.

Smolikov, S., Schild-Prüfert, K., and Colaiácovo, M. P. (2009). A yeast two-hybrid screen for SYP-3 interactors identifies SYP-4, a component required for synaptonemal complex assembly and chiasma Formation in *Caenorhabditis elegans* meiosis. *PLoS Genetics*, 5(10):e1000669.

Snowden, T., Acharya, S., Butz, C., Berardini, M., and Fishel, R. (2004). hmsh4-hmsh5 recognizes holliday junctions and forms a meiosis-specific sliding clamp that embraces homologous chromosomes. *Molecular cell*, 15(3):437–451.

Stehr, F., Stein, J., Schueder, F., Schwille, P., and Jungmann, R. (2019). Flat-top TIRF illumination boosts DNA-PAINT imaging and quantification. *Nature Communications 2019 10:1*, 10:1–8.

Stringer, C., Wang, T., Michaelos, M., and Pachitariu, M. (2020). Cellpose: a generalist algorithm for cellular segmentation. *Nature Methods 2020 18:1*, 18(1):100–106.

Sturtevant, A. H. (1913). The linear arrangement of six sex-linked factors in *Drosophila*, as shown by their mode of association. *Journal of Experimental Zoology*, 14(1):43–59.

Sulston, J. and Hodgkin, J. (1988). Methods. In Wood, W. B. and the Community of *C. elegans*

Researchers, editors, *The Nematode Caenorhabditis elegans*, page 587. Cold Spring Harbor Laboratory, New York.

Sym, M., Engebrecht, J., and Roeder, G. (1993). Zip1 is a synaptonemal complex protein required for meiotic chromosome synapsis. *Cell*, 72(3):365–378.

Sym, M. and Roeder, G. S. (1994). Crossover interference is abolished in the absence of a synaptonemal complex protein. *Cell*, 79(2):283–292.

Sym, M. and Roeder, G. S. (1995). Zip1-induced changes in synaptonemal complex structure and polycomplex assembly. *The Journal of Cell Biology*, 128:455.

Szostak, J. W., Orr-Weaver, T. L., Rothstein, R. J., and Stahl, F. W. (1983). The double-strand-break repair model for recombination. *Cell*, 33(1):25–35.

The *pandas* development team (2020). pandas-dev/pandas: Pandas.

Thevathasan, J. V., Kahnwald, M., Cieśliński, K., Hoess, P., Peneti, S. K., Reitberger, M., Heid, D., Kasuba, K. C., Hoerner, S. J., Li, Y., Wu, Y. L., Mund, M., Matti, U., Pereira, P. M., Henriques, R., Nijmeijer, B., Kueblbeck, M., Sabinina, V. J., Ellenberg, J., and Ries, J. (2019). Nuclear pores as versatile reference standards for quantitative superresolution microscopy. *Nature Methods*, 16(10):1045–1053.

Tinevez, J. Y., Perry, N., Schindelin, J., Hoopes, G. M., Reynolds, G. D., Laplantine, E., Bednarek, S. Y., Shorte, S. L., and Eliceiri, K. W. (2017). TrackMate: An open and extensible platform for single-particle tracking. *Methods*, 115:80–90.

Tung, K. S. and Roeder, G. S. (1998). Meiotic chromosome morphology and behavior in *zip1* mutants of *Saccharomyces cerevisiae*. *Genetics*, 149(2):817–832.

Ur, S. N. and Corbett, K. D. (2021). Architecture and dynamics of meiotic chromosomes. *Annual Review of Genetics*, 55(1):497–526. PMID: 34530636.

van der Walt, S., Schönberger, J. L., Nunez-Iglesias, J., Boulogne, F., Warner, J. D., Yager, N., Gouillart, E., Yu, T., and the scikit-image contributors (2014). *scikit-image*: Image processing in Python. *PeerJ*, 2:e453.

Van Rossum, G. and Drake, F. L. (2009). *Python 3 Reference Manual*. CreateSpace, Scotts Valley, CA.

Virtanen, P., Gommers, R., Oliphant, T. E., Haberland, M., Reddy, T., Cournapeau, D., Burovski, E., Peterson, P., Weckesser, W., Bright, J., van der Walt, S. J., Brett, M., Wilson, J., Millman, K. J., Mayorov, N., Nelson, A. R. J., Jones, E., Kern, R., Larson, E., Carey, C. J., Polat, İ., Feng, Y., Moore, E. W., VanderPlas, J., Laxalde, D., Perktold, J., Cimrman, R., Henriksen, I., Quintero, E. A., Harris, C. R., Archibald, A. M., Ribeiro, A. H., Pedregosa, F., van Mulbregt, P., and SciPy 1.0 Contributors (2020). *SciPy* 1.0: Fundamental algorithms for scientific computing in Python. *Nature Methods*, 17:261–272.

Voelkel-Meiman, K., Johnston, C., Thappeta, Y., Subramanian, V. V., Hochwagen, A., and MacQueen, A. J. (2015). Separable crossover-promoting and crossover-constraining aspects of Zip1 activity during budding yeast meiosis. *PLoS genetics*, 11(6):e1005335.

Wang, K., Wang, C., Liu, Q., Liu, W., and Fu, Y. (2015). Increasing the genetic recombination frequency by partial loss of function of the synaptonemal complex in rice.

Wang, Y., Schnitzbauer, J., Hu, Z., Li, X., Cheng, Y., Huang, Z.-L., and Huang, B. (2014). Localization events-based sample drift correction for localization microscopy with redundant cross-correlation algorithm. *Optics Express*, 22(13):15982.

Wickham, H. (2007). Reshaping data with the *reshape* package. *Journal of Statistical Software*, 21(12):1–20.

Wickham, H. (2016). *ggplot2: Elegant Graphics for Data Analysis*. Springer-Verlag New York.

Wickham, H., Averick, M., Bryan, J., Chang, W., McGowan, L. D., François, R., Grolemund, G., Hayes, A., Henry, L., Hester, J., Kuhn, M., Pedersen, T. L., Miller, E., Bache, S. M., Müller, K., Ooms, J.,

Robinson, D., Seidel, D. P., Spinu, V., Takahashi, K., Vaughan, D., Wilke, C., Woo, K., and Yutani, H. (2019). Welcome to the *tidyverse*. *Journal of Open Source Software*, 4(43):1686.

Wickham, H., François, R., Henry, L., Müller, K., and Vaughan, D. (2023). *dplyr: A grammar of data manipulation*. https://dplyr.tidyverse.org, https://github.com/tidyverse/dplyr.

Winterflood, C., Platonova, E., Albrecht, D., and Ewers, H. (2015). Dual-color 3D superresolution microscopy by combined spectral-demixing and biplane imaging. *Biophysical Journal*, 109(1):3–6.

Woglar, A. and Villeneuve, A. M. (2018). Dynamic architecture of DNA repair complexes and the synaptonemal complex at sites of meiotic recombination. *Cell*, 173(7):1678–1691.e16.

Woglar, A., Yamaya, K., Roelens, B., Boettiger, A., Köhler, S., and Villeneuve, A. M. (2020). Quantitative cytogenetics reveals molecular stoichiometry and longitudinal organization of meiotic chromosome axes and loops. *PLoS biology*, 18(8).

Wu, Y. L., Hoess, P., Tschanz, A., Matti, U., Mund, M., and Ries, J. (2022). Maximum-likelihood model fitting for quantitative analysis of SMLM data. *Nature Methods 2022 20:1*, 20:139–148.

Xu, H., Tong, Z., Ye, Q., Sun, T., Hong, Z., Zhang, L., Bortnick, A., Cho, S., Beuzer, P., Axelrod, J., Hu, Q., Wang, M., Evans, S. M., Murre, C., Lu, L. F., Sun, S., Corbett, K. D., and Cang, H. (2019). Molecular organization of mammalian meiotic chromosome axis revealed by expansion STORM microscopy. *Proceedings of the National Academy of Sciences of the United States of America*, 116(37):18423–18428.

Xu, K., Shim, S.-H., and Zhuang, X. (2013). *Super-resolution imaging through stochastic switching and localization of single molecules: An overview*, pages 27–64. Springer Berlin Heidelberg, Berlin, Heidelberg.

Yokoo, R., Zawadzki, K. A., Nabeshima, K., Drake, M., Arur, S., and Villeneuve, A. M. (2012). COSA-1 reveals robust homeostasis and separable licensing and reinforcement steps governing meiotic crossovers. *Cell*, 149(1):75–87.

Yoon, S., Choi, E. H., Kim, J. W., and Kim, K. P. (2018). Structured illumination microscopy imaging reveals localization of replication protein A between chromosome lateral elements during mammalian meiosis. *Experimental Molecular Medicine 2018 50:8*, 50(8):1–12.

Zetka, M. C., Kawasaki, I., Strome, S., and Müller, F. (1999). Synapsis and chiasma formation in *Caenorhabditis elegans* require HIM-3, a meiotic chromosome core component that functions in chromosome segregation. *Genes and Development*, 13(17):2258–2270.

Zhang, L., Köhler, S., Rillo-Bohn, R., and Dernburg, A. F. (2018). A compartmentalized signaling network mediates crossover control in meiosis. *eLife*, 7.

Zhang, L., Liang, Z., Hutchinson, J., and Kleckner, N. (2014). Crossover patterning by the beam-film model: Analysis and implications. *PLoS Genet*, 10(1):1004042.

Zhang, L., Stauffer, W., Zwicker, D., and Dernburg, A. F. (2021). Crossover patterning through kinase-regulated condensation and coarsening of recombination nodules. *bioRxiv*, page 2021.08.26.457865.

Zhang, L., Stauffer, W. T., Wang, J. S., Wu, F., Yu, Z., Liu, C., Kim, H. J., and Dernburg, A. F. (2023). Recruitment of polo-like kinase couples synapsis to meiotic progression via inactivation of CHK-2. *eLife*, 12:e84492.

Zhang, Z., Xie, S., Wang, R., Guo, S., Zhao, Q., Nie, H., Liu, Y., Zhang, F., Chen, M., Liu, L., Meng, X., Liu, M., Zhao, L., Colaiácovo, M. P., Zhou, J., and Gao, J. (2020). Multivalent weak interactions between assembly units drive synaptonemal complex formation. *Journal of Cell Biology*, 219(5).

Zickler, D. and Kleckner, N. (1999). Meiotic chromosomes: Integrating structure and function. *Annual Review of Genetics*, 33(1):603–754.

Zickler, D. and Kleckner, N. (2015). Recombination, pairing, and synapsis of homologs during meiosis. *Cold Spring Harbor perspectives in biology*, 7(6).

Zickler, D., Moreau, P. J., Huynh, A. D., and Slezec, A. M. (1992). Correlation between pairing initiation sites, recombination nodules and meiotic recombination in Sordaria macrospora. *Genetics*, 132(1):135–148.

Zwettler, F. U., Spindler, M. C., Reinhard, S., Klein, T., Kurz, A., Benavente, R., and Sauer, M. (2020). Tracking down the molecular architecture of the synaptonemal complex by expansion microscopy. *Nature Communications 2020 11:1*, 11(1):1–11.

Appendix A. *Caenorhabditis elegans* strains used in this study

Table A.1. *Caenorhabditis elegans* strains used in the study

Strain ID	Strain	Source
N2	wild-type isolate, Bristol	CGC
MT21793	*gur-3*(*ok2245*) X; *lite-1*(*ce314*) X	CGC; Bhatla and Horvitz 2015
YKM348	*syp-5*(*kim8*[*ha::syp-5*]) I; *meIs8*[*pie-1p::GFP::cosa-1*, *unc-119*(+)] II	Hurlock et al. 2020
YKM349	*syp-5*(*kim9*[*syp-5::ha*]) I; *meIs8*[*pie-1p::GFP::cosa-1*, *unc-119*(+)] II	Hurlock et al. 2020
YKM350	*syp-6*(*kim10*[*ha::syp-6*]) I; *meIs8*[*pie-1p::GFP::cosa-1*, *unc-119*(+)] II	Hurlock et al. 2020
YKM351	*syp-6*(*kim11*[*syp-6::ha*]) I; *meIs8*[*pie-1p::GFP::cosa-1*, *unc-119*(+)] II	Hurlock et al. 2020
YKM219	*skr-2*(*kim65*[*skr-2::3xFlag*]) I; *meIs8*[*pie-1p::GFP::cosa-1*, *unc-119*(+)] II	Blundon et al. 2023
YKM217	*skr-1*(*kim67*[*ha::skr-1*]) I	Blundon et al. 2023
SMN256	*cosa-1*(*ske25*[*HaloTag::cosa-1*]) III; *syp-1*(*ske17*[*syp-1::mNeonGreen*]) V; *gur-3*(*ok2245*) X; *lite -1*(*ce314*) X	This study by E. Berna Durmus
SMN260	*cosa-1*(*ske25*[*HaloTag::cosa-1*]) III	Köhler lab by Simone Köhler
SMN73	*skeSi1*[*sun-1p::UTR230::GFP::3xNLS + Cbr-unc-119* (+)]) II; *rad-51*(*ske1*[*ha::rad-51*]) IV	Köhler lab by Simone Köhler
NA	*skeSi1*[*sun-1p::UTR230::GFP::3xNLS + Cbr-unc-119* (+)] II; *rad-51*(*ske48*[*V5::rad-51*]) IV	This study by me
SMN349	*rad-51*(*ske48*[*v5::rad-51*]) IV	This study by me
SMN350	*cosa-1*(*ske25*[*HaloTag::cosa-1*]) III;; *rad-51*(*ske48*[*v5::rad-51*]) IV	This study by me
SMN351	*htp-3*(*ske16-1*[*htp-3::ha*]) I; *cosa-1*(*ske25*[*HaloTag::cosa-1*]) III; *rad-51*(*ske48*[*v5::rad-51*]) IV	This study by me
SMN348	*zhp-3*(*ie115*[*zhp-3::v5*]) I; *htp-3*(*ske16-1*[*htp-3::ha*]) I; *cosa-1*(*ske25*[*HaloTag::cosa-1*]) III	This study by me and Simone Köhler (*ie115* allele)

Table A.1 – *Continued on the next page*

Table A.1 – *Continued from the previous page*

Strain ID	Strain	Source
SMN407	*syp-1*(*ske17*[*syp-1::mNeonGreen*]) V; *gur-3*(*ok2245*) X	This study by Cristina Pineiro Lopez and E. Berna Durmus
SMN408	*htp-3*(*ske16-1*[*htp-3::ha*]) I; *cosa-1*(*ske45*[*alfa::cosa-1*]) III	This study by me
SMN452	*cosa-1*(*ske21*[*cosa1::mNeonGreen*]) III; *him-3*(*ske31*[*halo::him-3*]) IV; *gur-3*(*ok2245*) X; *lite -1*(*ce314*) X	This study by Cristina Pineiro Lopez, Lauren M. Sloat, and me
SMN453	*msh-5*(*ske50*[*msh-5::HaloTag9*]) IV; *syp-1*(*ske17*[*syp-1::mNeonGreen*]) V; *gur-3*(*ok2245*) X; *lite -1*(*ce314*) X	This study by Cristina Pineiro Lopez, Lauren M. Sloat, and me
SMN175	*meIs8*[*pie-1p::GFP::cosa-1*, *unc-119*(+)] II; *syp-1*(*ske18*[*syp-1::ha*]) V	This study by me and Simone Köhler
SMN73	*zhp-3*(*ie115*[*zhp-3::v5*]) I	Köhler lab by Simone Köhler
SMN437	*msh-5*(*ske50*[*msh-5::HaloTag9*]) IV; *syp-1*(*ske17*[*syp-1::mNeonGreen*]) V; *gur-3*(*ok2245*) X	This study by me and Lauren M. Sloat
SMN288	*htp-3*(*ske16-1*[*htp-3::ha*]) I; *msh-5*(*ske49*[*msh-5::V5*]) IV	This study by me
SMN290	*htp-3*(*ske16-1*[*htp-3::ha*]) I; *msh-5*(*ske52*[*V5::msh-5*]) IV	This study by me
SMN326	*htp-3*(*ske16-1*[*htp-3::ha*]) I; *cosa-1*(*ske25*[*HaloTag::cosa-1*]) III; *him-6*(*ske51*[*him-6::V5*]) IV	This study by me
SMN324	*htp-3*(*ske16-1*[*htp-3::ha*]) I; *cosa-1*(*ske25*[*HaloTag::cosa-1*]) III; *msh-5*(*ske49*[*msh-5::V5*]) IV; *rec -8(ske54*[*rec-8::ollas*]) IV	This study by me
SMN311	*htp-3*(*ske16-1*[*htp-3::ha*]) I; *cosa-1*(*ske25*[*HaloTag::cosa-1*]) III; *msh-5*(*ske49*[*msh-5::V5*]) IV	This study by me
SMN310	*htp-3*(*ske16-1*[*htp-3::ha*]) I; *cosa-1*(*ske25*[*HaloTag::cosa-1*]) III; *msh-5*(*ske52*[*V5::msh-5*]) IV	This study by me

Appendix B. Specifics of CRISPR/Cas9-mediated genome editing

This appendix provides the list of all alleles generated in this study (**Table B.1**), together with additional information about the repair templates (**Table B.2**), and the sequences of the CRISR-RNAs (crRNA), genotyping information, and sequencing PCR primers (**Table B.3**).

Table B.1. Alleles generated for this study by CRISPR/Cas9-mediated genome editing

Allele	Genotype	Strain	Strain ID	Generated by
ske49	*msh-5::V5*	*htp-3*(*ske16-1*[*htp-3::ha*]) I; *msh-5*(*ske49*[*msh-5::V5*]) IV	SMN288	me
ske52	*V5::msh-5*	*htp-3*(*ske16-1*[*htp-3::ha*]) I; *msh-5*(*ske52*[*V5::msh-5*]) IV	SMN290	me
ske51	*him-6::V5*	*htp-3*(*ske16-1*[*htp-3::ha*]) I; *cosa-1*(*ske25*[*HaloTag::cosa-1*]) III; *him-6*(*ske51*[*him-6::V5*]) IV	SMN326	me
ske48	*V5::rad-51*	*skeSi1*[*sun-1p::UTR230::GFP::3xNLS* + *Cbr-unc-119* (+)] IV; *rad-51*(*ske48*[*V5::rad-51*]) IV	NA	me
ske50	*msh-5::HaloTag9*	*msh-5*(*ske50*[*msh-5::HaloTag9*]) IV; *syp-1*(*ske17*[*syp-1::mNeonGreen*]) V; *gur-3*(*ok2245*) X	SMN437	me and Lauren M. Sloat
ske54	*rec-8::olla*s	*htp-3*(*ske16-1*[*htp-3::ha*]) I; *cosa-1*(*ske25*[*HaloTag::cosa-1*]) III; *msh-5*(*ske49*[*msh-5::V5*]) IV; *rec-8*(ske54[rec-8::ollas]) IV	SMN324	me
ske45	*alfa::cosa-1*	*htp-3*(*ske16-1*[*htp-3::ha*]) I; *cosa-1*(*ske45*[*alfa::cosa-1*]) III	SMN408	me
ske18	*syp-1::ha*	*meIs8*[*pie-1p::GFP::cosa-1*, *unc-119(+)*] II; *syp-1*(*ske18*[*syp-1::ha*]) V	SMN175	me and Simone Köhler

Table B.2. Repair templates for CRISPR/Cas9-mediated genome editing

Allele (genotype)	Repair template sequence	Description
***ske49* (*msh-5::V5*)**	5'-ggaagatgatgagttcttgaagagtttccttgaaacagaaggatctctacatattgacacaagcgcc-gatgagacgatagatcgttcgaaaagaagtggaaagccaatcccaaacccacttcttggactcgactc-cacctaattttatataattagaatttcgtatttcttgtaatgttcaatcttgttcaatgtatttcgttttcgtttttaaat-tatttatagcgcatttttaataaatactatttttttaaaactcgtgcaatagttcacaacgaagtttaactgcgatttttt-tacaaaaaatacagatttttttggttttcaaaagtagctgatctgcaattattgcactttctgaaagtatcgaat-taatgaatgcaacaagaagttccagacgcgcacttttgcaattcttgcgcgaaatatactgtacccgggc-3'	Initial gBlock ordered from the IDT was cloned into pMiniT 2.0 (NEB® PCR Cloning Kit, E1202S, New England Biolabs, Inc.). Injected template (final concentration **62 ng/µl**) was generated by a PCR using high-fidelity DNA polymerase (Q5® High-Fidelity DNA Polymerase, M0491S, New England Biolabs, Inc.) and following primers: F: 5'-ggaagatgatgagttcttgaaga-3'; R: 5'-gcccgggtacagtatatttc-3'
***ske52* (*V5::msh-5*)**	5'-cttaaatcagaaataattttatgaaattttggttcaaatgggaaagccaatcccaaacccacttcttg-gactcgactccaccagtacaagatggagatattacaattcaaaacgcgggaatggattccgcggtcg-3'	Ordered from IDT as Ultramer™ dsDNA oligonucleotide and directly used for injection at final concentration of **5 µM**
***ske51* (*him-6::V5*)**	5'-Btn-ccagctacttcactcaaacggaacatgtatccagccacaagtatgggaaagccaatcc-caaacccacttcttggactcgactccacctaaaagattgctatgaatagtaactattgaatt-3'	Ordered from Sigma-Aldrich/Merk as dsDNA oligonucleotide and directly used for injection at final concentration of **5 µM**
***ske48* (*V5::rad-51*)**	5'-cttaaaaataattaattaaaattatctcaggagtcaaaaatgggaaagccaatcccaaacc-cacttcttggactcgactccacctcagcacaagcaagtcgtcaaaagaaatcggatcaa-3'	Ordered from Sigma-Aldrich/Merk as dsDNA oligonucleotide and directly used for injection at final concentration of **5 µM**
***ske45* (*alfa::cosa-1*)**	5'-tgaaaaatcgtgaaaactgaactgaagtgtcaatgtcccgtctcgaggaggagctccgtcgtcgtct-caccgagggaggaggaagttcttcacggtgagttgtcgtttcaaaataaaatg-3'	Ordered from Sigma-Aldrich/Merk as dsDNA oligonucleotide and directly used for injection at final concentration of **5 µM**
***ske18* (*syp-1::ha*)**	5'-cgagagccgaagctcatactgcagatgttcgcaggaaacgcgggggaaaaaagtacccctacgat-gtcccagattatgcttaatgtgtgtgtggggaagaaacgactatgtaccatttc-3'	Ordered from Sigma-Aldrich/Merk as dsDNA oligonucleotide and directly used for injection at final concentration of **5 µM**
***ske54* (*rec-8::ollas*)**	5'-gaagcgaagcaagaagatccttattttccaattctagtacgtcacatcagtcacgaagaaatgtccg-gattcgctaacgagcttggaccacgccttatgggaaagtgaagctgctaatataattgatactgtatcatttc-ccaatttttcatagcttc-3'	Ordered from IDT as Ultramer™ DNA Oligonucleotide and directly used for injection at final concentration of **5 µM**

Table B.2 – *Continued on the next page*

Table B.2 – *Continued from the previous page*

Allele (genotype)	Repair template sequence	Description
ske50 **(*msh-5::HaloTag9*)**	5’-ggaagatgatgagttcttgaagagtttccttgaaacagaaggatctctacatattgacacaagcgcc-gatgagacgatagatcgttcgaaaagaagtggagctggaatcggaaccggattcccattcgaccca-cactacgtcgaggtccttggagagcgcatgcactacgtcgacgtcggaccacgcgacggaacc-ccagtccttttccttcacggaaacccaacctcctcctacgtctggcgcaacatcatcccacacgtcgccc-caacccaccgctgcatcgccccagaccttatcggaatgggaaagtccgacaagccagaccttggat-acttcttcgacgaccacgtccgtttcatggacgccttcatcgaggcccttggacttgaggaggtcgtccttgt-catccacgactggggatccgcccttggattccactgggccaagcgcaacccagagcgcgtcaag-gtaagtttaaacatatatatactaactaaccctgattatttaaattttcagggaatcgccttcatggagttcatc-cgcccaatcccaacctgggacgagtggccagagttcgcccgcgagaccttccaagccttccgcaccac-cgacgtcggacgtaagcttatcatcgaccacaacgtcttcatcgagggaacccttcgtatgggagtcgtc-cgtccacttaccgaggtcgagatggaccactaccgcgagccattccttaacccagtcgaccgcgagc-cactttggcgcttcccaaacgagcttccaatcgccggagagccagccaacatcgtcgcccttgtcgag-gagtacatggactggcttcaccaatccccagtcccaaagcttcttttctggggaaccccaggagtccttatc-ccaccagccgaggccgcccgtcttgccaagtcccttccaaactgcaaggtaagtttaaacagttcggtac-taactaaccatacatatttaaattttcaggccgtcgacatcggaccaggacttaaccttcttcaagagga-caacccagaccttatcggatccgagatcgcccgttggctttccacccttgagatctaattttatataatta-gaatttcgtatttcttgtaatgttcaatcttgttcaatgtatttcgttttcgtttttaaattatttatagcgcattt-taataaatactatttttttaaaactcgtgcaatagttcacaacgaagtttaactgcgatttttttacaaaaaatacа-gatttttttggttttcaaaagtagctgatctgcaattattgcactttctgaaagtatcgaattaatgaatgcaacaa-gaagttccagacgcgcacttttgcaattcttgcgcgaaatatactgtacccgggc-3’	Initial gBlock ordered from the IDT was cloned into pMiniT 2.0 (NEB® PCR Cloning Kit, E1202S, New England Biolabs, Inc.). Injected templete (final concentration **40 ng/µl**) was generated by a PCR using high-fidelity DNA polymerase (Q5® High-Fidelity DNA Polymerase, M0491S, New England Biolabs, Inc.) and following primers: F: 5’-ggaagatgatgagttcttgaaga-3’; R: 5’-gcccgggtacagtatatttc-3’; Before it was added into the injection mixture template was melted according to protocol described in Ghanta and Mello, 2020.

Table B.3. Sequences of CRISPR-RNA (crRNA), genotyping information, and sequencing primers for each CRISPR/Cas9-mediated genome editing

Allele (genotype)	crRNA	Genotyping primers and fragment sizes	Sequencing primers
***ske48* (*msh-5::V5*)**	Two crRNAs were used simultaneously: 5'-catcggcgctcgtatcgata-3' and 5'-tgcgcgtctggaacttcttg-3'	F:5'-gtcaaacgacgatgaggaag-3'; R:5'-cgttgtgaactattgcacgag-3'; WT, 248 bp; Edit, 290 bp	F:5'-gttcgatttccccgagca-3'; R:5'-taccttcacaactcttccatcg-3';
***ske52* (*V5::msh-5*)**	5'-tggttcaaatgtccactcgatgg-3'	F:5'-ggtgttcaatcaacttttttgaag-3'; R:5'-gaaaattatcatcacggggtaag-3'; WT, 269 bp; Edit, 311 bp	F:5'-ggtgttcaatcaacttttttgaag-3'; R:5'-gaaaattatcatcacggggtaag-3';
***ske51* (*him-6::V5*)**	5'-atcttttacatcgatgtagc-3'	F:5'-ggcaaaaccagctacttcac-3'; R:5'-ctttttgagggcaatttccatc-3'; WT, 278 bp; Edit, 320 bp	F:5'-gtgatgggtggtttcgc-3'; R:5'-ctttttgagggcaatttccatc-3';
***ske48* (*V5::rad-51*)**	crRNA targets sequence for HA tag; 5'-cataatctgggacatcgtag-3'	**Set1:** F:5'-gctccactgttaaaaatgccg-3'; R:5'-atatcgccagaactgattcctg-3'; WT, 319 bp; *HA::rad-51*, 346 bp; Edit, 361 bp; **Set2:** F:5'-gctccactgttaaaaatgccg-3'; R:5'-gtcgagtccaagaagtggg-3'; WT, no amplification; *HA::rad-51*, no amplification; Edit, 197 bp; **Set3:** F:5'-gctccactgttaaaaatgccg-3'; R:5'-gcataatctgggacatcgtagg-3' ; WT, no amplification; *HA::rad-51*, 187 bp; Edit, no amplification;	F:5'-gctccactgttaaaaatgccg-3'; R:5'-atatcgccagaactgattcctg-3';

Table B.3 – *Continued on the next page*

Table B.3 – *Continued from the previous page*

Allele (genotype)	crRNA	Genotyping primers and fragment sizes	Sequencing primers
***ske50* (*msh -5::HaloTag9*)**	Two crRNAs were used simultaneously: 5'-catcggcgctcgtatcgata-3'; 5'-tgcgcgtctggaacttcttg-3'	**Set1:** F:5'-gttcgatttccccgagca-3'; R:5'-gggcgatgcagcgg-3'; WT, no amplification; Edit, 474 bp; **Set2:** F:5'-gttcgatttccccgagca-3'; R:5'-cgttgtgaactattgcacgag-3'; WT, 420 bp; Edit, 1407 bp	F:5'-gttcgatttccccgagca-3'; R:5'-taccttcacaactcttccatcg-3'
***ske54* (*rec-8::ollas*)**	5'-agcagcttcacatttcttcg-3'	F:5'-gaaggttgaagcgaagcaagaaga-3'; R:5'-cctcataacagccctagctagagtc-3'; WT, 250 bp; Edit, 292 bp	F:5'-gaaggttgaagcgaagcaagaaga-3'; R:5'-cctcataacagccctagctagagtc-3'
***ske45* (*alfa::cosa-1*)**	5'-aagtgtcaatgtcaagttct-3'	F:5'-gtattggtctcgcaccgaac-3'; R:5'-ctgctgatacggcaggtgta-3'; WT, 280 bp; Edit, 328 bp	F:5'-gtattggtctcgcaccgaac-3'; R:5'-ctgctgatacggcaggtgta-3'
***ske18* (*syp-1::ha*)**	5'-gatgttcgccgaaagagagg-3'	F:5'-cgttgaaacgaactcgtgc-3'; R:5'-ttttctctctcgttgccgc-3'; WT, 198 bp; Edit, 225 bp	F:5'-cgatatcgtggaatccgact-3'; R:5'-ccaatttgtcggggagtttt-3'

Appendix C. Brood counts for the *Caenorhabditis elegans* strains generated in this study

Table C.1. Brood counts for the *Caenorhabditis elegans* strains generated in this study

Strain ID (genotype)	#eggs (worms)	#males	#live progeny	Viability of progeny [%]	*p*-value (significance)[1]	Incidence of males [%]	*p*-value (significance)[2]
N2 (wild-type isolate, Bristol)	1301 (5)	2	1332	102.8		0.14	
SMN260 (*cosa-1*(*ske25*[*HaloTag::cosa-1*]) III)	1548 (6)	8	1612	103.5	0.931 (ns)	0.46	0.025 (*)
SMN326 (*htp-3*(*ske16-1*[*htp-3::ha*]) I; *cosa-1*(*ske25*[*HaloTag::cosa-1*]) III; *him-6*(*ske51*[*him-6::V5*]) IV)	1473 (6)	4	1559	105.9	0.12 (ns)	0.25	0.213 (ns)
SMN311 (*htp-3*(*ske16-1*[*htp-3::ha*]) I; *cosa-1*(*ske25*[*HaloTag::cosa-1*]) III; *msh-5*(*ske49*[*msh-5::V5*]) IV)	1404 (5)	7	1511	107.8	0.052 (ns)	0.46	0.02 (*)
SMN310 (*htp-3*(*ske16-1*[*htp-3::ha*]) I; *cosa-1*(*ske25*[*HaloTag::cosa-1*]) III; *msh-5*(*ske52*[*V5::msh-5*]) IV)	1119 (4)	2	1005	92.9	0.73 (ns)	0.18	0.614 (ns)
SMN256 (*cosa-1*(*ske25*[*HaloTag::cosa-1*]) III; *syp-1*(*ske17*[*syp-1::mNeonGreen*]) V; *gur-3*(*ok2245*) X; *lite-1*(*ce314*) X)	1705 (6)	7	1711	100.6	0.792 (ns)	0.41	0.095 (ns)

[1]Wilcoxon rank rum test using the *ggpubr* R package (version 0.6.0, Kassambara 2023). Statistical significance: ns (p > 0.05), * (p <= 0.05), ** (p <= 0.01).

[2]One-sided Wilcoxon rank rum test using the *ggpubr* R package (version 0.6.0, Kassambara 2023). Statistical significance: ns (p > 0.05), * (p <= 0.05), ** (p <= 0.01).

Appendix D. Reagents used in cytological methods

Listed in this appendix are antibodies, HaloTag ligands, and succinimidyl ester derivatives of organic fluorophores (**Table D.1**) and the specifics on how these reagents were used in each experiment of this study (**Table D.2**).

Table D.1. Reagents used for flourescent staining in the cytological experiments

Reagent type	Reagent	Company/Source	Catalog number/ Reference	Description	Dilution
Primary antibody	anti-HA(Ms)	Thermo Fisher Scientific	2-2.2.14	Mouse monoclonal	Listed in Table D.2.
	anti-HA(Gt)	Thermo Fisher Scientific	A190-138A	Goat polyclonal	Listed in Table D.2.
	anti-HIM-3	Novus Biologicals	#53470002	Rabbit polyclonal	Listed in Table D.2.
	anti-HTP-3	a gift from Abby F. Dernburg	MacQueen et al., 2005	Chicken polyclonal	Listed in Table D.2.
	anti-Flag	Merk/Sigma-Aldrich	F1804-50UG	Mouse monoclonal	Listed in Table D.2.
	anti-V5	Thermo Fisher Scientific	R960-25	Mouse monoclonal	Listed in Table D.2.

Table D.1 – *Continued on the next page*

Table D.1 -- *Continued from the previous page*

Reagent type	Reagent	Company/Source	Catalog number/ Reference	Description	Dilution
Secondary antibody	AlexaFluor488-anti-goat IgG	Invitrogen	A-11001	Donkey polyclonal	Listed in Table D.2.
	CF680-anti-goat IgG	Biotium	20060-1	Donkey polyclonal	Listed in Table D.2.
	AlexaFluor647-anti-mouse IgG	Jackson Immuno Research	AB_2340863	Donkey polyclonal	Listed in Table D.2.
	CF680-anti-rabbit IgG	Merk/Sigma-Aldrich	SAB4600362-125UL	Goat polyclonal F(ab')2 fragment	Listed in Table D.2.
	F(ab')2 fragment anti-chicken IgY	Jackson Immunoresearch	AB_2340347	Donkey polyclonal	Listed in Table D.2.
	F(ab')2 fragment anti-goat IgG	Jackson Immunoresearch	AB_2340386	Donkey polyclonal	Listed in Table D.2.
	F(ab')2 fragment anti-mouse IgG	Jackson Immunoresearch	AB_2340761	Donkey polyclonal	Listed in Table D.2.
	F(ab')2 fragment anti-rabbit IgG	Jackson Immunoresearch	AB_2340586	Donkey polyclonal	Listed in Table D.2.
Succinimidyl (NHS) ester dye derivatives	AlexaFluor 594, NHS ester	ThermoFischer Scientific	A37572	Dissolved in DMSO to 1 mM solution	not applicable
	AlexaFluor 647, NHS ester	ThermoFischer Scientific	A37573	Dissolved in DMSO to 1 mM solution	not applicable
	CF680, NHS ester	Biotium	92139	Dissolved in DMSO to 1mM solution	not applicable
	STAR 635P, NHS ester	Abberior	ST635P-0002-1MG	Dissolved in DMSO to 1 mM solution	not applicable
	CF660C, NHS ester	Biotium	92137	Dissolved in DMSO to 1 mM solution	not applicable

Table D.1 – *Continued on the next page*

Table D.1 -- *Continued from the previous page*

Reagent type	Reagent	Company/Source	Catalog number/ Reference	Description	Dilution
HaloTag ligands	JaneliaFluor 503	a gift from Luke Lavis	Grimm et al. 2015	Dissolved in DMSO to 1 mM solution	1:200 or 1:100
	JaneliaFluor 639	a gift from Luke Lavis	Deo et al. 2021	Dissolved in DMSO to 1 mM solution	1:100
	JaneliaFluor 669	a gift from Luke Lavis	Grimm et al. 2015	Dissolved in DMSO to 1 mM solution	1:100
Nanobody	FluoTag®-X2 anti-ALFA	NanoBioTech	N1502		Listed in Table D.2.
	FluoTag®-X4 anti-GFP	NanoBioTech	N0304-AF647-L		Listed in Table D.2.

Table D.2. Specifics of the cytological experiments

Strain	Primary antibodies	Secondary antibodies	HaloTag ligand	Figure	Microscope	Acquisition details
YKM349	1:250 anti-HA(Ms) and anti-HTP-3	1:100 AlexaFluor 647 -F(ab')2-anti-mouse IgG and CF680-F(ab')2-anti -chicken IgY	none	4.2,4.1	SMLM at EMBL Imaging Centre	200,000 frames, exposure time of 20 ms, laser power densities of approx. 20 kW/cm2, UV activation laser at a 3 kW/cm2 in rising mode
YKM349	1:1,000 anti-HA(Ms) and anti-HTP-3	1:1,000 STAR 635P-F(ab')2 -anti-mouse IgG and AlexaFluor 594-F(ab')2-anti -chicken IgY	none	4.3	Leica Stellaris 8 STED FALCON	Described in section 3.4.6
YKM348-351	1:200 anti-HA(Ms) and 1:200 or 1:100 anti-HIM-3	1:1,000 or 1:500 AlexaFluor647-anti-mouse IgG and CF680-anti-rabbit IgG	none	4.4, F.1	SMLM from Ries group	100,000–150,000 frames, exposure time of 15 ms, laser power densities ~6 kW/cm2

Table D.2 – *Continued on the next page*

Table D.2 – *Continued from the previous page*

Strain	Primary antibodies	Secondary antibodies	HaloTag ligand	Figure	Microscope	Acquisition details
YKM219	1:200 anti-Flag and 1:200 or 1:100 anti -HIM-3	1:50 AlexaFluor 647-F(ab')2 -anti-mouse IgG and CF680 -F(ab')2-anti-rabbit IgG	none	4.6	SMLM from Ries group	200,000 frames, exposure time of 20 ms, laser power densities of 13 -20 kW/cm2, UV activation laser at a 2 kW/cm2 in rising mode
YKM217	1:200 anti-HA(Ms) and anti-HTP-3	1:50 AlexaFluor 647-F(ab')2 -anti-mouse IgG and CF680 -F(ab')2-anti-chicken IgY	none	4.5	SMLM from Ries group	200,000 frames, exposure time of 20 ms, laser power densities of 13 -20 kW/cm2, UV activation laser at a 2 kW/cm2 in rising mode
SMN311	1:200 anti-V5, anti -HA(Gt)	1:50 AlexaFluor 647-F(ab')2 -anti-mouse IgG and CF660C/ CF680-F(ab')2 -anti-goat IgG	JF503	5.9, 5.10. 5.12, G.5	SMLM at EMBL Imaging Centre	250,000-300,000 frames, exposure time of 20-30 ms, laser power densities of 13-20 kW/cm2
SMN311	1:1000 anti-V5, anti -HA(Gt)	1:1000 AlexaFluor647-anti -mouse IgG and AlexaFluor488-anti-goat IgG	none	5.9	Olympus IXplore SpinSR	Described in section 3.4.5

Appendix E. Single molecule localisation microscopes used in this study

Table E.1. Single molecule localisation microscopes used in this study

Microscope	Objective	References	Figures
SMLM Ries Group	Leica 160X (NA 1.43)	Deschamps et al. 2016; Mund et al. 2018, also used in Hurlock et al. 2020	4.4, 5.11, F.1
SMLM Ries Group	Leica 160X (NA 1.43)	Deschamps et al. 2016; Deschamps and Ries 2020; Deschamps et al. 2023; Mund et al. 2018, 2023; Schröder et al. 2020; Diekmann et al. 2020, also used in Blundon et al. 2023	4.5, 4.6
SMLM EMBL Imaging Centre	UPLAPO100XOHR (NA 1.5)	Diekmann et al. 2020 with modifications, Stehr et al. 2019 (homogeneous laser illumination), also used in Čavka et al. 2022	4.1,4.2
SMLM EMBL Imaging Centre	UPLSAPO100XS (NA 1.35)	Diekmann et al. 2020 with modifications, Stehr et al. 2019 (homogeneous laser illumination)	5.9B, 5.10C-D, 5.12, G.5

Appendix F. Supplementary information for section 4.2

Table F.1. Number and total length of the stretches that were analyzed to map the orientation of SYP-5 and SYP-6. Modified from Hurlock et al. 2020.

Strain	No. of stretches analysed	Total length analysed [nm]
YKM348 (*syp-5*(*kim8*[*HA::syp-5*]) I; *meIs8*[*pie-1p::GFP::cosa-1*, *unc-119*(+)] II)	24	4271
YKM349 (*syp-5*(*kim9*[*syp-5::HA*]) I; *meIs8*[*pie-1p::GFP::cosa-1*, *unc-119*(+)] II)	18	4106
YKM350 (*syp-6*(*kim10*[*HA::syp-6*]) I; *meIs8*[*pie-1p::GFP::cosa-1*, *unc-119*(+)] II)	22	4667
YKM351 (*syp-6*(*kim11*[*syp-6::HA*]) I; *meIs8*[*pie-1p::GFP::cosa-1*, *unc-119*(+)] II)	23	4649

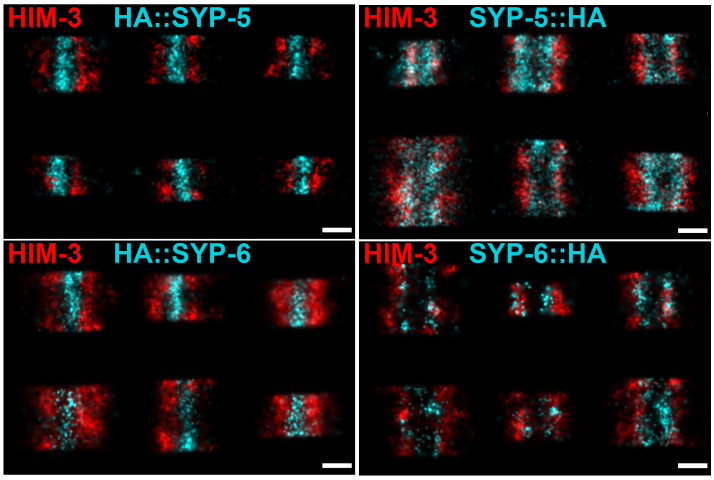


Figure F.1. Examples of individual stretches taken from SMLM images for mapping position and orientation of SYP-5/6 proteins

Scale bar, 100 nm. Modified from Hurlock et al. 2020.

Table F.2. Distribution parameters of the HA::SYP-5/6 and SYP-5/6::HA localisations in frontal (*x*-axis) and cross-sectional view (*z*-axis) with standard deviations obtained by a bootstrapping approach (Köhler et al., 2017). The distance between two localisation peaks is marked by *d*, while the distance from the center of the synaptonemal complex is marked by d/2. ”-” indicates that unimodal distributions were fitted. The width of the distributions is given by the half-width at half maximum of the fitted Gaussian distributions (HWHM). Adapted from Hurlock et al. 2020.

	***x*-axis**			***z*-axis**
Protein	***d***	***d/2***	**HWHM [nm]**	**HWHM [nm]**
HA::SYP-5	-	-	24.0 ± 0.9	43.7 ± 1.7
SYP-5::HA	84	41.6 ± 1.1	27.6 ± 0.8	48.9 ± 2.3
HA::SYP-6	-	-	24.7 ± 1.6	42.5 ± 1.2
SYP-6::HA	84	42.3 ± 1.2	23.5 ± 0.9	45.7 ± 2.1
HIM-3	126	63.3 ± 1.1	33.9 ± 0.8	46.4 ± 1.1
HIM-3 (HA::SYP-5)	120	60.1 ± 2.0	31.9 ± 1.5	42.2 ± 1.7
HIM-3 (SYP-5::HA)	136	68.2 ± 2.4	35.8 ± 1.8	49.3 ± 3.0
HIM-3 (HA::SYP-6)	120	60.4 ± 2.2	35.3 ± 1.5	46.8 ± 1.6
HIM-3 (SYP-6::HA)	128	64.5 ± 1.6	30.6 ± 1.1	47.1 ± 1.8

Appendix G. Supplemental information for chapter 5

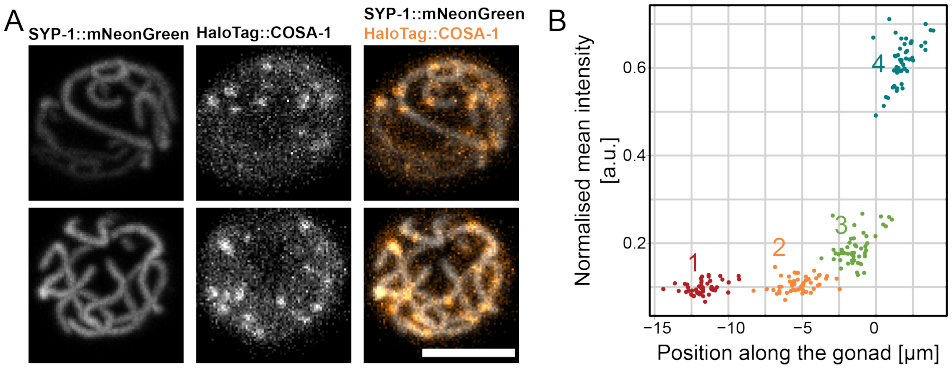


Figure G.1. Supplemental information for Figure 5.1A

(A) Nuclei destined for apoptosis identified within the timelapse movie of *Caenorhabditis elegans* germline. **(B)** Normalized mean HaloTag::COSA-1 foci intensity for four nuclei whose synaptonemal complexes have been traced to study the dynamics of COSA-1 association to the synaptonemal complex. Each point represents normalized mean HaloTag::COSA-1 foci intensity within the nucleus at a given time point of the timelapse movie of *Caenorhabditis elegans* germline.

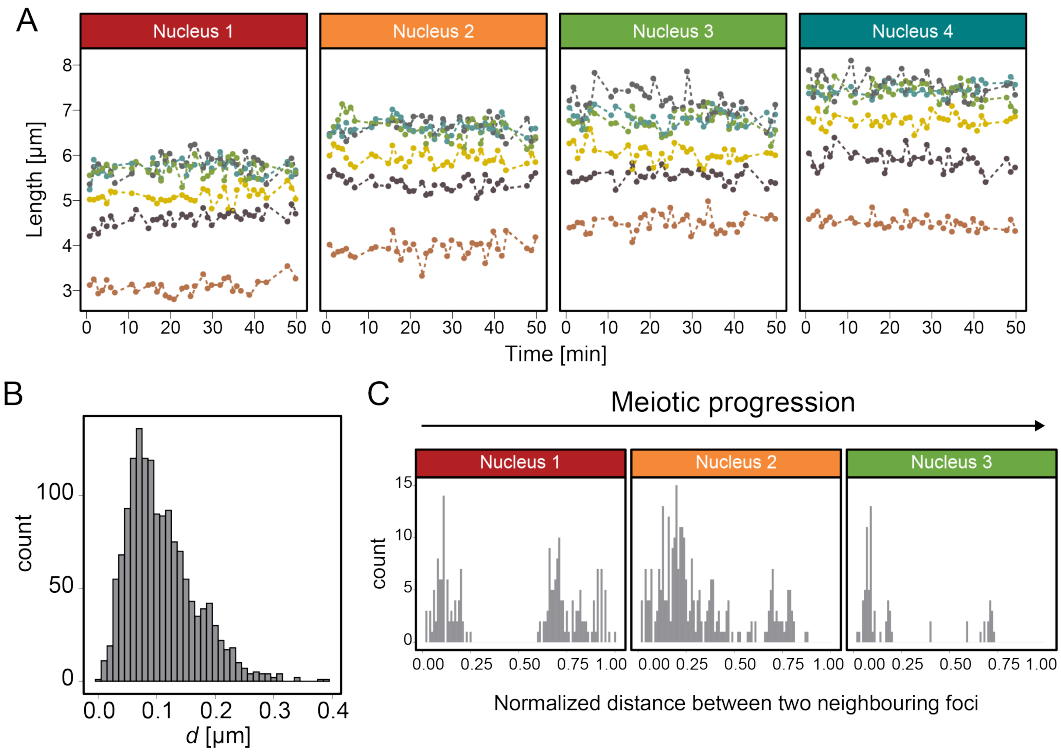


Figure G.2. Characterisation of synaptonemal complex tracing

(A) Length of the processed traces (see section 3.8.4). Different colours of the points and dashed lines denote six different synaptonemal complexes within each nucleus. **(B)** Histograms showing the distribution of the distances between HaloTag::COSA-1 foci identified by spotMAX and its associated foci for all four traced nuclei. **(C)** Histograms showing the distribution of the distances between two neighbouring foci. Different coloured title boxes in A and C denote the four nuclei (**Figure 5.1A**) in which distribution of the HaloTag::COSA-1 signal along the chromosomes has been assessed.

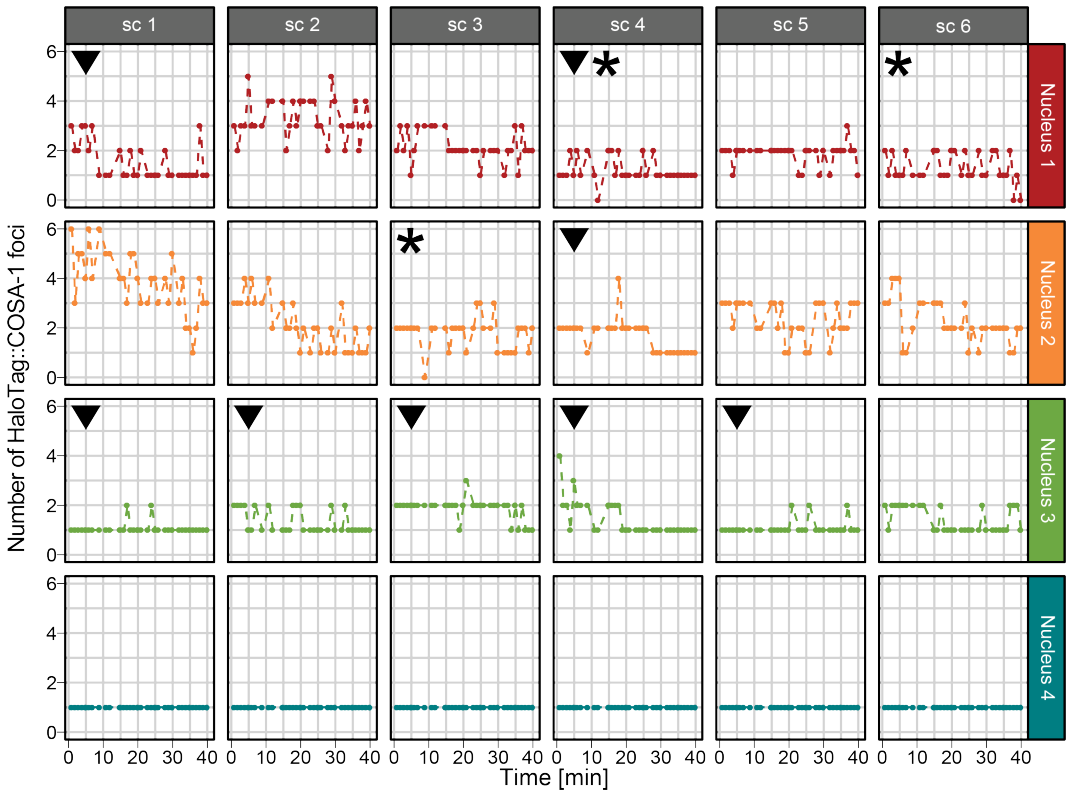


Figure G.3. HaloTag::COSA-1 foci counts for each traced synaptonemal complex

Number of HaloTag::COSA-1 foci associated to each traced synaptonemal complex. The numbering of the synaptonemal complexes relates to their mean length during the timelapse movie, with ”sc 1” marking the longest and ”sc 6” marking the shortest. Different colours denote four different traced nuclei as shown in **Figure 5.1A**. The inverted triangles mark synaptonemal complexes that have a single HaloTag::COSA-1 focus associated with them, and their recreated HaloTag::COSA-1 foci profiles are shown in **Figure 5.7**. The asterisks indicate synaptonemal complexes that, at some point during the timelapse, do not have any foci associated with them. These specific synaptonemal complexes are shown in **Figure G.4B**.

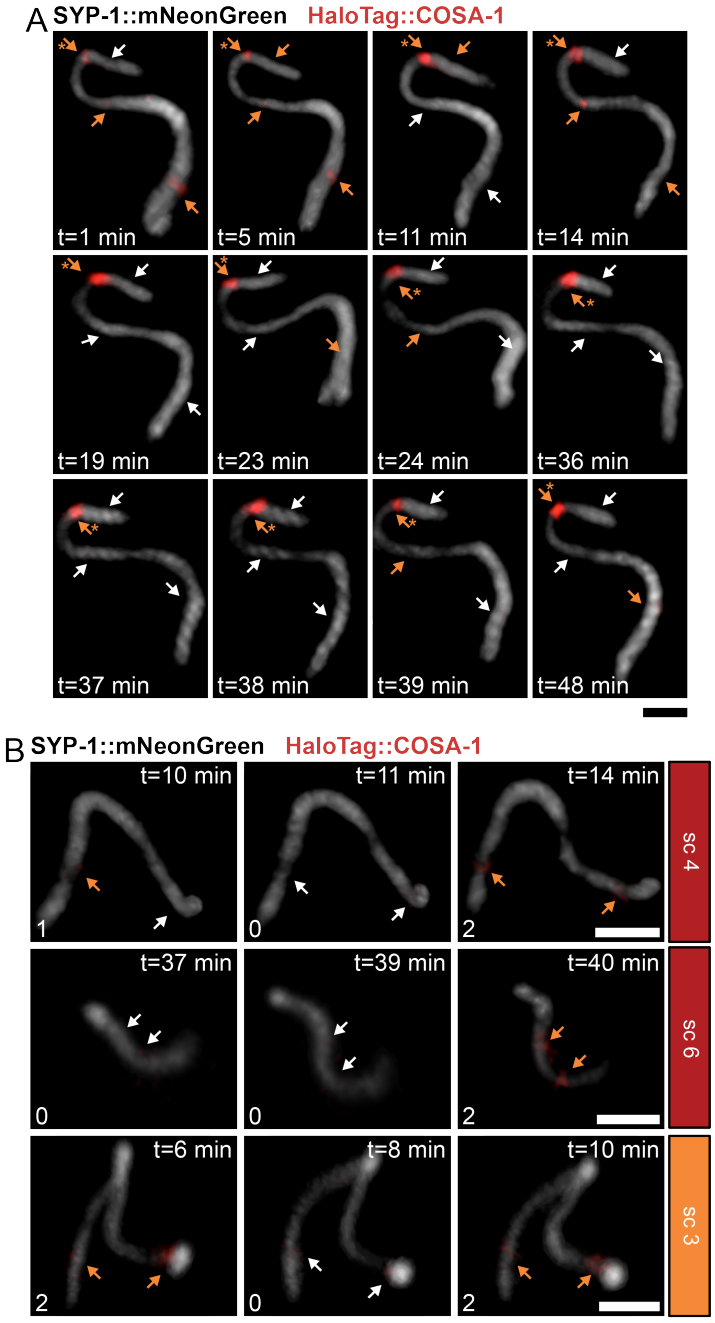


Figure G.4. Supplemental information for Figure 5.6

(A) Analogous to the **Figure 5.6B** showing the raw HaloTag::COSA-1 signal (not sharpened). **(B)** Cropped synaptonemal complexes that have zero HaloTag::COSA-1 foci associated with them (centre). Additionally, the same synaptonemal complexes in neighbouring time frames are displayed (left and right). The number in the bottom left corner denotes the number of foci identified by spotMAX that are associated to the corresponding synaptonemal complex. The arrows point to the regions of the synaptonemal complex that were associated with spotMAX-identified foci at least once during the timelapse. The orange colour of the arrow indicates that the foci were associated to a particular region at the given time point, whilst white indicates that the region has no associated foci. Asterix next to the arrow denotes HaloTag::COSA-1 focus that is present and identified in all time frames. Scale bars: 0.3 µm.

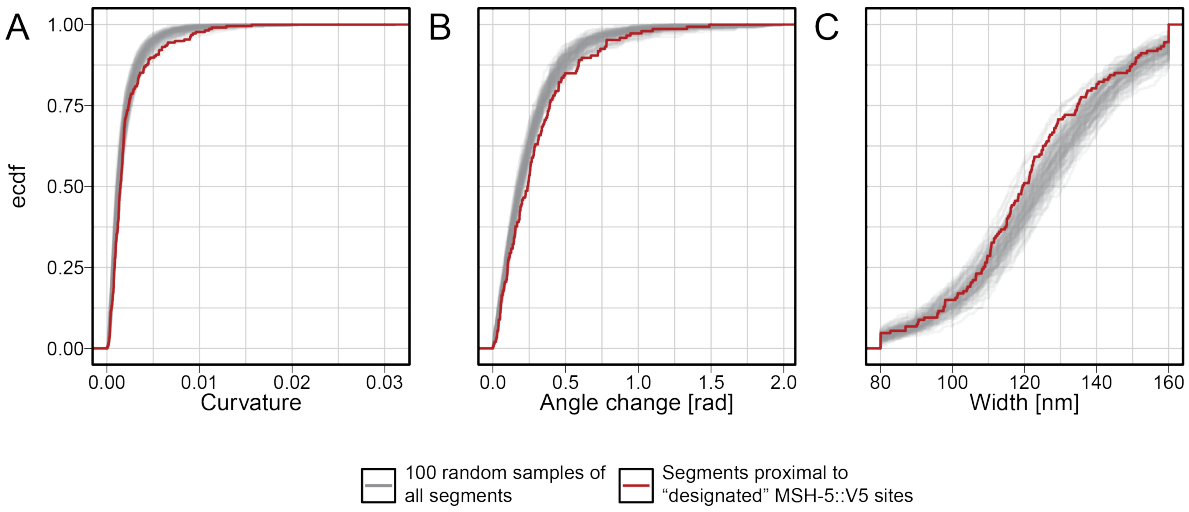


Figure G.5. Supplemental information for Figure 5.12

Comparison of empirical cumulative distributions (ecdf) of curvature **(A)**, angle change **(B)**, and width of the synaptonemal complex **(C)** in proximity to MSH-5::V5 foci labelled as designated in **Figure 5.10** (red), and within random samples drawn along the length of all analysed synaptonemal complex stretches (grey). The sample size corresponds to the number of crossover proximal points (red).

Table G.1. Total length of super-resolved synaptonemal complex stretches analysed in chapter 5

Rows to diplotene	Number of stretches	Total length [µm]	Average distance between the two *midline*[1] points [nm]	Total number of midline points
<6	35	91.0	26.2	3528
6	8	17.3	26.4	668
7	19	46.5	26.2	1798
8	17	38.7	26.3	1494
>8	21	36.7	26.3	1418

Table G.2. Total number of super-resolved MSH-5::V5 foci analysed in chapter 5

Rows to diplotene	Number of foci	Number of designated foci [2]
<6	20	11
6	4	1
7	12	2
8	20	2
>8	23	2

[1]Please consult section 3.7.3 for the details.

[2]Designated foci are classified as such based on the size of the ultrastructure.

List of publications

1. Joshua Blundon, Brenda Cesar, Jung Woo Bae, Ivana Čavka, Jocelyn Haversat, Jonas Ries, Simone Köhler, Yumi Kim. (2023) Skp1 proteins are structural components of the synaptonemal complex in *C. elegans*. bioRxiv. may 2023; 2023.05.13.540652.

2. Ivana Čavka, Rory M. Power, Dietrich Walsh, Timo Zimmermann, Simone Köhler. (2022) Super-resolution microscopy of the synaptonemal complex within the *Caenorhabditis elegans* germline. Journal of Visualized Experiments. sep 2022; (187), e64363.

3. Yiming Li, Wei Shi, Sheng Liu, Ivana Čavka, Yu-Le Wu, Ulf Matti, Decheng Wu, Simone Köhler, Jonas Ries. (2022) Global fitting for high-accuracy multi-channel single-molecule localization. Nature Communications. jun 2022; 13(1):3133.

4. Matthew E. Hurlock, Ivana Čavka, Lisa E. Kursel, Jocelyn Haversat, Matthew Wooten, Zehra Nizami, Rashi Turniansky, Philipp Hoess, Jonas Ries, Joseph G. Gall, Ofer Rog, Simone Köhler, and Yumi Kim. (2020) Identification of novel synaptonemal complex components in *C. elegans*. Journal of Cell Biology, 219(5), may 2020. ISSN 15408140.